The Life Magmatic at Summer Coon: Silicic Dike Propagation Controls and Emplacement Mechanisms at Stratovolcanoes

by

Gui Guenther Akşit

A dissertation accepted and approved in partial fulfillment of the
requirements for the degree of
Doctor of Philosophy
in Earth Sciences

Dissertation Committee:
Katharine Cashman, Chair
Meredith Townsend, Core Member
Thomas Giachetti, Core Member
Andrew Harp, Core Member
Marli Miller, Core Member
Katelyn McDonough, Institutional Representative

University of Oregon
Fall 2025

© 2025 Gui Guenther Akşit

This work is available under the terms of the Creative Commons

Attribution-Noncommercial License.

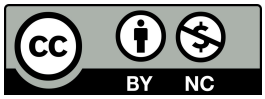

DISSERTATION ABSTRACT

Gui Guenther Akşit

Doctor of Philosophy in Earth Sciences

Title: **The Life Magmatic at Summer Coon: Silicic Dike Propagation Controls and Emplacement Mecanisms at Stratovolcanos**

Magmatic dikes are ubiquitous at arc stratovolcanoes, and play a critical role in the structural evolution of the volcanic edifice by either stalling in the subsurface or feeding eruptions anywhere along the volcanic surface. Understanding how dikes move within an edifice, and the controls dictating propagation or arrest, is vital for accurate hazard prediction and understanding volcano development more generally. At modern volcanoes studying magma transport through dikes, and the dynamic processes occurring within these dikes, is inherently difficult due to their intrusive nature. To fill this gap, I look at the ancient, eroded Summer Coon stratovolcano in Colorado where the magmatic plumbing system is exposed within the paleo-edifice. By studying the exposed, large, radial, silicic dikes at Summer Coon, I explore how internal magmatic properties, such as composition, porosity, viscosity, and crystallinity, work in tandem with external stresses due to a volcanic edifice to influence propagation trajectories. First, through an examination of flow fabrics in combination with analyses of the density, porosity, and geochemistry of dike margin and interior samples, I determine that two of the silicic dikes propagated laterally, at low-angles proximal to the center of the volcano. Distally, these dikes propagated at distinctly different angles, with one maintaining lateral flow along its length and the other switching to inclined flow. I interpret this difference as the consequence of a more buoyant magma forming the dike with inclined flow. To test how stresses due to a volcanic edifice along with magmatic properties may have acted to drive lateral intrusion, I model dike stability under and within a volcanic edifice for a magma undergoing dynamic volatile exsolution. I find that exsolution and outgassing promote dike intrusion into an edifice and that edifice stresses promote lateral propagation through low horizontal stress gradients. Finally, I focus on a single rhyolite dike to determine the emplacement mechanism for intrusion. Through mapping, structural analysis, and microtextural characterization, I determine that high shear

during intrusion of this dike resulted in mechanical fragmentation of a viscous magma at the margins, promoting outgassing and propagation toward the flanks. This dissertation includes previously submitted and unpublished co-authored material.



ACKNOWLEDGEMENTS

It was a long and winding road to get here, and I could not have done this without a plethora of support. From the professors in my life as an anthropologist who inspired me to be curious and think critically, to the first geology professor who encouraged me to consider a different path, thank you. Without you, I may not have had the courage to start again. And for the friends and professors during my first foray back into academia, you reminded me of what I was capable of and of the joy there is in studying the natural world, whether in tiny sundews thriving in secluded bogs, or the physics behind *everything*.

To those who believed in my abilities and saw my potential when I struggled to believe in it myself, I would not have completed this without you. Meredith, thank you for taking a chance on me, and having an amazing project for me to work on. I look forward to many years of collaboration, whether at Summer Coon or some other fascinating site to study magma transport. Marli, your mentorship and friendship have been some of the best things in my life during my time at UO. Your support truly got me through some very dark days, and it is amazing to have you as a cheerleader in my corner. Thomas, thank you for all of your support, whether through opening your lab to me, or helping me make sense of SEM imagery. Katelyn, thank you for joining my committee when I was desperate, and for having so much enthusiasm for my work! And finally, Kathy, thank you for adopting me as an advisee for the last years of this degree. Your expertise and insight have helped me grow a researcher.

This work is the product of many, many hours in the field, some better, and less blizzardy, than others. Andrew, your guidance in getting acquainted with Summer Coon, conducting fieldwork, and making sense of everything back in the lab, was invaluable for this research. Despite the grueling days in the field, I will always look back fondly on the days hiking soooooo many dikes at Summer Coon (even the Milk duds!) with you. I would not have been able to do this work without an amazing batch of field

assistants over the years. Kate, Kendall, Madeline, and Franzi, you helped so much! Thank you for taking good (and legible!) notes, extracting and carrying samples over the years.

There is one person who helped me succeed in so many different ways, my partner Eray. Whether as my pack mule, or the master extractor in the field, or as my rock and library buddy back home, your support through the *many* years it took to reach this point was invaluable. Thank you for sticking with me through career changes, multiple moves, blizzards, precarious scrambles, danger kitties, and bounding boulders. I cannot wait to see what the field (and future) holds for us next!

I want to thank all of my family, both the American and Turkish sides, for being with me on this journey. To my darling bunnies, Inky and Tombiş, thank you for putting up with my neediness and being my emotional support fluffle! I also want to thank all of the other support I had at UO, from the Earth Sciences department generally, to the amazing staff at the Craft Center who helped me rekindle my artistic side and provided a space to decompress during the pandemic, to Harinder Hoca and the Turkish language instructors who let me geek out about geology in Turkish. The community you provided helped keep me grounded. I also am indebted to the friends and support I have had at my time at Whitman. Sabrina, Caitlyn, Katie, and Elizabeth, thank you for being my writing circle buddies and making me feel like a college student again ;) MAGES, it has been wonderful having your community during all of this.

Finally, I want to thank all of my students, whether in the Sternberg Science Camps, in classes and field trips at UO, or in my classes at Whitman. You are why I finished this degree, your enthusiasm and love for geology, your curiosity and excitement about being out in the field for the first time, your pure joy at learning. On the tough days finishing this dissertation, you brought light and gave me energy to finish. Please stay curious and never lose your sense of wonder in the natural world.

This research was supported by in part by a National Science Foundation grant, EAR-2123211, a Geological Society of America Student Research Grant, and the University of Oregon.

Here, there be dragons...



THE EPIC OF THE SLEEPING DRAGONS

the mantle
is the realm of
dragons
a hostile molten forge
of writhing, convecting
beasts

and here
where the fury and heat of earth
meet the crust
slipped beneath the surface
water awakens
the nascent dragonlings of summer coon
and whispers promises of
a sun-drenched land where
air meets mountains

with dreams
of feeling the oligocene sun
on molten scales
the dragonlings begin their journey
burrowing ever upward

a relentless trek
through crystalline terra
past their trapped and frozen sisters
through wastes of immense
pressure
and heat
growing ever sluggish
as they rise

after countless depths
they despair
and can ascend no more
stuck between the writhing deep
and open skies
they cease their journey
unable to continue

eons of rest
in their crustal home
change the dragonlings
they grow
evolve
shed their scales of old
take on new forms
unrecognizable from their
mantle kin

revitalized and lightened
their odyssey to see the sun
resumes
one by one the
dragon siblings of summer coon
set off for a land unseen

the smallest
barely past dragonlings
ascend first
with ample water for the
way ahead
and scales small and pliable
they claw their way
through layer after layer
of mesozoic rock
a vertical climb
to the long sought land of light
they breach
and with breath of lava they
rejoice
making a new volcanic home
where they slumber on the open flanks
their quest complete

but for their grown
and changed
siblings
the journey will not end
in triumph

for the largest dragons
with crystal scales of silica
the voyage above is a struggle
their bulbous, buoyant forms
require great effort
to cleave a path
through solid earth
from their crustal den
they follow in their smaller siblings' steps
making the vertical climb
and shedding water
to ease their trek

but where the smallest
found the surface meeting sky
the largest find only
an igneous barrier
the mounds of exulted lava
left by their risen sisters
the mountain of summer coon

the path above blocked
they must break a new route
through the volcanic peak

if they are to ever
see the sun
and so
exhausted
slowly freezing within the cold summit
and with scales locking
the dragons turn
traveling on a lateral arc
toward the sun-soaked slopes

but in this
cold, hostile wasteland
of frigid rock and air
the largest dragons
with limbs heavy
water-parched
their effort spent
their molten scales hardening
to their weariness
they succumb
and drift off
to a dreamless slumber
the sun just beyond their
reach

the sleeping dragons
of summer coon

gui guenther akşit



TABLE OF CONTENTS

Chapter Page

1. THE DIKE'S GUIDE TO THE SUMMER COON VOLCANO 15

2. THE DIKE'S MUST LATERALLY FLOW: THE INFLUENCE OF MAGMA DENSITY & EDIFICE STRESSES ON SILICIC DIKE PROPAGATION TRAJECTORIES AT SUMMER COON VOLCANO, COLORADO, USA 20

2.1 Introduction 21

2.2 Geologic Background. 24

2.3 Methodology. 26

2.3.1 Fieldwork and Sampling 26

2.3.2 Flow Fabrics. 29

2.3.3 Magma Properties 31

2.4 Results. 33

2.4.1 Magma Composition 33

2.4.2 Flow Fabrics. 33

2.4.2.1 Dike A 33

2.4.2.2 Dike S 35

2.4.3 Magma Density and Porosity 35

2.4.3.1 Dike A 35

2.4.3.2 Dike S 37

2.4.4 The Source of Porosity 39

2.4.5 Host Rock Density and Magma Buoyancy 40

2.5 Discussion. 41

2.5.1 Dike Propagation and Magma Flow Directions 41

2.5.2 Topographic Stresses, Magma Buoyancy, and the Role of Magmatic Volatiles 43

2.5.3 Transition to Inclined Propagation in Dike S 44

2.5.4 Future Work 45
2.6 Conclusion 47
2.7 Bridge 48
3. MOSTLY GASLESS: THE IMPACT OF VOLATILE EXSOLUTION AND OUTGASSING ON THE DEPTH AND HEIGHT OF LATERAL DIKES BENEATH A VOLCANIC EDIFICE. 49
3.1 Introduction 50
3.2 Summer Coon Background & Field Data Analysis 53
3.2.1 Silicic Dikes at Summer Coon 53
3.2.2 Sample Collection 56
3.2.3 Vesicularity of Silicic Dikes at Summer Coon 57
3.3 Modeling the Depth and Height of Lateral Dikes 62
3.3.1 Model Set-Up 62
3.3.2 Model Results 65
3.3.2.1 No Exsolution 65
3.2.2.2 Volatile Exsolution for Capped 50% Porosity 65
3.2.2.3 Volatile Exsolution for Capped 15% Porosity 68
3.3.2.4 Summary of Key Model Trends 69
3.4 Discussion 71
3.4.1 Porosity, Outgassing & a Percolation Threshold 71
3.4.2 Edifice Stresses and Degassing Promote Lateral Propagation 73
3.4.3 Inferred Volumes of Intrusion 74
3.4.4 Field vs Model Differences 75
3.5 Conclusion 77
3.6 Bridge 78
4. HOW TO EMPLACE YOUR RHYOLITE: FIELD AND MICROTEXTURAL EVIDENCE OF EMPLACEMENT MECHANISMS FOR RHYOLITIC DIKE

PROPAGATION WITHIN A STRATOVOLCANO 79
4.1 Introduction 80
4.2 Geologic Background 83
4.3 Methodology 85
4.4 Field Observations 90
4.4.1 Brecciated Margin (BrM) 90
4.4.2 Glassy Flow-Banded Interior (GfB) 93
4.4.3 Platy Interior (PI) 93
4.4.4 Kinematic Indicators 94
4.5 Results - Image Analysis 96
4.5.1 Brecciated Margin 96
4.5.2 SEM Interiors 99
4.5.3 Porosity Variations 99
4.6 Discussion 101
4.6.1 Fragmentation Style of the Brecciated Margin 101
4.6.2 Intrusion and Cooling of the Interiors 104
4.6.3 A Question of Sintering 106
4.6.4 Comparison to Exposed Conduits 107
4.6.4 Direction of Future Work 108
4.7 Conclusion 109
5. SO LONG, AND THANKS FOR ALL THE DIKES 111
APPENDICES 114
A. SUPPLEMENTARY MATERIAL FOR CHAPTER 2 114
B. SUPPLEMENTARY MATERIAL FOR CHAPTER 3 126
C. SUPPLEMENTARY MATERIAL FOR CHAPTER 4 130
REFERENCES 133

LIST OF FIGURES

Figure Page

2.1 Simplified geologic map of Summer Coon denoting Dikes A and S 25

2.2 Sampling to final image analysis workflow 30

2.3 Diagram of significant flow fabrics for Dike A 34

2.4 Diagram of significant flow fabrics for Dike S 36

2.5 Graph of measured sample bulk density, calculated host rock, magma and melt density 38

2.6 Total measured margin and interior porosity along the length of Dikes A and S 39

2.7 Thin section and SEM imagery of pore and fractures in Dike A and S samples 41

2.8 Correlation between measured bulk density, total porosity, and flow fabric angles 46

3.1 Simplified geologic map highlighting dikes studied in Chapter 3 54

3.2 Vesicles in the field 57

3.3 Total Alkali-Silica plot for dikes studied in Chapter 3 58

3.4 Total porosity measurements for each dike 59

3.5 Margin porosity measurements as a function of distance along each dike 61

3.6 Modeled edifice stresses in the theta-theta direction 64

3.7 Dike stability profiles for a range of overpressures, porosity thresholds, and compositions 66

3.8 Dike opening profiles for no exsolution for both trachytic and rhyolitic compostions 67

3.9 Dike opening profiles for 15% porosity cap for both trachytic and rhyolitic compostions 70

4.1 Simplified geologic map highlighting the rhyolitic dikes 84

4.2 Dike D sampling locations 86

4.3 Field photos of Dike D highlighting key features and kinematic indicators 87

4.4 Brecciated margin image analysis imagery 89

4.5 Zone thickness along the length of Dike D 91

4.6 Field, hand sample, and thin section imagery from the BrM, GfB, and PI 92

4.7 Field measurements of different kinematic indicators plotted on Google Earth

map imagery of Dike D 95
4.8 Plot of plunge data recorded from kinematic indicators 97
4.9 Brecciated margin fractal dimension and shape parameter plots 98
4.10 Composite images of isolated pore space, silica, and microlite phase in SEM 100
4.11 Area fraction of pore space, silica phase and microlite content in interiors 101
4.12 Total porosity measured via helium pycnometry for each zone in Dike D 102
4.13 SEM imagery of brecciated margin, glassy flow-banded and platy interior zones 103
4.14 Conductive cooling timescales for 4.5 m-wide dike at 800°C 108
A.1a Complete, significant flow fabrics for Dike A proximal and medial segments 115
A.1b Complete, significant flow fabrics for Dike A distal segments 116
A.2a Complete significant flow fabrics for Dike S proximal and medial segments 117
A.2b Complete flow fabrics for Dike S distal segments 118
A.3 Sampling sites presented in Chapter 2 for Dike A and S 123
A.4 Pressure models calculated for Dike S 125
B.1 Google Earth image of sampling locations for the porosity analysis presented in Chapter 3 . . . 126
B.2a Dike opening profiles modeled for trachytic composition and 50% porosity threshold 128
B.2b Dike opening profiles modeled for rhyolitic composition and 50% porosity threshold 129
C.1 Plain light thin section imagery for the platy interior 130
C.2 Plain light thin section imagery for the glassy flow-banded interior 131
C.3 Plain light thin section imagery for the brecciated margin 132

LIST OF TABLES

TABLE Page

2.1 Sample data collected and analyzed for Dike A. 27

2.2 Sample data collected and analyzed for Dike S 28

A.1a Complete data collected for Dike A 119

A.1b Complete data collected for Dike A continued 120

A.2a Complete data collected for Dike S 121

A.2b Complete data collected for Dike S continued 122

A.3 Complete normalized bulk rock geochemistry results for Dike A and Dike S 124

B.1 Normalized bulk rock geochemistry presented for the silicic dikes in Chapter 3 127



CHAPTER 1

The Dike's Guide to the Summer Coon Volcano

The shallow plumbing system at stratovolcanoes is dominated by intrusions in the form of dikes, sills, and stocks. When magmatic dikes enter the volcanic edifice, they can travel along varied pathways to either stall in the subsurface, or erupt anywhere along the surface of the volcano. Estimating the path that magma takes in the subsurface, as well as the controls dictating these paths and the dynamics of emplacement, is critical for accurately assessing volcanic hazards at modern stratovolcanoes. Dike-fed flank and fissure eruptions occurring at a distance from the main volcanic summit have been directly observed at Mt. Etna, Chaitén, and Cordón Caulle, or evidence of past dike-fed eruptions has been preserved, such as at South Sister volcano in Oregon (Acocella et al., 2003; Castro et al., 2013; Donnelly-Nolan et al., 2008; Lara, 2009). Despite the commonality of dike-fed eruptions, as well as the prevalence of dike intrusion without eruption (e.g., Agung and Sakurajima; Albino et al., 2019; Hotta et al., 2016), the interplay of controls dictating propagation paths is not well constrained. Geophysical techniques can track propagation by interpreting resultant seismicity, as well as probable depths, and rough volumes or pressures of intrusion by monitoring surface deformation. However, unless the material erupts, we are limited in our interpretation of the nature of the magma intruded, as well as the external and in-conduit processes that influence magma transport. To unravel this mystery of magma transport under stratovolcanoes, we must investigate the dissected remains of eroded stratovolcanoes and the shallow plumbing systems exposed within.

Potential factors that influence magma transport through dikes can be broadly categorized

into internal and external controls. Internal controls are intrinsic to the magma itself, and can include the composition, density, and viscosity of the magma. These are all modified by dynamic processes that occur during intrusion due to cooling, decompression, and the flow of magma, such as crystallization, volatile exsolution and degassing. External controls, in contrast, are factors influencing propagation that are independent of the material being intruded. External factors may include the stress field, such tectonic or large-scale regional stresses or more locally from the topographic load of the edifice, pre-existing features such as faults, density and rigidity layering within the volcano or sub-edifice crust, or conduit changes during propagation. Here, and in the rest of this dissertation, I use the term conduit to refer to the fracture through which magma is flowing over the lifetime of the dike.

In this work, I aim to untangle the controls on silicic dike propagation within an edifice at Summer Coon volcano through a combination of field mapping, lab analyses, and computer modeling. I investigate the following questions in each of the different chapters:

Chapter 2: What are the trajectories of magma recorded in large silicic dikes? Is there a correlation between intrusion direction and magmatic properties? What role does buoyancy play in driving different magmatic pathways?

Chapter 3: How could dynamic exsolution and outgassing influence both the lateral propagation within an edifice as well as the ability of dikes to enter an edifice?

Chapter 4: What are the mechanisms of emplacement for a rhyolitic dike at Summer Coon? What processes occur in the conduit to form different textural zones?

In *Chapter 2: The Dikes Must (Laterally) Flow*, I lay the groundwork for the remaining dissertation by determining the propagation direction for two of the largest, best exposed silicic dikes at Summer Coon (Dikes A and S; Fig 2.1), and looking at the correlation between flow direction and magmatic properties of density and porosity. Through image analysis of aligned, elongate minerals preserved both at the margins and interior of the dikes I find that in the segments proximal to the center of the volcanic edifice both dikes record initially horizontal intrusion, in line with the previous work by Poland et al. (2004). However, while Dike A records lateral propagation along its entire length, Dike S switches to inclined or near vertical propagation distally. I find that the variable emplacement trajectories of Dike S may be

correlated with density measurements along the dike, while there is no correlation between fabrics and density for the laterally emplaced Dike A. I additionally show that a volcanic edifice may have acted as a buoyancy filter for the magmatic density ranges calculated for each dike, and driven initial lateral propagation. I posit that the change in propagation along Dike S may have occurred from variable buoyancy forces, influenced by exsolved magmatic volatiles, or stress state along the dike pathway. This work demonstrates the importance of higher density sampling along entire dike lengths, as well as taking interior and margin samples, to fully characterize dike propagation pathways and magma transport evolution. I also show that external stresses alone may not be enough to dictate propagation, and that the dynamic processes occurring within magma also need to be considered, especially in regard to their influence on magmatic buoyancy. This work was done in collaboration with Meredith Townsend and Andrew Harp, and was published in the *Bulletin of Volcanology*.

In *Chapter 3: Mostly Gasless*, I build on the work laid out in *Chapter 2* to explore how the lateral dike propagation observed proximally for Dikes A and S could be modulated by the dual controls of edifice stress and degassing. As magma ascends from the reservoir to the surface, it experiences a change in external stress that would allow for the exsolution of volatiles within the magma (e.g., Liu et al., 2005), yet this process of dynamic exsolution has been poorly considered in dike modeling. Field data for fifteen of the large silicic dikes at Summer Coon show they are extremely vesicle poor (<8% total porosity), even though at their paleodepths and inferred pressures of intrusion they could be highly vesicular (>50%). I argue that these low porosities come about both from a low percolation threshold for crystal-rich magmas, at which permeable networks would form and exsolved gasses escape, and from high shear within the conduit, evidenced by the strong fabrics found in the margin and interior in *Chapter 2*. This field evidence of degassed dikes informs a model for dike stability within a volcanic edifice, in which I test how dynamic exsolution and outgassing could encourage lateral propagation for dikes of either a trachytic or rhyolitic composition for a range of magmatic overpressures and under different exsolution constraints. Using a refined FEM model for edifice stresses designed by Scholz (2025), I find that outgassing significantly impacts the ability of a dike to enter into an edifice and in tandem with edifice stresses promotes in-edifice propagation. When allowing for volatile exsolution

of a saturated magma, and setting a field-informed percolation threshold of 15%, the dikes of both compositions can enter into the edifice at the level of exposures observed at Summer Coon, even at low overpressures. Once in the edifice, these outgassed magmas are effectively trapped by the low pressure gradients induced by the edifice itself, and can laterally propagate toward the volcanic flanks. This work highlights the importance of considering exsolution and outgassing during propagation in the dike modeling field, not just for estimating propagation paths, but also in reconsidering volumes necessary for intrusions. This research was conducted in collaboration with Meredith Townsend, Kate Scholz, and Andrew Harp.

In the final chapter *How to Emplace Your Rhyolite*, having established that the silicic dikes at Summer Coon laterally intruded (at least proximally), and that active outgassing during propagation, in tandem with low stress gradients induced by the edifice, could have encouraged this lateral intrusion, I narrow my focus to the emplacement history of a single rhyolite dike, Dike D. Rhyolitic, dike-fed eruptions, such as the recent activity of Chaitén or Cordón Caulle in Chile, or the 600 BP eruption of the Mono-Inyo craters in California, display complicated eruption dynamics beginning with explosive activity, transitioning to hybrid explosive-effusive behavior, and concluding with effusive flows and/or dome-building (Castro et al., 2012; Lara, 2009; Schipper et al., 2013; Sieh & Bursik, 1986). These eruption dynamics are controlled by deeper conduit processes, which cannot be studied at active volcanoes, but can be inferred from exposures of ancient rhyolitic conduits, such as seen in Dike D. Additionally, exposed conduits best preserve the progression of magmatic material over the course of activity, allowing us to test two alternate hypotheses for the evolution of effusive rhyolites, as interpreted from erupted deposits: either (1) high-shear of a viscous magma promotes the brittle (mechanical) fragmentation of rhyolite during intrusion at the conduit margins, but the interior magma maintains viscous cohesion to effusively erupt (e.g., Gonnermann & Manga, 2003; Rust et al., 2004; Tuffen et al., 2003; Tuffen & Dingwell, 2005), or (2) effusive rhyolites fragment at depth through high bubble pressures, traveling as a pyroclastic mixture through the conduit, and sintering after fragmentation to reform a viscous magma (e.g., Farquharson et al., 2022; Foster et al., 2024; Gardner et al., 2017; Wadsworth et al., 2020). By mapping macroscale zones observed in the field that are ubiquitous at the

rhyolite dikes of Summer Coon, brecciated margins, glassy flow-banded interiors and platy interiors, and conducting microscale textural analysis of the material from these three zones, I find that Dike D intruded as a coherent, viscous magma. I reconstruct a propagation history where during the initial stages of intrusion, the dike experienced high shear at the margins so to pluck and incorporate host rock clasts and brittlely fragment magmatic material, which was continuously abraded as transport persisted. The interior zones formed as the magma continued to intrude, forming viscous flow-banding where strain-rates were low enough, but occasionally fracturing in isolated areas experiencing high-shear, until eventually the interior cooled over weeks or months. This work offers a rare glimpse of the deeper rhyolitic conduit at stratovolcanoes, and how non-erupted material may evolve during intrusion. This work is a collaboration with Meredith Townsend, Thomas Giachetti, Katie Springer, Kathy Cashman, and Andrew Harp.


THE Dikes
MUST
laterally
FLOW

CHAPTER TWO

The dikes must (laterally) flow: The influence of magma density & edifice stresses on silicic dike propagation trajectories at Summer Coon volcano, Colorado, USA

This work was previously published as:

Aksit, G. G., Townsend, M., & Harp, A. (2025). The influence of magma density and edifice stresses on silicic dike propagation trajectories at Summer Coon volcano, Colorado, USA. *Bulletin of Volcanology*, 87(10), 81. https://doi.org/10.1007/s00445-025-01870-9

and is formatted to the Bulletin of Volcanology standards.

2.1 INTRODUCTION

Magma transport within stratovolcanoes occurs primarily through dikes, which follow highly variable pathways. Dikes can erupt at the summit, propagate laterally to erupt along the flanks, or arrest in the subsurface altogether (Gudmundsson et al. 1999; Gudmundsson 2002; Geshi 2008; Acocella & Neri 2009; Moran et al. 2011; Townsend et al. 2017). Understanding what controls dike arrest or eruption, as well as propagation direction and vent locations, is critical for hazard assessment at stratovolcanoes. However, forecasting dike pathways remains challenging due to limited understanding of the interplay between internal factors (e.g., magma buoyancy, viscosity) and external factors (e.g., topographic loading, rigidity layering) (Rubin & Pollard 1987; Rubin 1995b; Menand & Tait 2002; Pinel & Jaupart 2000; 2004; Gudmundsson 2006; Maccaferri et al. 2011; Heimisson et al. 2015; Rivalta et al. 2015; Urbani et al. 2018).

The direction of magma transport in the shallow crust is governed by external factors such as mechanical boundaries, stress barriers, or buoyancy variations. Although many numerical models (e.g., Pinel & Jaupart 2000; Dahm 2000; Rivalta et al. 2015) and analog experiments (e.g., Rivalta et al. 2005; Rivalta & Dahm 2006; Rivalta et al. 2015) are configured for vertical dike ascent, geologic and geophysical data indicate that lateral propagation is common in the shallow crust, both at rift zones and beneath volcanic edifices (Rubin & Pollard 1987; Geshi 2008; Sigmundsson et al. 2015; Townsend

et al. 2017; Urbani et al. 2017). A switch from vertical to lateral magma transport could occur when magma encounters a mechanical boundary (Taisne & Jaupart 2009; Maccaferri et al. 2010; Geshi et al. 2012; Barnett & Gudmundsson 2014; Bazargan & Gudmundsson 2019) or a stress barrier arising from topography or from regional and local tectonics (Pinel & Jaupart 2004; Poland et al. 2008; Kervyn et al. 2009; Menand 2011; Gudmundsson 2011). Alternatively, an adjustment from vertical to lateral transport could occur when the magma reaches a level of neutral buoyancy, where the magma is no longer less dense than the surrounding crust (Walker 1986; Rubin & Pollard 1987; Ryan 1988; Lister and Kerr 1991; Rubin 1995b; Chen et al. 2011; Townsend et al. 2017). Additionally, the gradual construction of an edifice can alter the conditions for vertical and lateral propagation over time (Pinel & Jaupart 2000; 2004; Kervyn et al. 2009; Urbani et al. 2018).

Existing models for dike propagation often neglect the dynamic evolution of magma physical properties during intrusion. Processes including decompression-induced volatile exsolution, crystallization, and outgassing can change magma buoyancy and viscosity, influencing dike propagation and arrest (Gonnerman & Manga 2007; Zellmer et al. 2011; Geshi et al. 2020; Abdullin et al. 2024). Magma buoyancy may increase due to bubble growth during exsolution (Geshi et al. 2020) but may decrease by the loss of bubbles through outgassing to the country rock (e.g., Stasiuk et al. 1996; Rust et al. 2003; Caricchi et al. 2011). At the same time, magma viscosity increases with degassing and crystallization, leading to the potential viscous arrest of dikes (Rasmussen et al. 2022). Moreover, few models consider propagation within constructive topography (Zhan et al. 2022; Mantiloni et al. 2023), either restricting dike propagation to take place entirely beneath an edifice, or assuming that dikes that can penetrate the edifice will erupt close to the summit (Pinel & Jaupart 2004).

At modern stratovolcanoes, seismicity and ground deformation can provide indirect evidence of dike intrusion pathways, volumes, and rates of propagation, but offer limited information on magma dynamics (e.g., Ágústsdóttir et al. 2016; Hotta et al. 2016; White & McCausland 2019; Albino et al. 2019). Geophysical data combined with numerical modeling can illuminate external conditions, such as the stress state in the edifice (Corbi et al. 2015), but internal magma properties are unknown unless an eruption occurs. Since erupted material represents only a fraction of what is intruded (White et

al. 2006), there is a sampling bias towards material that reaches the surface and a paucity of data on dikes that arrest. This knowledge gap is especially pronounced for silicic magmas, which erupt less frequently than mafic magmas but have higher water content, more complex rheology, and greater potential for explosive eruptions. Despite the record of geologically recent silicic dike-fed eruptions at stratovolcanoes and in arc settings, such as Devil's Chain at South Sister volcano, Oregon (Fierstein et al. 2011), the Glass Mountain eruptions at Medicine Lake, California (Donnelly-Nolan et al. 2008), or the Mono-Inyo craters, California (Sieh & Bursik 1986), there is a relative disparity of research on silicic dike propagation. Although silicic dikes are well-documented in eroded systems such as Spanish Peaks in Colorado (Johnson 1968; Smith 1975) or Sunlight Volcano in Wyoming (Feeley 2003), the influence of magma dynamics on their propagation remains understudied.

Eroded stratovolcanoes provide valuable opportunities to collect quantitative data on dike propagation directions and directly sample solidified magmatic material. In this study, we leverage the excellent exposure of silicic dikes within the well-characterized Summer Coon volcanic system, an Oligocene-aged stratovolcano that has been eroded almost down to its base, revealing a system of radial dikes (Lipman 1968; Moats 1990; Poland et al. 2004; Harp et al. 2018; Harp 2021; Lipman et al. 2024). We focus on two silicic dikes, which are well-exposed along their entire multi-kilometer lengths and were previously studied and interpreted to have propagated laterally within the volcanic edifice (Poland et al. 2004; 2008). We extend Poland et al.'s (2004) previous research on propagation trajectories by collecting higher resolution field data on magma flow directions along the complete exposed length of the dikes to understand how and on what scale dike propagation directions varied. We interpret the evolution of magma transport from the original intrusion event, preserved in dike margins, through to the final emplacement of magma, recorded in dike interiors. Additionally, we present data on the dike material's porosity, density, crystal fraction, and chemical composition to quantitatively constrain the magma's physical properties during intrusion. Our new field data shed light on the roles of buoyancy and topographic stress in dike propagation and how volatile exsolution and degassing may have influenced these forces to drive the dikes in different directions.

2.2 GEOLOGIC BACKGROUND

Summer Coon volcano is an eroded Oligocene stratovolcano located on the eastern edge of the San Juan Volcanic Field (SJVF) in Colorado, USA (Lipman 1968; Lipman et al. 1970). K-Ar, U-Pb and 40Ar/39Ar age dating of edifice material, lava flows, and intrusions indicate that Summer Coon was active from 34.2-32.8 Ma during the pre-ignimbrite volcanic episode of the SJVF (Lipman et al. 1970; Perry et al. 1999; Lipman et al. 2024). At its maximum size, the edifice diameter was at least ~14 km and the height was at least ~2200 m above the basement, estimated by projecting the 17° slope of contacts between lava flows toward the volcanic center (Moats 1990). Since cessation of volcanic activity, the edifice has been eroded to expose the interior plumbing system of the volcano ~300 m above the basement (Moats 1990; Harp 2021). Regional deformation during the formation of the Rio Grande Rift around 21.5 Ma resulted in minor tilting of the extinct Summer Coon volcano ~7° to the southeast (Lipman & Mehnert 1975; Lipman 1970; Mertzman 1972; Moats 1990).

Today, hundreds of radial basaltic-andesite dikes and ~20 andesite to rhyolite dikes are exposed within the edifice (Lipman 1968; Mertzman 1972). These dikes are oriented about a hydrothermally altered central intrusive complex (CIC) (Fig. 2.1) containing several diorite and granodiorite stocks (Harp 2021). Based on composition, cross-cutting relationships, and the stratigraphy of extrusive products, Lipman (1968) proposed that the basaltic-andesite dikes are the oldest, followed by the rhyolite dikes, and then the intermediate composition, mainly dacitic, dikes. This compositional progression is mirrored by the early eruptive basaltic-andesite breccias and lavas that form the bulk of the edifice at the level of exposure, which are overlain by smaller rhyolitic flows, and then capped by dacitic deposits on the volcanic flanks (Lipman et al. 2023; Fig. 2.1). In this work, the early basaltic-andesite dikes will be referred to as "mafic dikes," and middle and late-stage andesite to rhyolite dikes as "silicic dikes." The mafic and silicic dikes exhibit striking differences in their outcrop lengths and thicknesses. The mafic dikes average ~260 m in length and ~1-3 m in thickness (Mertzman 1972; Harp & Valentine 2018), whereas the silicic dikes reach up to 6.5 km in length and ~1-50 m in thickness (Lipman 1968; Mertzman 1972; Moats 1990).

The mafic and silicic dikes vary not only in exposed geometries, but also in inferred

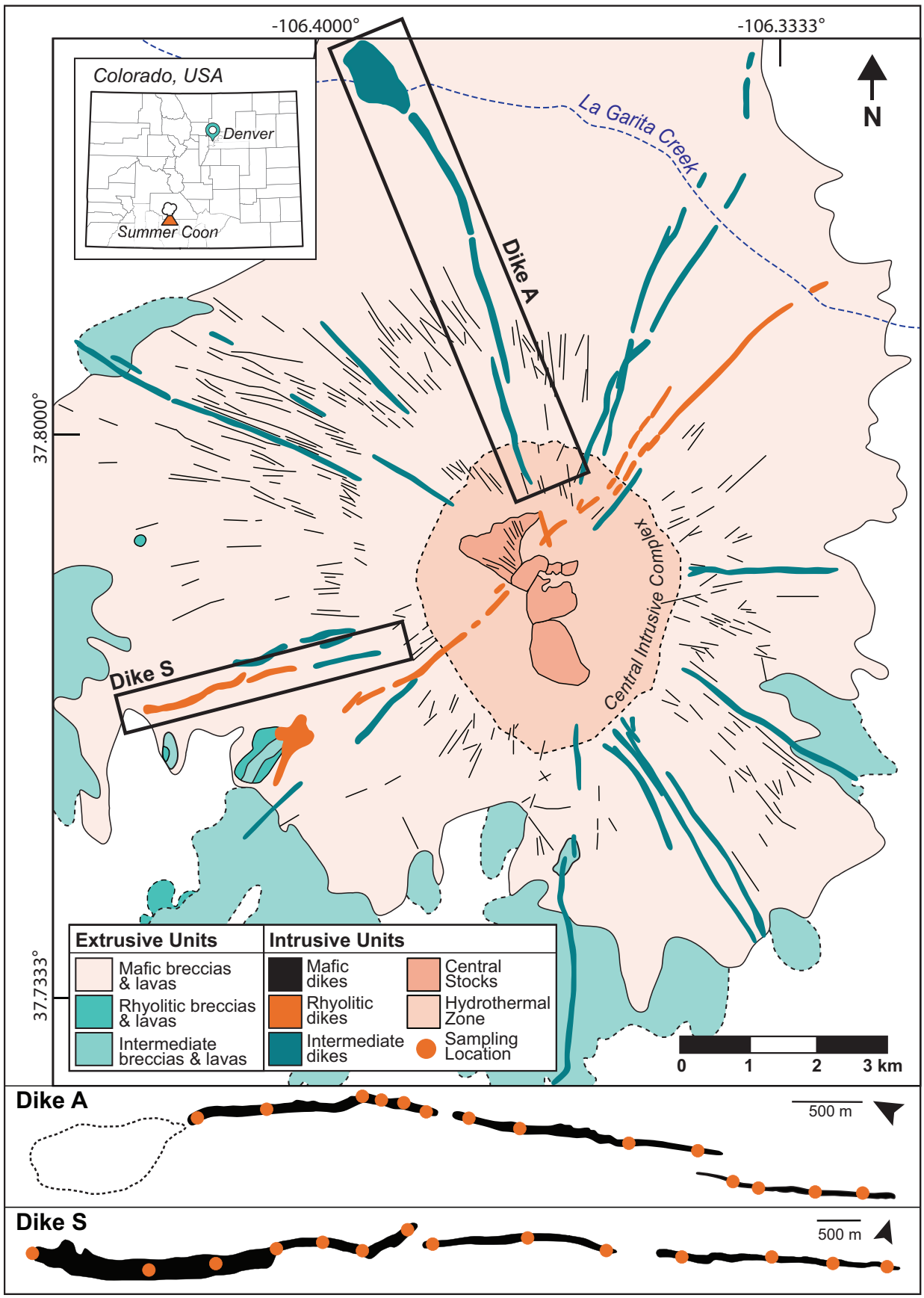
-106.4000°
-106.3333°
Colorado, USA
Denver
Summer Coon
La Garita Creek
N
Dike A
Dike S
Central Intrusive Complex
37.8000°
37.7333°
Extrusive Units
Mafic breccias & lavas
Rhyolitic breccias & lavas
Intermediate breccias & lavas
Intrusive Units
Mafic dikes
Rhyolitic dikes
Intermediate dikes
Central Stocks
Hydrothermal Zone
Sampling Location
0 1 2 3 km
Dike A
500 m
Dike S
500 m

Figure 2.1. (***Previous Page)*** Simplified geologic map of Summer Coon volcano, modified from Lipman (1968). The silicic dikes discussed here (Dike A and Dike S) are marked by the black rectangles on the map. Approximate outlines of each dike are presented below the map (thicknesses not to scale). Sampling locations used in this study are marked by orange circles on the dike profiles. The laccolith at the end of Dike A is outlined by a dashed line to mark its presence, but it is not considered during analysis in this paper

emplacement angles. Harp and Valentine (2018) measured plagioclase crystal fabric orientations preserved along the margins of 77 mafic dikes and concluded that most of these dikes were emplaced at an inclined angle ~45° from horizontal. Poland et al. (2004) analyzed two of the silicic dikes using Anisotropy of Magnetic Susceptibility (AMS) on margin and limited interior cores and interpreted overall low-angle, lateral propagation in response to stresses generated by the weight of the edifice, but they did find some areas of localized vertical flow (Poland et al. 2004). These flow variations may be due to sampling near en echelon segmentation in the areas proximal to the CIC. Studying dike behavior in the distal ends and away from segmented areas can clarify whether lateral propagation was consistent and reveal transport variations and potential causes for variation during the emplacement of km-scale silicic dikes.

This study revisits the silicic dikes analyzed by Poland et al. (2004), referred to as Dike A (6.4 km long) and Dike S (3.2 km long) (Fig. 2.1). Both dikes exhibit en echelon segmentation, with Dike A divided into three main segments and Dike S divided into four main segments. Dike thicknesses increase from proximal to distal ends, with significant widening at the distal ends interpreted to reflect the change in paleodepth and the corresponding change of overburden pressure (Tables 2.1 & 2.2) (Poland et al. 2008). The paleodepths of the dikes range from ~1.65 km (Dike A) and ~1 km (Dike S) near the CIC to within tens of meters of the paleosurface distally (Moats 1990). Dike A also features two areas of anomalous widening, one in a highly segmented portion of the medial segment and a laccolith-like structure at its distal end (Fig. 2.3) (Lipman 1968). This work aims to constrain dike propagation and flow directions along their full lengths and evaluate how magmatic properties influence these patterns.

2.3 METHODOLOGY

2.3.1 Fieldwork and Sampling

Fieldwork was conducted during summers of 2020-2023 at Summer Coon volcano, north of Del Norte,

Table 2.1. Sample data collected and analyzed for Dike A

Dike A	Mean Fabric Angle (°) (segment)	Mean Fabric R-value	Sample ID#	Normalized Distance from Dike Start	Dike Thickness (m)	Fabric Angle (°)	Fabric Number of Crystals (n)	Fabric R-value	Total Porosity (%)	Bulk density (kg/m³)	Solid density (kg/m³)
Margin	**167**	**0.57**									
Proximal	171	0.86	**SCA.2-1**	0.10	29.5	149	185	0.23	7.98	2401	2609
			SCA.3-1	0.14	26.9	165	294	0.40	15.57	2218	2627
			SCA.4-1	0.20	25.5	179	222	0.43	10.35	2456	2740
			SCA.5-1	0.22	21.1	10	234	0.48	4.72	2524	2650
Medial	141	0.52	**SCA.6-1**	0.30	25.8	117	183	0.14	4.65	2556	2681
			SCA.17-1	0.35	33.6	75	380	0.37	3.24	2569	2655
			SCA.16-1	0.49	56.7	135	215	0.30	0.63	2591	2608
			SCA.13.1	0.52	30.2	151	231	0.30	8.13	2481	2701
			SCA.12-1	0.52	25.2	158	303	0.31	8.70	2422	2653
Distal	175	0.57	**SCA.11-1**	0.57	31	1	176	0.64	9.65	2422	2673
			SCA.10-1	0.60	41.2	12	298	0.28	8.02	2422	2634
			SCA.9-1	0.63	43	22	242	0.49	8.64	2411	2639
			SCA.8-1	0.65	39	170	384	0.41	2.88	2538	2613
			SCA.7-3	0.65	38	144	97	0.32	8.27	2452	2673
			SCA.18-1	0.77	42.7	100	134	0.41	1.48	2567	2605
			SCA.14-3	0.83	55.2	173	127	0.47	1.95	2557	2608
Interior	**164**	**0.53**									
Proximal	163	0.60	**SCA.2-2**	0.10		173	221	0.25	3.23	2540	2625
			SCA.3-2	0.14		4	241	0.54	6.53	2483	2657
			SCA.5-2	0.22		122	181	0.29	10.37	2352	2624
Medial	154	0.96	**SCA.6-2**	0.31		162	369	0.30	9.99	2527	2807
			SCA.13-4	0.52		146	163	0.27	12.70	2351	2693
Distal	176	0.38	**SCA.11-2**	0.57		60	305	0.25	6.27	2544	2714
			SCA.9-3	0.63		173	361	0.37	3.83	2575	2677
			SCA.7-2	0.65		161	186	0.58	4.07	2578	2688
			SCA.18-2	0.76		22	248	0.37	6.53	2510	2686
			SCA.14-1	0.82		132	257	0.27	7.02	2473	2660

Table 2.2. Sample data collected and analyzed for Dike S

Dike S	Mean Fabric Angle (°) (segment)	Mean Fabric R-value	Sample ID#	Normalized Distance from Dike Start	Dike Thickness (m)	Fabric Angle (°)	Fabric Number of Crystals (n)	Fabric R-value	Total Porosity (%)	Bulk density (kg/m³)	Solid density (kg/m³)
Margin	**125**	**0.36**									
Proximal	176	0.97	**SCS.1-3**	0.02	11.5	3	315	0.36	4.64	2475	2595
			SCS.2-3	0.06	13.2	156	315	0.12	4.09	2488	2594
			SCS.3-1	0.14	12	169	191	0.36	4.75	2482	2606
			SCS.4-4	0.25	16	100	234	0.11	8.46	2431	2656
Medial	115	0.56	**SCS.6-1**	0.38	20.1	116	435	0.30	7.28	2418	2608
			SCS.7-1	0.45	29.7	66	289	0.23	7.81	2387	2589
			SCS.5-3	0.55	21.7	116	493	0.40	7.82	2393	2596
			SCU.4-1	0.58	32.2	19	256	0.05	2.33	2520	2580
			SCS.12-1	0.63	38	149	299	0.40	5.69	2427	2574
Distal	109	0.54	**SCS.11-1**	0.66	34.6	62	356	0.14	6.91	2416	2595
			SCS.10-1	0.73	74.5	86	368	0.22	9.05	2354	2588
			SCS.9-1	0.80	81	169	292	0.29	3.99	2472	2575
			SCS.8-6	0.86	72.2	103	329	0.52	2.39	2522	2584
			SCS.8-7	0.87	72.2	111	199	0.27	-	-	-
			SCS.13-1	0.97	52.4	125	476	0.14	4.38	2457	2569
Interior	**103**	**0.40**									
Proximal	118	0.88	**SCS.1-1**	0.02		100	464	0.48	5.70	2432	2579
			SCS.2-1	0.07		168	305	0.13	4.85	2508	2636
			SCS.3-2	0.14		121	316	0.32	8.16	2444	2662
			SCS.4-2	0.25		134	268	0.40	8.71	2433	2665
Medial	80	0.26	**SCS.6-3**	0.38		42	371	0.35	9.24	2428	2676
			SCS.5-2	0.55		117	257	0.21	6.11	2506	2669
			SCS.12-3	0.63		130	307	0.07	11.36	2298	2592
Distal	63	0.50	**SCS.10-3**	0.73		-	-	-	9.34	2267	2500
			SCS.8-3	0.87		93	210	0.20	1.08	2517	2544
			SCS.8-1	0.87		33	411	0.28	4.41	2463	2577
			SCS.13-2	1.00		24	370	0.13	7.16	2395	2580

CO. We walked the entire lengths of Dike A and Dike S, identifying at least one margin of each dike within a meter of the dike-host rock contact at all sampling locations. Dike thicknesses were measured at sampling locations with a TruPulse 200 Laser Rangefinder where exposure allowed, or estimated using Google Earth based on margins we identified in the field. This confirmed segmentation and widening anomalies previously reported (e.g., Lipman 1968, Moats 1990). Drone imagery supplemented on-the-ground interpretations and confirmed the continuity of the dikes, ultimately informing the dike outlines and maps presented in Figure 2.1.

We collected 41 oriented samples from the margin and interior of Dike A and 42 from Dike S along their entire lengths, starting from the first outcrop beyond the hydrothermally altered CIC. We targeted chilled margin samples as close to the host rock contact as possible (Fig. 2.2A) to analyze flow fabrics that record the initial dike propagation directions (Shelley et al. 1985; Poland et al. 2004; Harp & Valentine 2018). Interior samples were collected for flow fabric analysis to determine how magma flow evolved following initial intrusion (Poland et al. 2004). Samples were also collected for bulk rock chemistry, bulk density, and porosity analyses to characterize physical magma properties. Because the bulk density of the now solidified magmatic material represents an upper bound on the magma density at the time of intrusion, we combine density and porosity measurements with a model for melt densities based on chemical composition to constrain the true magma (melt + crystals + gas) density. Sampling intervals averaged 200-500 m for margins and 300-550 m for interiors, with sampling every 5-10 m across the dike width at selected locations (Fig. 2.1). Finally, we collected several host rock samples from various locations around the ancient volcanic edifice for analysis of bulk density.

2.3.2 Flow fabrics

We selected 26 oriented samples from Dike A and 25 from Dike S to analyze for flow fabrics. Margin-parallel polished and covered thin sections were prepared by Spectrum Petrographics Inc. and National Petrographic Service, Inc. Whole thin sections were photographed in plane light (Fig. 2.2B) with a Nikon Super CoolScan 5000 ED Film Scanner. Photos were converted to binary images in ImageJ to isolate crystals larger than microlites from the groundmass (Fig. 2.2C). We opted to do

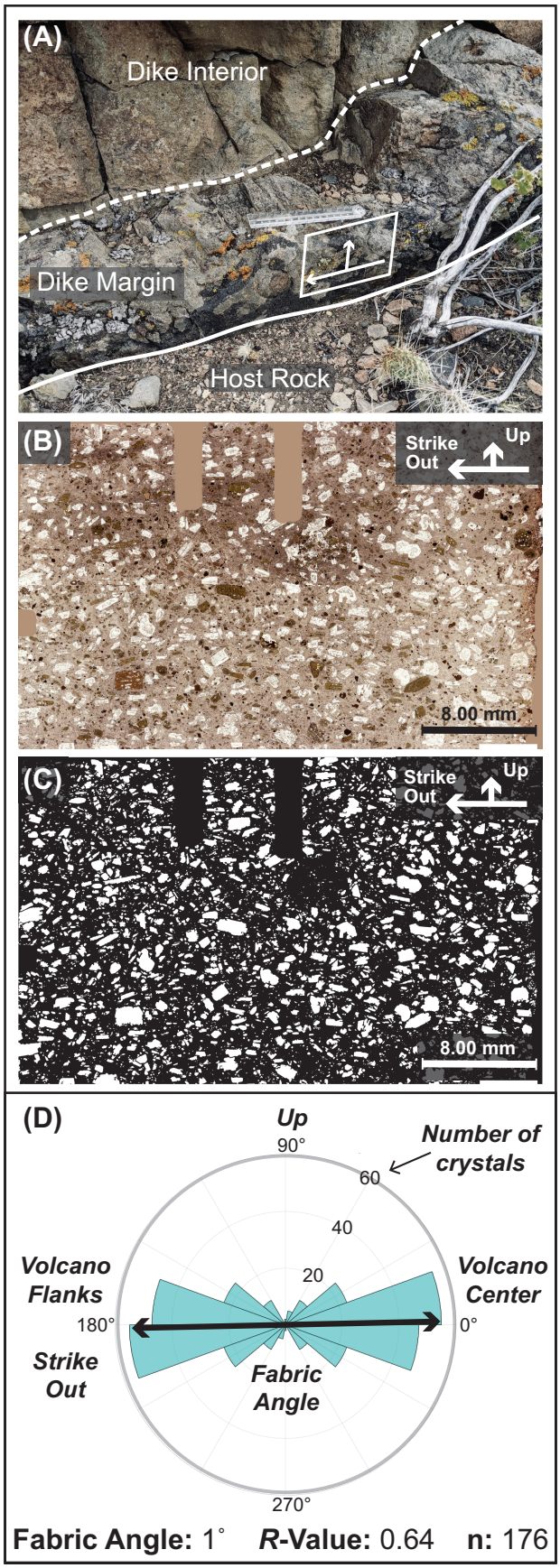

image analysis in this study over AMS as our thin sections were used for multiple analyses, including for flow fabrics, crystallinity, and SEM imaging. Using image analysis also allowed us to consider flow from a larger crystal population than AMS captures, without the uncertainty that fabrics are flow related (Poland et al. 2004). Crystal aspect ratios and orientations were calculated in ImageJ (Schneider et al. 2012). For each thin section, we filtered the crystals to isolate both the top 10% in aspect ratio and size, which are most sensitive to magma shear (Harp & Valentine 2018). From these, the average fabric angle and fabric strength were calculated using circular statistics (see Harp & Valentine (2018) Supplementary Material 1). Calculated fabric angles do not compensate for the 7° southeast post-emplacement tilting. The minor amount of tilting is unlikely to impact our results since the strikes of Dike A and S are oblique to the

Figure 2.2. Sampling to final image analysis workflow. **(A)** Example of glassy margin sampled in the field, and margin-parallel thin section orientation relative to outcrop. **(B)** Modified plain light image of an oriented thin section for Dike A. **(C)** Binary image of the same thin section in **(B)** with crystals isolated and prepared for crystal angle analysis. **(D)** Output rose diagram for the 10% largest, highest aspect ratio crystals from the binary thin section in **(C)**. 0° is oriented toward the central intrusive complex, 90° is oriented up, and 180° is oriented toward the distal volcano flanks. The number of crystals within a given binned range of angles are denoted by the interior circles. This thin section has a strong, near horizontal flow fabric angle (1°, *R*-value=0.64, *n*=176)

direction of tilt, and angle corrections would be much less than 7°. Fabric strength in each thin section was computed from the resultant vector of the crystal angles (*R*-value), with values ranging from 1 (total crystal alignment) to 0 (random distribution), and n-values referring to the number of crystals analyzed. *R*-values >0.2 were deemed statistically significant, following Harp & Valentine (2018). For dike-scale analysis, *R*-values were clustered from individual sample means, with n-values indicating how many thin sections were considered.

Fabric angles were plotted on rose diagrams where 0° is toward the CIC, 90° is up, and 180° is toward the flanks (Fig. 2.2D). Crystal angles were divided into 18 bins on the upper hemisphere and projected into the lower hemisphere. Fabric angles were categorized as low-angle (>0° to <30° and >150° to <180°), inclined (>30° to <60° and >120° to <150°), or high-angle (>60° to <120°; Harp & Valentine 2018). Angles >0° to <90° were defined as outward plunging and >90° to <180° as inward plunging (Fig. 2.2).

2.3.3 Magma Properties

Magma properties including bulk chemical composition, density and porosity were characterized along both dikes. The bulk density was determined using the Archimedes principle on 70-85 cm^3 sample cubes cut to avoid visible fractures, with porosity measured using an AccuPyc II 1340 Helium Pycnometer (100 cm^3 reference chamber). A corresponding portion of each sample was powdered and analyzed using a 10 cm^3 chamber. Total porosity and solid density were calculated (Klug & Cashman 1994; Formenti & Druitt 2003), with bulk and solid density errors <1% and porosity errors <5%. Backscatter electron imaging on carbon-coated thin sections using a ThermoScientific Apreo 2 Scanning Electron Microscope (SEM) was conducted in order to distinguish between primary porosity (e.g. deformed vesicles) and secondary porosity (e.g., post-emplacement fractures).

X-ray fluorescence spectroscopy (XRF) was used to analyze bulk rock compositions at Washington State University's Geoanalytical Lab. Samples included margin samples from the proximal, medial, and distal segments of each dike, as well as proximal and distal interiors. Bulk rock geochemistry was used to correlate dike segments and to inform calculations of melt density (Iacovino & Till 2019).

Melt density calculations required estimates of the magma pressure, temperature, and dissolved water concentration. To estimate magma pressure, we utilize the definition of magma overpressure as the difference between the absolute magma pressure and the dike-normal stress. Using a paleodepth range of 0-1.65 km for the dikes from Moats (1990) to represent the depths for the most distal and proximal outcrops gives a range in confining pressure of ~0-40 MPa (for host-rock density of 2500 kg/m^3). We note that this upper bound of pressure is likely an overestimate given that the confining pressure within a volcanic edifice should be a fraction of the vertical, lithostatic stress (McTigue & Mel 1987). However, we use these values to capture the full range of possible confining pressures acting on the dikes, as the exact values of confining stress within an edifice are indeterminate. Poland et al. (2008) use an elastic fracture model to find the overpressure in each dike that best fits the thickness distribution. For Dikes A and S, they find best-fitting constant overpressure values ranging from ~8-40 MPa. Adding the confining pressure leads to magma pressures ranging from ~8-80 MPa, and we used this range of magma pressure as input to the melt density model to capture the full range in possible values. We used a temperature range of 700°-900° C and dissolved water contents of 1.0 to 3.9 wt.% based on a solubility model for water in rhyolite (Liu et al. 2005).

We ultimately constrain the bulk magma density (melt + crystals + gas), using a weighted average of the phases present as constrained by our textural analysis (crystal fraction and porosity):

Eq. 1
$$\rho_{\mathrm{magma}} = \varepsilon_{\mathrm{m}}\rho_{\mathrm{m}} + \varepsilon_{\mathrm{x}}\rho_{\mathrm{x}} + \varepsilon_{\mathrm{g}}\rho_{\mathrm{g}}$$

Here, ρ_m, ρ_x, and ρ_g represent the melt density, crystal density, and gas density respectively, and ε_m, ρ_x, and ρ_g are the melt, crystal, and gas volume fraction in the magma respectively. A range in ρ_m comes from our calculated melt densities. We assume ρ_x = 2600 kg/m^3 based on the density of plagioclase, the dominant phenocryst in our samples. We use a Redlich-Kwong equation of state for water based on Huber et al. (2010) for pressures from 8-80 MPa and temperatures from 700°-900° C, which results in a range in ρ_g of ~170- 380 kg/m^3. We use values for ρ_g based on sample porosity measurements. To estimate crystal volume (area) fraction, we traced crystals in an area representing ≥10% of the full thin section area using Adobe Illustrator and processed binary images in ImageJ. We analyzed 6 thin sections for Dike S and 3 for Dike A. In general, our crystal fraction analysis revealed remarkably constant values,

with an average of 31% +/- 0.03%, and so we take $\rho_x = 0.3$ to be representative of all samples.

2.4 RESULTS

2.4.1 Magma composition

Dike A's bulk rock geochemistry shows a consistently trachyte composition, averaging 65.2 ± 0.3 wt.% SiO2 (Appendix A, Table A.1). Little differences exist between margin and interior samples, with margins averaging 65.0 ± 0.3 wt.% SiO2, while interiors average 65.3 ± 0.3 wt.% SiO2. Dike S transitions from rhyodacite in the proximal segment to rhyolite distally, averaging 69.5 ± 0.7 wt.% SiO2 (Appendix A, Table A.2). Margins average 69.1 ± 0.6 wt.% SiO2, while interiors average 70.0 ± 0.3 wt.% SiO2. Geochemistry confirms that the distal segments of Dike S are correlated with the proximal segment and are not related to the two shorter dikes directly north of Dike S, which had lower SiO2 measurements (66.6 wt.% and 57.7 wt.%).

2.4.2 Flow Fabrics

2.4.2.1 Dike A

Of the 16 margin thin sections analyzed for Dike A, 15 had statistically significant fabrics with *R*-values ranging from 0.23-0.64. Full details are reported in Table 2.1, and selected representative samples for each segment are graphically shown on Figure 2.3. All 10 interior samples had significant fabrics (*R*=0.25-0.58). Dike A primarily displays inward-plunging, low-angle fabrics in both margins and interiors, with a mean flow-angle of 166° (*R*=0.55, *n*=25). The mean margin flow-angle is 167° (*R*=0.57, *n*=15), and the mean interior flow-angle is 164° (*R*=0.53, *n*=10). This low-angle trend persists from the proximal to the distal portions of the dike, with subtle variation between the three largest segments (proximal, medial, and distal) (Fig. 2.3). In the proximal segment, both margins and interiors have dominantly low-angle flow fabrics (Fig. 2.3A). In the medial segment, margin fabrics are on average more inclined, while interior fabrics remain low-angle but more inclined than in the proximal and distal segments. (Fig. 2.3B). In the distal segment, both margin and interior fabrics return to low-angles (Fig. 2.3C).

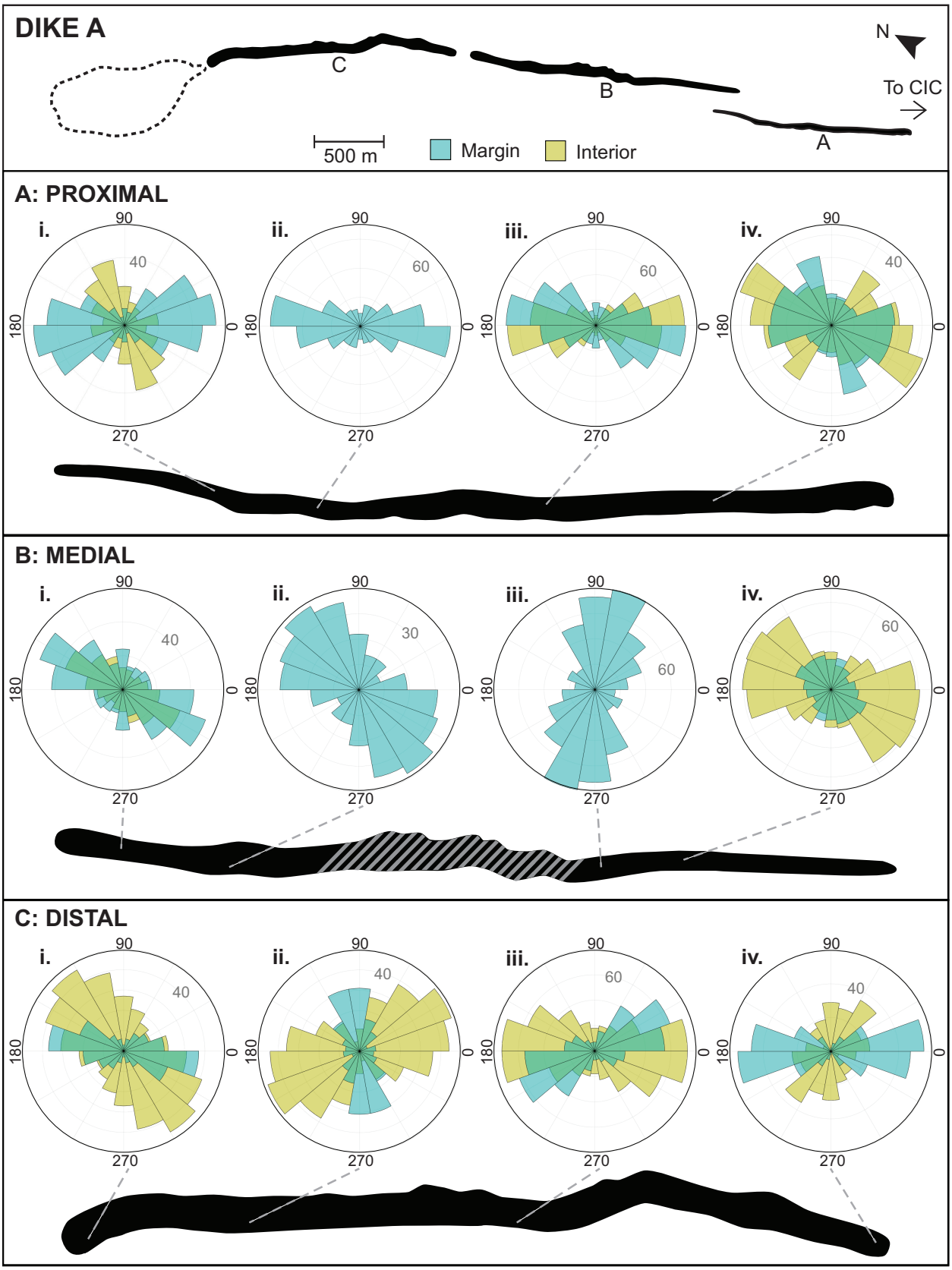
DIKE A
N
To CIC
C
B
A
500 m
Margin
Interior
A: PROXIMAL
i.
ii.
iii.
iv.
B: MEDIAL
i.
ii.
iii.
iv.
C: DISTAL
i.
ii.
iii.
iv.
90
180
0
270
40
60
30

Figure 2.3. ***(Previous Page)*** Diagram of significant flow fabrics for selected representative sampling locations along Dike A. Margin fabrics are shown in teal, and interior fabrics are shown in green for the **(A)** proximal segment, **(B)** medial segment, and **(C)** distal segment excluding the laccolith. The central intrusive complex is located to the right, and the distal flanks to the left in each segment diagram. The widening region in the medial segment **(B)** is denoted by grey stripes

Inclined and high-angle margin fabrics occur near segment ends or, in the medial segment, at areas of anomalous widening and small-scale segmentation (Fig. 2.3B.ii, iii). An exception is found at one distal location. Interior inclined fabrics are almost exclusively located at segment ends. Margin and interior samples from the same location do not exhibit systematic correlations in flow direction or plunging trend, with fabrics varying between 10° and 90° (Fig. 2.3B.i).

2.4.2.2 Dike S

Ten out of 15 margin thin sections analyzed for Dike S had significant flow fabrics (R=0.22-0.52). Seven of the ten interior samples also had significant fabrics (R=0.20-0.48). Overall, Dike S displays dominantly inclined to high-angle fabrics, with an average flow-angle of 115° (average R=0.35). Margins exhibit an average flow-angle of 125° (R=0.36, n=10), while interiors show a mean high-angle fabric of 103° (R=0.40, n=7).

Margin fabrics shift abruptly from low-angle in the proximal segment to dominantly high-angle in the medial and distal segments (Table 2.2; Fig. 2.4). By comparison, interior fabrics are consistently high-angle along all segments (Table 2.2; Fig. 2.4). At the most distal sampling location, where the dike abruptly widens and ends, neither margin nor interior fabrics are significant (Fig. 2.4 C.i). As with Dike A, no systematic correlation exists between interior and margin flow fabrics in terms of angle or plunge direction.

2.4.3 Magma density and porosity

2.4.3.1 Dike A

The average bulk density of 26 Dike A samples is 2482 ± 89 kg/m³, while solid density (crystals and glass only) averages 2661 ± 47 kg/m³. Margins exhibit a bulk density of 2474 ± 95 kg/m³, and a solid density of 2648 ± 38 kg/m³. Interiors have a bulk density of 2493 ± 82 kg/m³ and a solid density

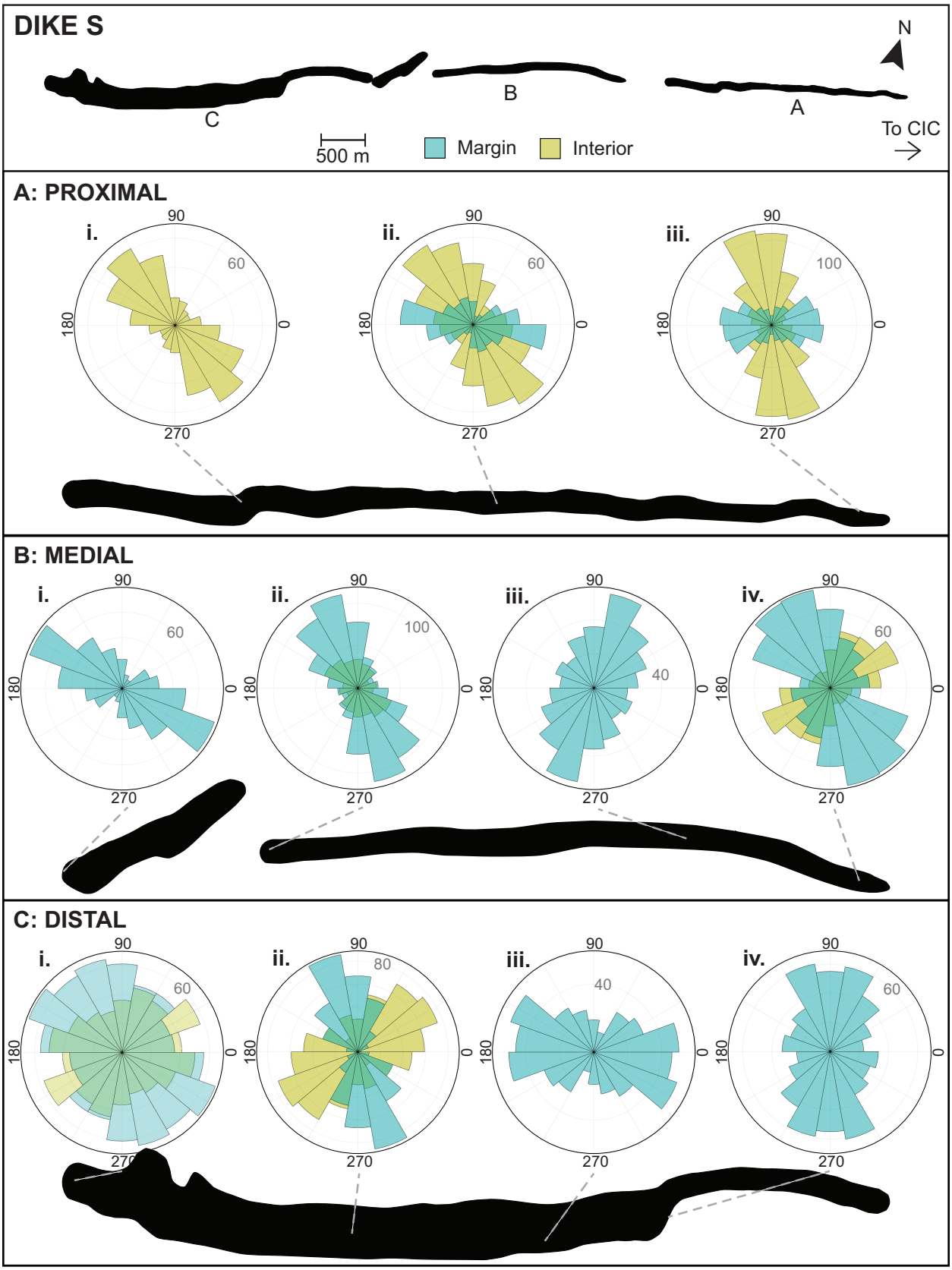
DIKE S
N
C
B
A
500 m
Margin
Interior
To CIC
A: PROXIMAL
i.
ii.
iii.
B: MEDIAL
i.
ii.
iii.
iv.
C: DISTAL
i.
ii.
iii.
iv.
90
180
0
270
60
100
40
80

Figure 2.4. ***(Previous Page)*** Diagram of significant flow fabrics for selected representative sampling locations along Dike S. Margin fabrics are shown in teal, and interior fabrics are shown in green for the **(A)** proximal segment, **(B)** medial segment, and **(C)** distal segment. The central intrusive complex is located to the right, and the distal flanks to the left in each segment diagram. The most distal rose diagram **(C.i)** does not have a significant R-value, but is included to show flow behavior at the inferred most distal portion of the dike

of 2683 ± 52 kg/m³. There are no systematic changes in either bulk or solid density with position along the length of the dike, for either margins or interiors (Fig. 2.5A). Bulk density variation (up to 373 kg/m³) exceeds that of solid density variation (up to 182 kg/m³), reflecting porosity differences. Porosity ranges from 0.63% to 15.57% and averages 6.75 ± 3.61%, with margin porosity at 6.55 ± 3.98% and interior porosity at 7.05 ± 3.10%. No discernible correlations exist between the porosity of margin samples and position along the length of Dike A (Fig. 2.6A). However, the interior samples have higher porosities in the medial segment than in the proximal or distal segments (Fig. 2.6A). There is no consistent pattern in whether the margin or interior at the same location has higher porosity. Of the 10 locations with pycnometry data for both, five margins had a higher porosity than the interiors, while the other five had lower porosity.

Melt densities were calculated for the highest and lowest SiO_2 samples using pressures from 8-80 MPa and temperatures from 700°-900° C (Iacovino & Till 2019). Changing the dissolved H_2O content from 3.9 wt.% to 1.1 wt.% (reflecting saturated conditions at the high-pressure and low-pressure ends, respectively) changes the calculated melt density range from 2301-2368 kg/m³ to 2421-2477 kg/m³ (Fig. 2.5A).

Combining the full range of melt density (2301-2477 kg/m³) with the measured porosity plus and minus one standard deviation gives bulk magma densities ranging from 2170-2448 kg/m³ (Fig. 2.5A). Here, the large spread in magma density is owing primarily to the range in assumed gas fraction.

2.4.3.2 Dike S

The bulk density of 25 Dike S samples averages 2437 ± 64 kg/m³, while solid density averages 2600 ± 42 kg/m³. Margins have a bulk density averaging 2446 ± 50 kg/m³, with solid density of 2594 ± 21 kg/m³. Interiors have a bulk density of 2426 ± 81 kg/m³ and a solid density of 2607 ± 58 kg/m³. Although there is no trend in the margin or interior solid density with position along the length of the

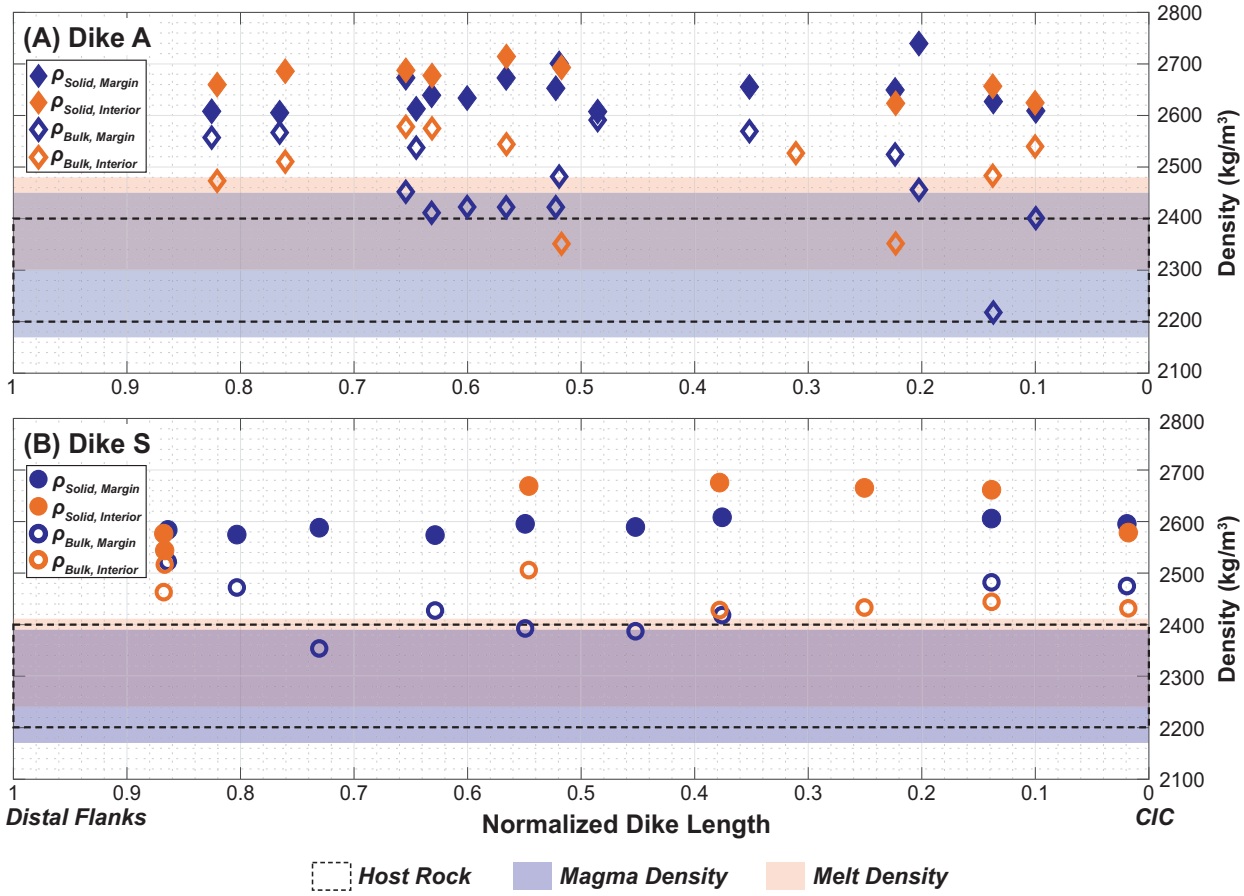

Figure 2.5. Graphs of measured sample bulk density (ρ_{bulk}), sample solid density (ρ_{solid}), calculated host rock, magma, and melt density (kg/m³). Samples are plotted along the normalized dike length, with 0 near the central intrusive complex, and 1 at the distal flanks. **(A)** Dike A solid density measurements are marked by filled diamonds and bulk density measurements by open diamonds (blue for margins, orange for interiors). **(B)** Dike S solid density measurements are marked by filled circles and bulk density measurements by open circles (blue for margins, orange for interiors). The melt density range for each dike is shown by the light orange rectangle, and magma density range by the light purple rectangle. The host rock density range is outlined by a black dashed box

dike, there does appear to be a systematic decrease in the margin bulk density from the proximal to the medial segment, and then a systematic increase in bulk density again moving from the medial to the distal segment (Fig. 2.5B). These variations in bulk density correlate with changes in porosity, reflecting that porosity is the dominant control on the bulk density in our samples.

Porosity ranges from 1.08% up to 11.36% with an average of 6.23 ± 2.54%. Dike margins average 5.68 ± 2.21%, while interiors average 6.92 ± 2.87%. Porosity for Dike S samples follows a trend of higher porosity in the medial portions and lower porosity at proximal and distal dike ends for both the margins and interiors (Fig. 2.6B). Interiors also have higher porosities than margins at eight of 11 locations.

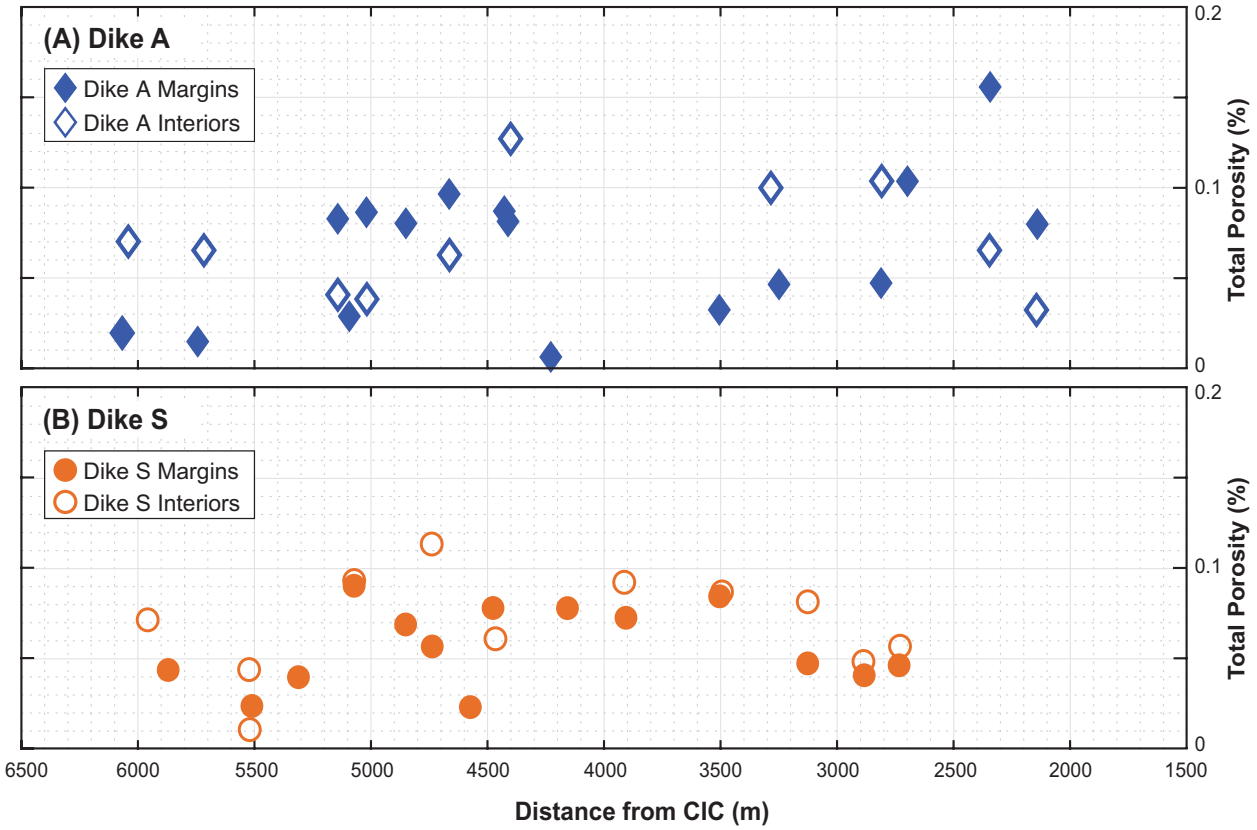

Figure 2.6. Total measured porosity (%) along the length of the dikes, measured from the CIC. Dike A samples are denoted by purple diamonds (solid for margins, open for interiors), and Dike S samples are denoted by orange circles (solid for margins, open for interiors). Error bars are less than 5% of the value of measured porosity for all samples, and are smaller than the marker size

Melt densities using the same conditions as Dike A were found to range from 2243-2309 kg/m^3 for 3.9 wt.% dissolved H2O to 2355-2410 kg/m^3 for 1.1 wt.% H2O. Using the measured porosity as a proxy for gas fraction (± one standard deviation) gives an estimated magma density of 2169-2391 kg/m^3 (Fig. 2.5B)

2.4.4 The source of porosity

Vesicles and fractures are visible in Dikes A and S at both outcrop and thin section scales. At the outcrop scale, bubble trains preserved in both margins and interiors are interpreted to record pre- or syn-emplacement vesiculation. Extensive fractures, oriented both parallel and perpendicular to the dike strike, are interpreted as post-emplacement cooling joints. Samples for porosity and thin section analysis were cut to avoid visible fractures wherever possible. In thin section, we observe elongated vesicles (0.5

to <3 mm) aligned with the inferred magma flow direction (Fig. 2.7A). These vesicles are generally void of minerals, though partial mineralization is visible at the micro-scale (Fig. 2.7C). There is no evidence of post-emplacement bubble growth in either the dike margins or interiors. Thus, we believe that vesicles record the minimum porosity at the time of magma intrusion.

Some samples from Dikes A and S lack visible vesicles, but at the micro-scale show abundant microfractures cutting microlites (Fig. 2.7B). In some cases, microlites extend across these fractures, which suggests that the fractures formed during post-emplacement cooling and contraction (Fig. 2.7B). Another common feature in both dikes is microlites nearly surrounded by pore space (Fig. 2.7D), which may represent localized contraction in microlite-rich regions that did not induce fracturing. Observations across scales suggest vesicles account for the majority of measured porosity, while the porosity in the lowest-porosity samples primarily results from post-emplacement contraction-induced microfractures.

2.4.5 Host rock density and magma buoyancy

Samples of the host rock basaltic-andesite breccia collected around the volcano have bulk densities ranging from 2206 ± 16 to 2385 ± 9 kg/m^3. Because the host rock samples include both scoriaceous materials and lava fragments, we take this density range to represent the full range of host-rock density that intruding magmas could have encountered at this level within the volcano. If we take the bulk density of rock samples from Dikes A and S (2482 ± 89 kg/m^3 and 2437 ± 64 kg/m^3) to represent the magma density during intrusion, the magmas in both dikes would have been negatively buoyant at this level of exposure (Fig. 2.5). However, if we account for the fact that the liquid melt would have had a lower density than the present-day glass and use our range of calculated magma densities as representative (2170-2448 kg/m^3 for Dike A and 2169-2391 kg/m^3 for Dike S), the magma densities for both dikes completely overlap those of the host rock (Fig. 2.5), meaning that the magmas may have been closer to neutrally buoyant with small-scale variations in buoyancy owing primarily to variations in the magmatic gas fraction.

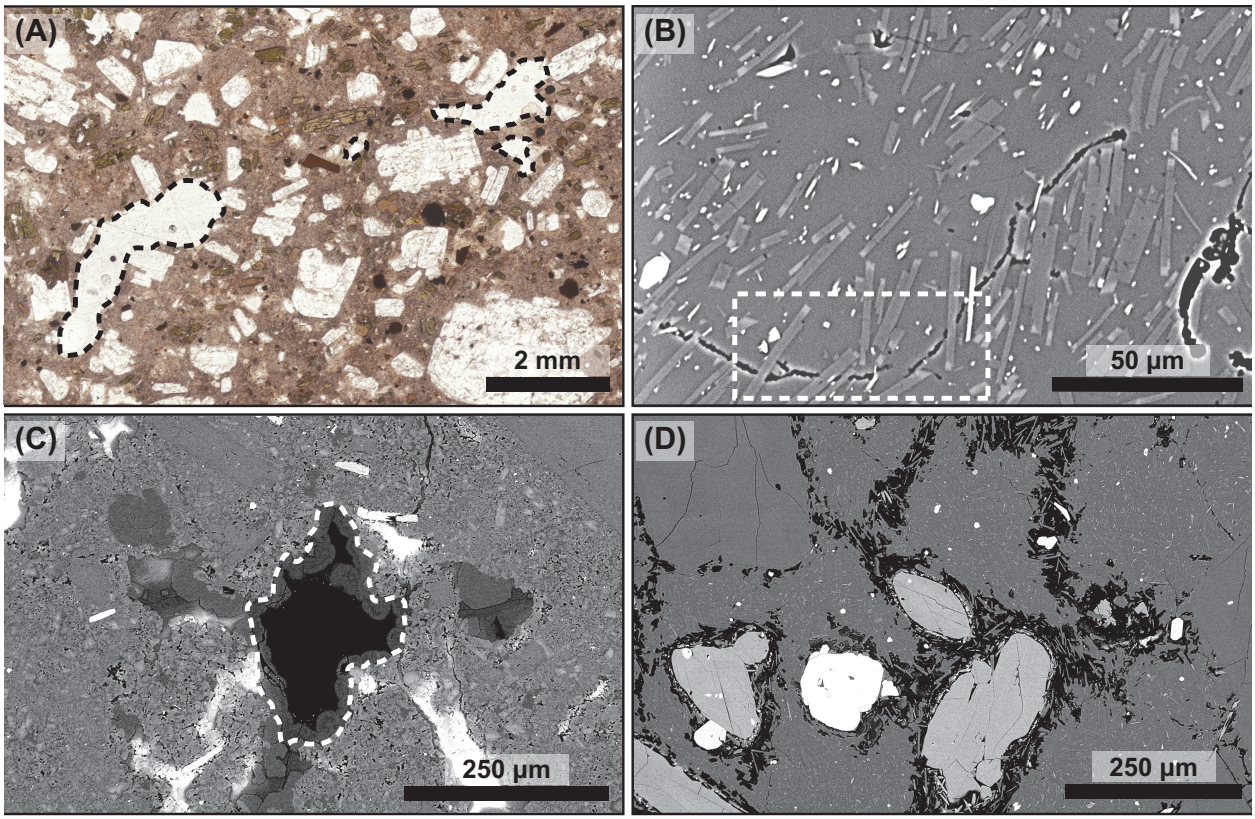

Figure 2.7. Thin section imagery depicting pores and fractures observed at various scales. **(A)** Plane light image of Dike A sample 9-1 with pore space outlined in dashed black lines. **(B)** SEM-BSE image of Dike A thin section 16-1 showing microlites bridging and unbroken by a fracture, in the white dashed box. **(C)** SEM-BSE image of Dike S sample 13-1 with pore space in black, outlined by dashed white line. Grey material within the outline is interpreted to be post-emplacement precipitate. **(D)** Void space around phenocrysts in an SEM-BSE image of Dike A sample 14-3, indicative of post-emplacement contractional pores

2.5 DISCUSSION

2.5.1 Dike Propagation and Magma Flow Directions

The flow fabrics in Dikes A and S differ significantly along their lengths, both at the margins and interiors. Dike A, apart from segment ends, has predominantly low-angle margin fabrics (167°) along its entire length (Fig. 2.3). This suggests that the initial propagation phase at this exposure level was dominantly lateral, extending from the CIC to the flanks. Similarly, low-angle fabrics in the interior of Dike A (164°) (Fig. 2.3) indicate sustained lateral magma flow until final solidification. However, inclined to subvertical flow fabrics are observed within the highly segmented and widened portion of the medial segment of Dike A (between ~3.8 – 4.7 km from the CIC) (Fig. 2.3B). This widened section, previously interpreted as a portion of the dike which fed a localized eruptive vent (Moats

1990; Poland et al. 2008), may have formed through inelastic processes such as thermal and mechanical erosion of the conduit. High-angle flow fabrics near this area support magma flow toward a surface vent, which could have sustained magma flow for longer leading to conduit erosion (Fig. 2.3B). Nevertheless, given the extent of Dike A more than 2 km beyond this region, the low-angle fabrics in distal segments, and the laccolith structure at the dike's distal end, we suggest that the eruptive portion represents a minor component of this primarily intrusive structure.

In Dike S, the low-angle margin fabrics in the proximal segment (176°) support initial lateral propagation, consistent with the interpretation of Poland et al. (2004) based on AMS data from this segment. However, higher-angle margin fabrics in the medial and distal segments (112°) indicate a transition from lateral to inclined flow. If margin fabrics preserve the initial stages of propagation, this transition likely began near the start of the medial segment (~3.4 km from the CIC) (Fig. 2.4). If instead we assume that the dike propagated laterally to its distal segment, like Dike A, the inclined margin fabrics in the medial and distal segments could only result from later-stage magma replacing the original margin material, which would be accompanied by host-rock erosion. Evidence for erosion would include host-rock xenoliths incorporated into the dike (Townsend et al. 2015), which we have not observed. Instead, we favor an interpretation that dike propagation transitioned from lateral to inclined as it encountered changes in the driving and/or resisting forces farther from the CIC.

The thickness of the distal segment provides further insights into the evolution of Dike S. The elastic fracture model of Poland et al. (2008), which provides an explanation for the geometry of many Summer Coon dikes, does not account for the abrupt doubling of thickness in the distal segment (Appendix A, Fig. A.4). This anomaly is better explained by inelastic widening, potentially caused by host-rock erosion during sustained localized flow at an eruptive vent. In this scenario, high-angle margin fabrics in the distal segment would reflect magma flow during conduit widening rather than initial propagation. However, as noted, there is no evidence of widespread erosion. Another possibility is that widening resulted from changes in host-rock rheology (e.g., rocks becoming less stiff closer to the surface) or near-surface stress, causing "flaring" or widening of the dike as it nears the paleo-surface (Geshi et al. 2010). Similar flaring has been documented in feeder dikes from other eroded volcanic

edifices (e.g., Keating et al. 2008; Friese et al. 2013; Harp & Valentine 2015). In this scenario, margin fabrics could preserve the original dike propagation direction. Regardless, the anomalous widening of the distal segment strongly suggests an eruptive vent. We propose that Dike S was a feeder dike for a flank eruption located ~5 – 5.7 km from the summit. The high-angle interior fabrics (103°) along the entire dike length support a final phase of vertical magma flow, consistent with eruptive vents opening along the entire trace of the dike. However, we cannot exclude the possibility that vertical flow within the proximal and medial segments terminated in the shallow subsurface above the level of exposure.

2.5.2 Topographic Stresses, Magma Buoyancy, and the Role of Magmatic Volatiles

To a first order, our interpretations of the new flow fabric data presented here align with Poland et al. (2008), who proposed that silicic dikes at Summer Coon rose vertically from a reservoir beneath the volcano before transitioning to lateral propagation at the interface between the volcanic cone and basement. Poland et al. (2008) suggested this transition resulted from a combination of a stress barrier and neutral buoyancy. Our new data, combined with estimates of magma properties, allow further exploration of this mechanism for lateral propagation at the current level of exposure.

At Summer Coon, the most obvious source of a stress barrier is the load of the large (~2.2 km tall, ~7 km radius) volcanic cone. Pinel and Jaupart (2000) proposed a critical magma density (ρ_{crit}) above which ascending magmas are trapped by the weight of the volcano and below which magmas continue to ascend into the edifice and erupt near the summit:

Eq. 2

$$\rho_{crit} = 2\frac{\Delta P_0 + \rho_c g h}{g(h_v(1+2\nu)+2h)}$$

In their equation, ρ_c is the density of the basement rock, g is the acceleration due to gravity, h is the depth beneath the volcanic edifice to the magma reservoir feeding the dike, ΔP_0 is the overpressure in the reservoir at the dike inlet, h_v is the height of the volcanic cone above the basement, and ν is Poisson's Ratio. To estimate the critical magma density at Summer Coon, we use h_v = 2.2 km, based on reconstruction of the volcanic cone by Moats (1990). We use ΔP_0 = 20 MPa based on the critical overpressure to propagate a dike from a shallow silicic reservoir (Rubin 1995a; Jellinek & Depaolo

2003), and a range in h from 6-10 km based on typical depths of silicic magma reservoirs (Huber et al. 2019). The crustal structure beneath the ancient Summer Coon edifice includes an upper layer of Paleogene volcanics and volcaniclastic rocks (~1.2 km thick) that overlies Cretaceous sedimentary rocks including shales and sandstones (Gries 1985). If we use $\nu = 0.25$ and take a range in ρ_c from 2200-2800 kg/m³ based on reference values for general sedimentary rocks (Clark 1966), this leads to a range in ρ_{crit} of 1992-2578 kg/m³. Our calculated ranges in magma density for Dike A (2170-2448 kg/m³) and Dike S (2169-2391 kg/m³) fall entirely within and near the middle of the range of ρ_{crit}. Thus, it is plausible that the lateral propagation of Dike A and the initially lateral propagation in the proximal section of Dike S are explained by insufficient buoyancy to overcome the stress barrier posed by the weight of the cone. However, without better constraints on the crustal density structure beneath the ancient Summer Coon edifice, this model is difficult to evaluate. Furthermore, the models of Pinel and Jaupart (2000; 2004) do not consider dike propagation within the volcanic edifice itself but predict that a dike will either ascend through the volcanic edifice and erupt in the focal area or propagate along a lateral path contained entirely beneath the base of the edifice. Observations of both dikes propagating laterally within the edifice challenge these predictions, highlighting the need for future work to model dike propagation within the large topography of a stratovolcano.

2.5.3 Transition to inclined propagation in Dike S

The abrupt shift from lateral to inclined propagation in Dike S at ~3.4 km from the CIC remains unexplained. One possibility is that compressive stress within the cone decreased with distance, allowing vertical ascent. A similar transition in Dike A at ~3.8 km distance aligns with its interpreted eruptive vent, suggesting a critical radial distance from the center of a volcanic cone (corresponding to a critical dike-normal stress) at which dikes may shift from lateral to vertical propagation. Without models for stress within the large topography of a volcanic cone, this hypothesis is difficult to test. More flow fabric data from other silicic dikes at Summer Coon, and data from active stratovolcanoes on the elevations of eruptive vents, could shed light on this hypothesis.

Alternatively, the magmatic volatile fraction may have influenced buoyancy, such that increasing

bubble fractions in the intruding magma caused the magma to cross a critical density and transition to inclined flow. Our analysis of dike margin samples from the proximal and medial segments reveals a strong negative correlation ($R^2 = 0.92$, $n = 7$) between flow-angle and bulk density (Fig. 2.8). As bulk density correlates with porosity, primarily from vesicles formed by gas that exsolved pre- or syn-emplacement, volatile fraction likely enhanced buoyancy, which could have enabled vertical flow in Dike S. The significantly lower porosity in samples from the distal segment, which nonetheless record higher-angle flow, may be explained by our interpretation that this segment was an eruptive vent that openly degassed during eruption. A similar analysis of dike margin samples from Dike A reveals no significant correlation between bulk density and flow-angle, although the bulk density values are largely greater than those in Dike S that correspond to higher flow-angles. Thus, it could have been the case that the magma in Dike A never reached a low enough density to achieve high-angle propagation along most of its length.

2.5.4 Future work

The high-resolution flow fabric data presented here reveal that dike propagation trajectories within stratocones can vary substantially. Some dikes, like Dike A, exhibit consistently lateral propagation to the most distal flanks, while others, like Dike S, transition from lateral to vertical flow at intermediate distances from the volcanic center. These observations underscore the need to better understand variability in dike pathways within stratovolcanoes, as these trajectories ultimately dictate the location of eruptive vents.

The inclined dike margin fabrics observed between ~3.4-3.8 km distance from the CIC in both dikes raise the intriguing possibility of a critical radial distance from a volcanic center where lateral dike propagation transitions to inclined flow. However, our study was limited to two well-exposed dikes. Additional flow fabric data from more of the radial silicic dikes at Summer Coon could clarify whether this pattern is consistent across the system. Furthermore, comparison to other exposed radial dike systems (e.g. Spanish Peaks) could shed light on the ubiquity of this pattern.

Furthermore, the porosity data from Dike S suggest that magmatic volatile fraction may

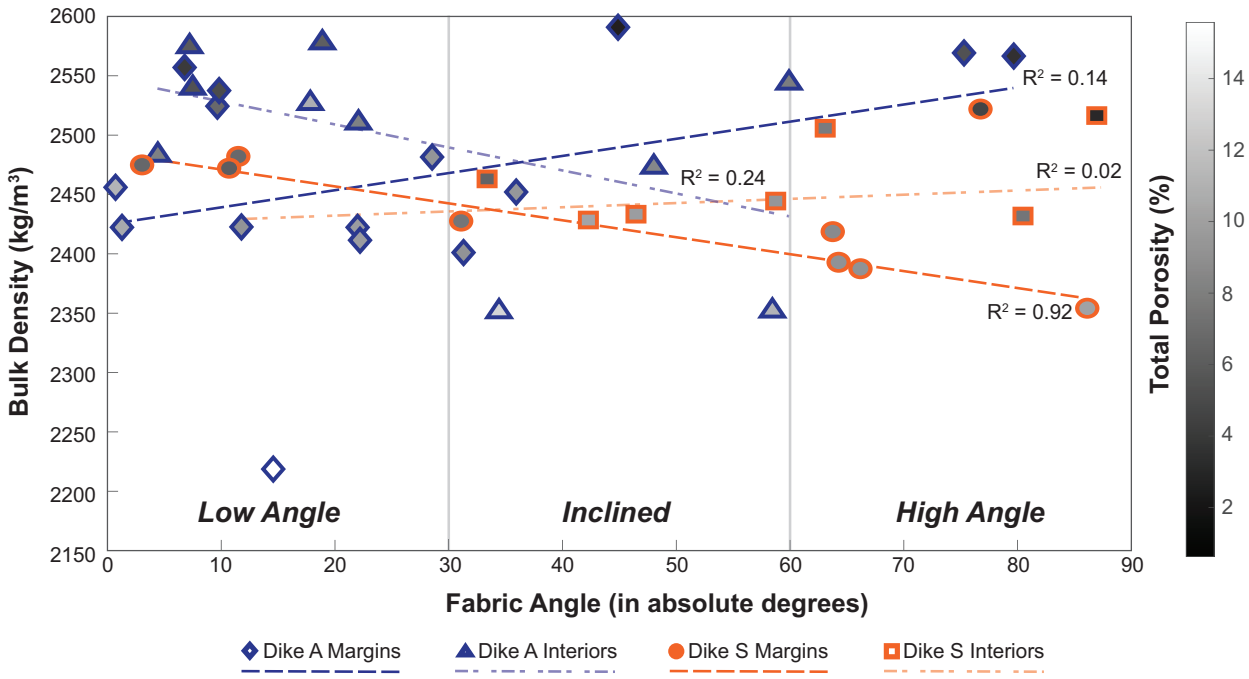

Figure 2.8. Correlation between measured bulk density (kg/m³), total porosity (%), and flow fabric angles normalized to 0°-90°. Dike A margin measurements are noted by purple diamonds, and interiors by purple triangles. Dike S margin measurements are noted by orange circles, and interiors by squares. Symbols are colored according to the total porosity measured for each sample, with fill colors corresponding to the color bar. Bounds for low-angle, inclined, and high-angle fabrics are noted. Trendlines correlating density to fabric angle and corresponding R^2 values are shown in purple for Dike A and orange for Dike S. Margin trendlines are presented for the non-widening portions of each dike, where original fabrics are interpreted to be preserved for propagation in an elastic regime

play a role in influencing dike trajectories. Future studies on the dikes at Summer Coon and other stratovolcanoes could test whether magma bubble fraction serves as a primary driver of dike pathways. Investigating the causes of systematic changes in magma porosity – such as the tapping of a reservoir with heterogeneous bubble distributions, volatile exsolution during intrusion, or variable outgassing during intrusion – would provide critical insights.

Finally, the hypotheses presented here should be further tested by integrating field data with physics-based models. Existing models, however, are not well-suited to consider the complex history and evolution of stress at a stratovolcano, as they typically only capture the stress state at a single snapshot in time (e.g., Chadwick & Dieterich 1995; Pinel and Jaupart 2000; Maccaferri et al 2011; Corbi et al 2015; Mantiloni et al 2023). Volcanic and tectonic processes continually change the local stress field; for example, over short timescales, surface processes like lava flows, dome growth, and flank or caldera

collapse can result in an abrupt change to the surface load, yet over longer timescales processes such as faulting or viscous creep in warm crust can partly relax stresses. In addition, the process of dike and sill intrusion would, over multiple intrusion events, progressively alter the local stress field (Rubin et al 1987; Davis et al 2021). Field data, such as the dike geometries and propagation directions presented here, provide valuable constraints for such models. Further work to track how dike geometries and trajectories change over time, coupled with geochemical data on the timing of compositional changes, would improve our ability to reconstruct how an evolving stress field influences magma transport. Comparing these integrated datasets across multiple volcanic systems would ultimately allow us to identify broader patterns of magma transport and stratovolcano evolution.

2.6 CONCLUSIONS

We revisited two of the best-exposed silicic dikes at Summer Coon volcano, CO, to reconstruct magma transport pathways and analyze the evolution of magma flow during dike intrusion. By correlating variations in flow directions with magma density and porosity, we explored the factors influencing dike propagation. Propagation pathways for these large silicic dikes are variable. Dike A intruded in a dominantly lateral direction over its 5.25-km length, while Dike S transitioned from lateral to inclined and vertical emplacement. Flow patterns near segment ends and at anomalously widened areas are more variable but do not represent the dominant propagation trajectory of the dikes. For Dike S, a negative correlation between flow-angles at the margins and measured bulk density – primarily influenced by vesicle fraction – suggests that magma bubble content may influence dike pathways in the shallow subsurface. This relationship, however, was not observed in Dike A. The lateral propagation of both dikes in the proximal segments may reflect the influence of edifice stresses acting as a buoyancy filter, consistent with predictions by Pinel & Jaupart (2004). The shift to more vertical propagation in medial and distal segments of Dike S may be related to changes in buoyancy forces during emplacement or variations in confining stress with increasing distance from the volcanic center. Our findings emphasize the importance of comprehensive sampling along entire dike lengths to adequately characterize dike propagation patterns and the utility of sampling dike interiors to capture

the full evolution of intrusion. While this study provides insight into the role of magma properties on influencing buoyancy during dike emplacement, a larger comparison with other dikes at Summer Coon, combined with numerical modeling of edifice stresses and dike propagation, are essential to address the remaining questions.

2.7 BRIDGE

In the preceding work, I found that two of the large silicic dikes at Summer Coon record dominantly lateral propagation in segments proximal to the volcanic center. However, these dikes diverge in trajectories distally, with Dike A maintaining dominantly lateral flow along its entire length, and Dike S shifting to inclined and near-vertical flow toward the flanks. This shift in Dike S may be correlated to its greater buoyancy compared to Dike A, due in part to a higher-silica composition and a lower density, influenced by the magma porosity. Field observations directly informed my conclusions in this chapter, however active magmatic processes like volatile exsolution and outgassing, or direct measurements of the paleo-edifice stress field, cannot be made from field deposits. In the succeeding chapter, I combine field measurements of porosity with numerical modeling to explore how compositional variation and dynamic processes occurring within the dikes during propagation in Summer Coon's edifice could have encouraged the proximally lateral propagation inferred from this work.


mostly
GASLESS

CHAPTER 3

Mostly gasless: The impact of volatile exsolution and outgassing on the depth and height of lateral dikes beneath a volcanic edifice

This work was conducted in collaboration with Meredith Townsend, Kate Scholz, and Andrew Harp

3.1 INTRODUCTION

Lateral dike propagation is a common process at stratovolcanoes, where lateral intrusions create radial dike swarms, and produce flank eruptions that can occur at lower elevation on the volcanic flanks, far from the summit, posing unique hazards to surrounding communities. Prominent recent examples include the 2021 Nyiragongo eruption in the Democratic Republic of Congo, which produced a 25-km-long dike traveling at depths of less than 500 m beneath the city of Goma, and the 2023 Grindavík dike in Iceland, which propagated ~15 km at 1-5 km depth before arresting, but caused widespread damage through surface faulting above the dike (Sigmundsson et al., 2024; Smittarello et al., 2022). In these and many other examples (e.g., Miyakejima volcano, Piton de la Fournaise, Bárðarbunga), dikes propagated over long distances at a roughly constant depth range (Fukushima et al., 2005; Ueda et al., 2005; Woods et al., 2019). This pattern is thought to be promoted by the weight of the volcanic edifice (Acocella & Neri, 2009; Heimisson et al., 2015; Pinel & Jaupart, 2004), a level of neutral buoyancy in the shallow crust (Lister & Kerr, 1991; Ryan, 1988; Townsend et al., 2017; Walker, 1989) and/or the reduced confining pressures associated with volcanic rift zones inhibiting magma ascent (Pinel & Mériaux, 2025; Segall et al., 2001; Sigmundsson et al., 2024; Rubin & Pollard, 1987). Despite the variety of suggested factors driving lateral propagation, it remains poorly understood what ultimately controls the depth and height of lateral dikes, whether or not a lateral dike will stall or erupt, and if it erupts, the location and elevation of the lateral dike-fed vents on volcanic cones.

While external factors such as edifice load or tectonic stress have been widely studied, internal processes within the magma itself may also exert a strong influence on the propagation, depth, and geometry of lateral dikes intruding beneath stratovolcanoes. In particular, variations in magma density

driven by volatile exsolution and outgassing can dynamically alter the pressure conditions within the dike that govern its propagation. As magma leaves its source reservoir, it encounters confining pressure variations that influence volatile solubility, which can alter magma properties within the dike (Abdullin et al., 2024; Aksit et al., 2025; Geshi et al., 2020; Maimon et al., 2012; Rasmussen et al., 2022). For example, ascent from the reservoir or lateral propagation beneath a sloping volcano both lead magma to encounter lower confining pressure, which would promote volatile exsolution and bubble growth (e.g., Liu et al., 2005). This degassing lowers magma density and enhances buoyancy. The resulting increase in porosity can locally pressurize the dike where bubbles accumulate and change the conditions for fracture stability and propagation (Geshi et al., 2020). Conversely, outgassing during propagation, where bubbles escape into the surrounding host rock, can counteract this effect by reducing magma overpressure and buoyancy.

Volatile exsolution and outgassing are central processes in cylindrical conduit models of magma ascent (e.g., Burgisser et al., 2024; Gonnermann & Manga, 2003; Mastin & Ghiorso, 2000; Melnik & Sparks, 2005; Papale et al., 1998; Wong & Segall, 2019), where the evolution of bubble fraction critically controls eruption dynamics. In contrast, dike models – geometrically distinct from volcanic conduits in being tabular or penny-shaped cracks governed by fracture mechanics – have only recently begun to include volatile exsolution. Even so, most implementations are limited to simplified treatments of vertical ascent dynamics (e.g., Abdullin et al., 2024; Geshi et al., 2020; Taisne & Jaupart, 2011) and none include the effects of outgassing or volatile loss to the host rock. Alternatively, dike models may assume bubbles are decoupled from the magma, accumulate at the dike tip, and result in gas-cap-driven propagation (Lister, 1990; Maimon et al., 2012; Rubin, 1993). These oversimplifications ignore both field and petrologic observations of volatiles trapped in the magma syn-emplacement or syn-eruption (e.g., Allgood et al., 2025; Harp, 2021; Shea et al., 2010). Because dike propagation is governed by stress concentration at the fracture tips, which is highly sensitive to small variations in internal pressure and external stress, changes in magma density and buoyancy driven by volatile processes are expected to exert a disproportionately large influence on dike geometry and propagation.

Unraveling the role of degassing and outgassing in dike propagation is complicated by their

sensitivity to the surrounding stress field. At stratovolcanoes, where dikes intrude and erupt repeatedly over hundreds of thousands of years to build up a volcanic edifice, one of the primary factors altering the stress field is the topographic load of the edifice itself (Acocella & Neri, 2009; Pinel & Jaupart, 2000; Roman & Jaupart, 2014). The presence of a large edifice causes near-surface stresses to deviate from purely lithostatic conditions, with the gravitational stresses induced by the edifice governed by edifice height, basal radius, and the overall geometry (Goldman et al., 2022; Scholz, 2025). The load of the edifice may further act as a density or buoyancy filter for ascending magma, even without invoking internal magmatic processes such as exsolution (Pinel & Jaupart, 2000; 2004). Models of dike propagation under volcanic topography generally predict that the compressive stress concentration beneath the edifice should inhibit dikes from propagating into the edifice (Davis et al., 2020, 2021; Martel & Muller, 2000), in direct contradiction to widespread field and geophysical observations of intra-edifice propagation and flank eruptions (e.g., Fernandina volcano, Mt. Etna, Miyakejima volcano) (Acocella & Neri, 2009; Chadwick & Dieterich, 1995; Geshi et al., 2020). Incorporating volatile exsolution into models of dike propagation beneath volcanic edifices may help reconcile these discrepancies by allowing density- and pressure-driven feedbacks that could promote dike propagation within otherwise compressive stress regimes (Geshi et al., 2020).

Building on this hypothesis, we investigate how volatile exsolution and outgassing interact with edifice-induced stresses to influence the stability, depth, and geometry of laterally propagating dikes. While prior models have treated these processes separately, their combined effects likely contribute to whether magma intrudes entirely beneath the edifice, partially within the edifice, or erupts on the flanks. To address this gap, we combine field data on the textures and geometries of radial dikes with mechanical models for dikes subject to loading by a volcanic edifice and internal pressure variations related to volatile exsolution and outgassing. Measurements of vesicularity collected from multiple exposed dikes at Summer Coon volcano in Colorado provide a natural record of exsolution and outgassing during lateral intrusion beneath an ancient stratovolcano. These data are used to constrain a dike model designed to find the stable heights and depths of laterally-propagating dikes. Through this integrated approach, we aim to identify the conditions that allow kilometer-scale lateral propagation

of dikes within a large volcanic edifice, focusing on the role of magma composition, water content, and outgassing. Our results provide a physical basis for reconciling field observations of lateral dikes exposed within eroded stratovolcanoes and theoretical models. In addition, our findings improve our understanding of how volatile processes influence the geometry and depth of lateral dikes that can feed hazardous flank eruptions.

3.2 SUMMER COON BACKGROUND & FIELD DATA ANALYSIS

3.2.1 Silicic Dikes at Summer Coon

Summer Coon volcano, in south-central Colorado, was active in the Oligocene during the pre-ignimbrite phase of San Juan Volcanic Field magmatism (Fig. 3.1) (Lipman et al., 1970, 2024). From the exposed dip of contacts between eruptive deposits, it is estimated Summer Coon stratovolcano had a maximum radius of approximately 7 km and a minimum edifice height of 2200 m above the basement (Moats, 1990). Intrusive and extrusive deposits indicate three distinct stages of magmatism: an early basaltic-andesite phase, a middle rhyolitic phase, and a late intermediate composition phase (Lipman, 1968; Lipman et al., 2024). The edifice was constructed mainly of basaltic-andesite breccia at the modern level of exposure, though some smaller rhyolitic and dacitic eruptive deposits are still preserved (Harp, 2018; Lipman et al., 2024). Erosion over the past 32 m.y. has exposed hundreds of radial dikes within the volcano oriented about a central intrusive complex (CIC) at the volcanic core, with a modern exposure ~300 m above the base of the volcanic edifice (Fig. 3.1) (Harp, 2021; Lipman, 1968; Lipman, 1976; Mertzman, 1972; Moats, 1990). Of these hundreds of radial dikes, around 19 are distinctive, en echelon segmented large dikes intruded during the middle and late phases of magmatic activity (Lipman, 1968; Poland et al., 2004). Three of the large dikes are middle-phase rhyolite dikes, ranging from 3.5-50 m wide and 1.75-4 km long, while the other ~16 well-exposed intermediate dikes have widths of 1-50 m, with an average of ~15-25 m, and lengths up to 6.5 km (Lipman, 1968; Moats, 1990).

The rhyolite and intermediate composition dikes, referred to as the silicic dikes for the rest of this work, are the focus of this research due to their exposure lengths at different paleodepths under

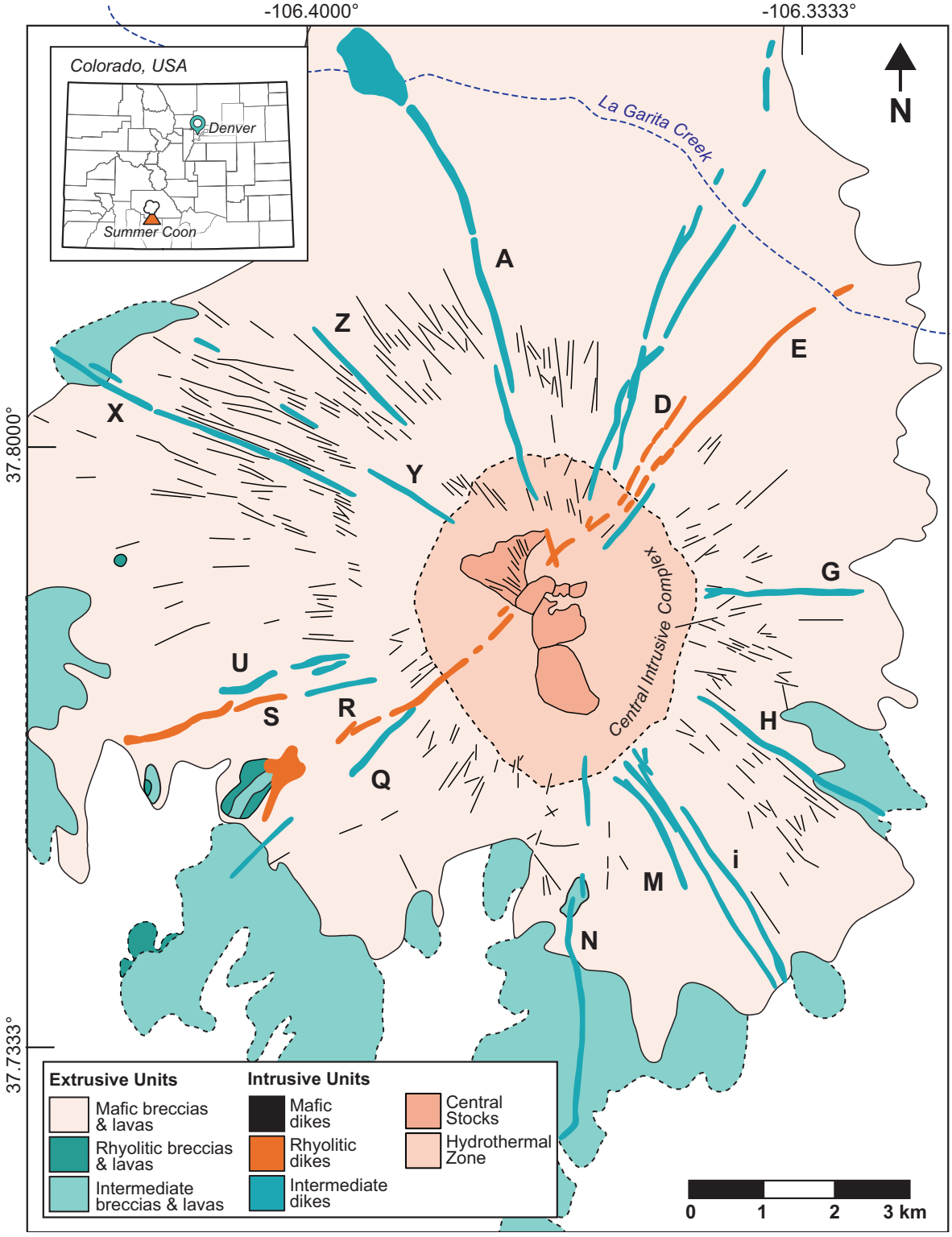

Figure 3.1. Simplified geologic map of Summer Coon volcano, with a portion of the basaltic-andesite dikes marked by small black lines, the intermediate dikes (andesite to rhyodacite) outlined in teal, and rhyolite dikes in orange (thicknesses not to scale). Dikes studied in this work are labeled A through Z, as was convention during fieldwork. Dikes I and M, which are only partially rhyolitic composition, are marked as intermediate per Lipman (1968; 1976). Modified from Harp & Valentine (2018) (after Lipman, 1976).

the edifice, their interpreted lateral intrusion, with some possibly feeding vents on the volcanic flanks, and field and petrologic characteristics indicating water saturated magmas. These characteristics make the silicic dikes at Summer Coon an excellent location to investigate the influence of volatile processes on lateral dike propagation at stratovolcanoes. The km-long outcrop lengths of the silicic dikes is interpreted as evidence of lateral propagation within the edifice, which is supported by both anisotropy of magnetic susceptibility (AMS) and crystal fabric analyses of dike margins (Aksit et al., 2025; Poland et al., 2004). AMS of Dike A and S margins (Fig. 3.1) show dominantly lateral flow in proximal segments, which is interpreted to be due to edifice stresses deflecting the dikes to the flanks (Poland et al., 2004). Crystal flow fabric analysis of the Dike A and S margins and interiors supports the AMS conclusions of primarily low-angle propagation proximally, but found that distally Dike A propagated laterally while Dike S appears to have propagated at a higher angle in the medial and distal segments (Aksit et al., 2025). Along their lengths, the dikes vary in the estimated paleodepths of intrusion, which range from 1.5 km nearest the center of the volcano, and decrease in depth toward the distal flanks to within a few hundred meters of the surface for some dikes, or at the surface for others (Moats, 1990).

The silicic dikes also vary both in composition and crystallinity, roughly distinguished by the magmatic phase of intrusion. Middle-phase rhyolite dikes are extremely crystal-poor, with only several larger crystals visible in thin section, and are dominated by a microlite-rich glass with pockets of pure silica melt. The late-stage dikes vary from andesite to rhyodacite in composition, but consistently have higher crystal contents ranging from 28-35%. The dominant phenocrysts within the intermediate dikes are plagioclase (18-25%), amphiboles (5-16%), and biotite (1-5%), with smaller amounts of pyroxenes and oxides supported by a microlite-rich glass (Mertzman, 1972). The abundance of glass matrix in these samples suggests that although the bulk-rock compositions are intermediate, the melt during intrusion would have been higher in silica, likely rhyolitic (e.g., Bachmann & Bergantz, 2008; Gorbach et al., 2016). The presence of amphibole within these dikes further implies that the melt was saturated, with source conditions of ~3 or more wt.% H_2O (Plank et al., 2013). As the silicic dikes laterally propagated, intrusion at shallower depths could have shifted the solubility of water in magma from ~3.0 wt.% near the center of the volcano, to ~0 wt.% at the flanks (assuming an initial 4.0 wt.% H_2O content at 900°C

and ignoring CO_2; e.g., Liu et al., 2005), resulting in exsolution and bubble growth within a saturated magma. Evidence of this exsolution is preserved as remnant stretched vesicles and vesicle trains in outcrop (Fig. 3.2).

The ubiquity of km-long exposures of the silicic dikes at Summer Coon, along with relatively consistent widths along dike strike (Chaper 2, Tables 2.1, 2.2), suggests vertically stable, lateral propagation within the edifice, at least proximally. Lateral propagation would not be preferred if the dikes were vertically unstable in the subsurface, meaning that either the dike fracture would close and the dikes would arrest in the subsurface, or that the fracture would propagate vertically resulting in vertical magma ascent (Pollard & Townsend, 2018). The stability of the fracture depends on both the external stress field, as well as magma pressure within the dike, which is influenced by magma density and porosity (Abdullin et al., 2024; Maimon et al., 2012; Rubin, 1995). Summer Coon is an ideal natural laboratory to test the role of these twin factors on lateral propagation due to the excellent exposure of multiple, large silicic dikes within the edifice, which both preserve textures of volatile exsolution processes and provide a decompression transect along dike exposures.

3.2.2 Sample Collection

We sampled 15 of the large, silicic dikes at Summer Coon in the summers of 2020-2023 (Fig. 3.1; Appendix Fig. B.1). We chose the selected dikes for analysis for their relatively long outcrop lengths (>1.25 km), and because at exposed depths they do not cross, which could indicate a modified stress field during emplacement due to the proximity of previous intrusions (Rubin, 1995). We conducted a transect along each dike as terrain and public access permitted, sampling the margins at ~200-600 m intervals, and collecting at least one interior sample per dike for comparison. In total, we collected 98 margins and 61 interior samples which are presented in this study. The host rock for all locations where intrusions were sampled was basaltic-andesite breccia (Lipman, 1968; Harp, 2021).

Samples were analyzed for bulk chemical composition, preserved total porosity, and bulk density of the solidified dike material. At least one sample from each dike was sent to Washington State University's Geoanalytical lab for bulk rock geochemistry by X-ray fluorescence spectroscopy (XRF).

We measured porosity for the dikes from 10-50 cm^3 sample cubes cut to avoid fractures, using a 100 cm^3 reference chamber AccuPyc II 1340 Helium Pycnometer. Corresponding powdered samples were analyzed using a 10 cm^3 reference chamber pycnometer, and the results of both solid and powdered runs used to calculate the total preserved porosity (φ) (Formenti & Druitt, 2003; Klug & Cashman, 1994). Because of the diligence taken to avoid fractures, and previous research which shows preserved, and elongated vesicles at micro- to macro-scales (Aksit et al., 2025), we are confident that our porosity measurements reflect the minimum magma vesicularity during emplacement. Additionally, during the transects, we recorded evidence of vesicle bands and stretched vesicles in several of the dikes, which is further evidence of an exsolved volatile phase syn-emplacement (Fig. 3.2).

3.2.3 Vesicularity of Silicic Dikes at Summer Coon

XRF bulk-rock geochemistry for the 15 sampled dikes provides SiO_2 values ranging from 54.8-

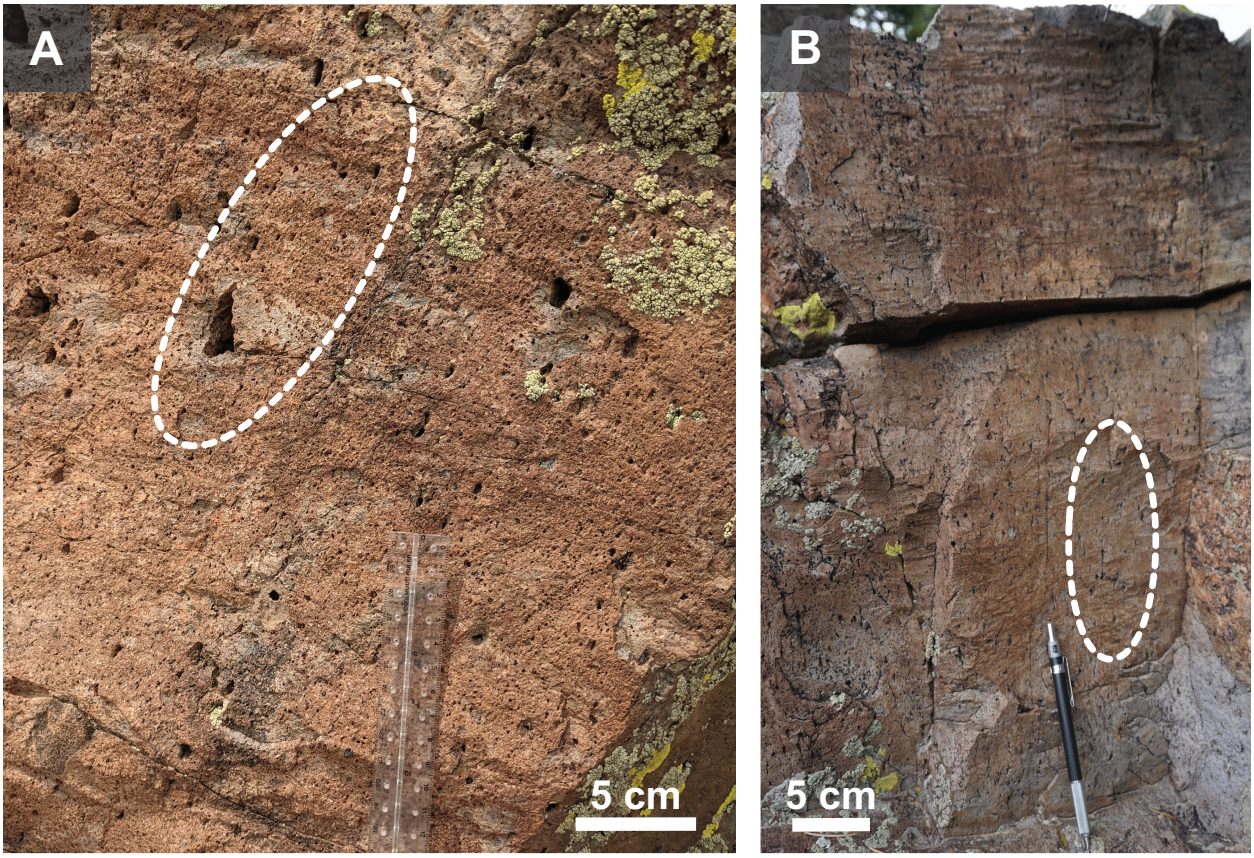

Figure 3.2. Vesicles observed in situ in the field at Dikes G (**A**) and E (**B**). Dashed circles mark smaller, representative areas displaying vesicles for clarity.

74.8 wt.% (Fig. 3.3). Four dikes fall between basaltic trachyandesite, and trachyandesite/andesite to trachyte/dacite compositions (Dikes G, N, U, and Y). Five dikes have compositions between trachyte, trachydacite, and dacite (Dikes A, H, Q, X, Z) and three have variable compositions from trachyte to rhyodacite or rhyolite along their length (Dikes I, M, & S). Of the 15 dikes sampled, three are true rhyolites along their length (Dikes D, E, & R). Margin and interior compositions within a single dike typically vary less than 2 wt.% SiO_2, but where multiple margin samples were analyzed for a dike, the total variation in measured composition exceeded up to 3 wt.% SiO_2 (Appendix Fig. B.2). The dikes fall into two general compositional groups based on geochemistry, trachytes and rhyolites (Fig. 3.3), with the average composition for each of these groups approximated by the average chemistry of Dike A or Dike D. In our model analysis, we use the bulk-rock geochemical data from these two dikes as representative of either the trachytes or rhyolites.

The dikes all have remarkably low porosities in both their margins and interiors (Fig. 3.4A-B). The average porosity per dike, calculated from all margin and interior samples, ranges from 2.0-7.9%

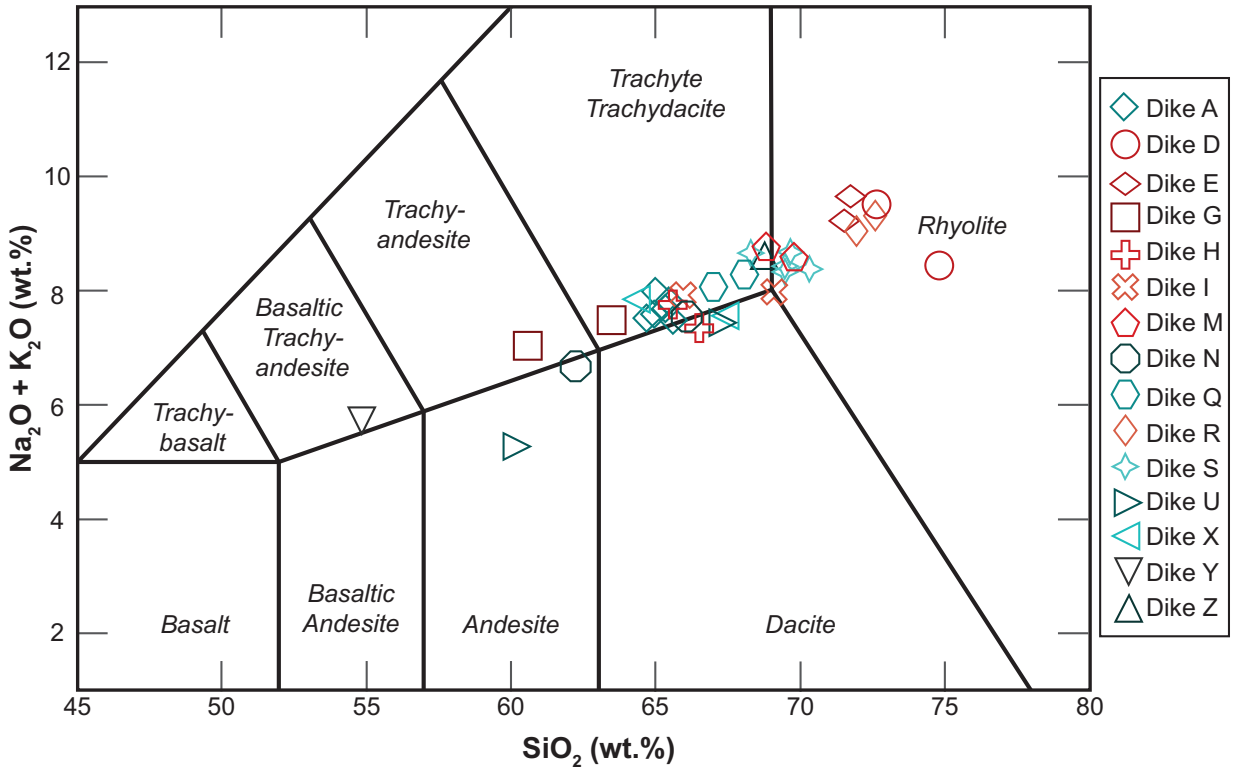

Figure 3.3. Bulk-rock geochemistry for the dikes analyzed in this paper plotted on a Total-Alkali Silicia diagram. Dikes with multiple plotted points were sampled proximally and distally at the margins. An interior sample for Dikes A and S was also analyzed. While Dike Y is geochemically a basaltic-trachyandesite, its width and porosity are similar to the higher silica dikes analyzed in this study, and is thus grouped with the silicic dikes.

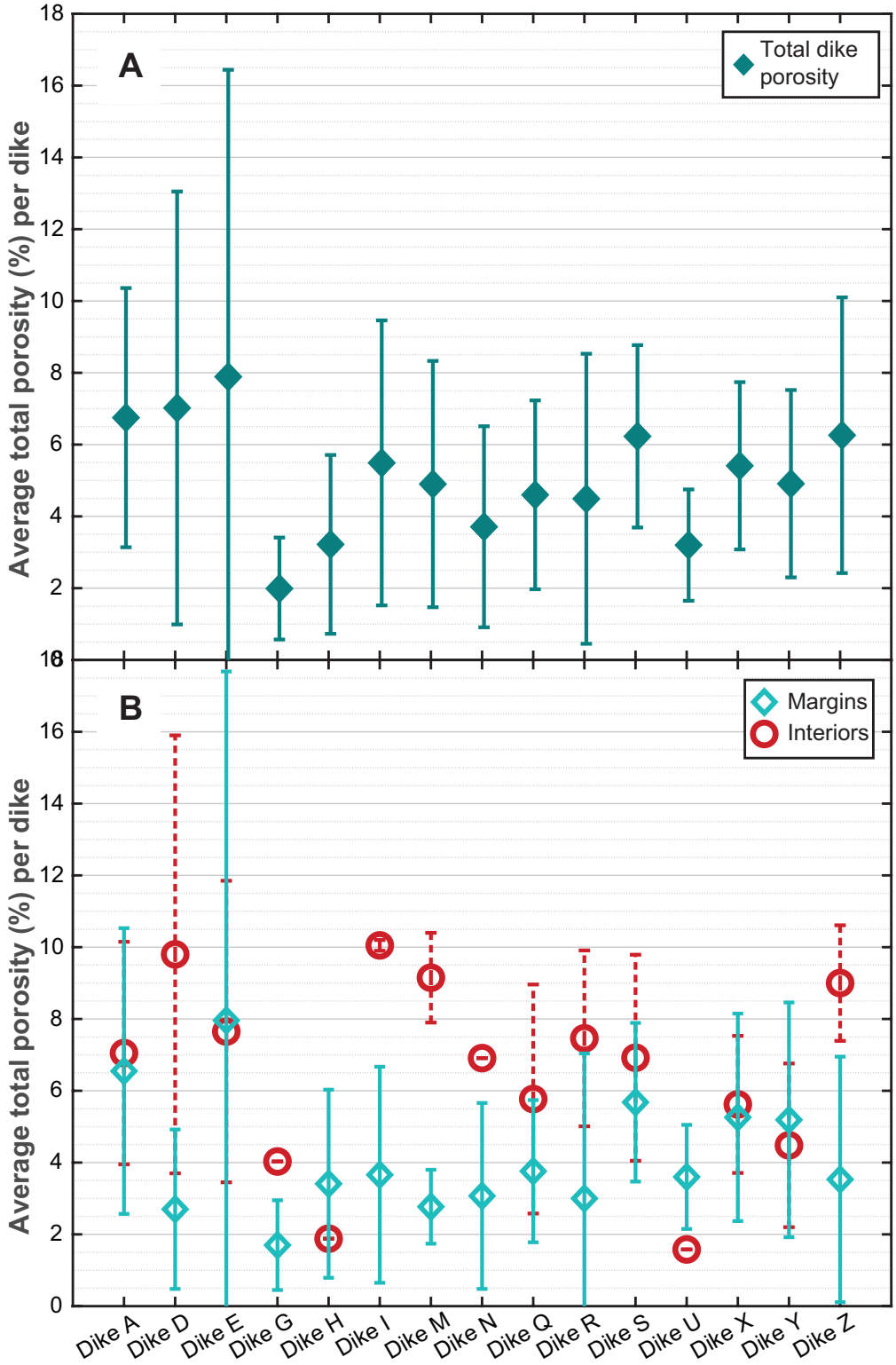

Figure 3.4. Total porosity measurements for each dike. **(A)** shows the average porosity of each dike, compiled from both interior and margin samples, with the solid diamond marking the average value, and error bars indicating the standard deviation. **(B)** divides the porosity measurements into the average margin porosity (teal diamonds) and average interior porosity (red circles). As Dikes G, H, N, and U only had one interior sample analyzed, there are no error bars included.

(Fig. 3.4A). Fourteen out of fifteen analyzed dikes have average margin porosities that fall below 11%, and the average margin porosity across all dikes is 4.1 ± 1.6% (Fig. 3.4B). Only a single margin sample collected from Summer Coon exceeds the average porosity measured for all of the dikes. A Dike E proximal margin sample approaches ~30% porosity and pushes Dike E's average up to 17.5% porosity (Fig. 3.5A-B); however, the remaining Dike E margins are all below 7% porosity. Interior samples from across the silicic dikes have similarly low porosities as the margins, averaging 6.5 ± 2.6%. For five of the dikes however, only one interior sample was analyzed. Yet even when looking exclusively at the dikes with multiple interior samples, which have an average interior porosity of 7.3 ± 1.7%, the average interior porosity overlaps with that of the dikes with only one sample. On average, porosity is higher in the interiors than the margins, with 11 dikes having higher interior porosities than in the margins, and four dikes having lower porosity in the interiors (Fig. 3.4B). The difference in values between margin and interior porosity ranges from 0.3% to 7.1% for each dike, but there is no consistent variation from location to location within a dike between the margins and interior porosity (Fig. 3.5A-B).

In order to assess whether topography-induced pressure gradients influenced volatile exsolution and bubble growth, we compared changes in margin porosity along the lengths of the dikes. Changes along dike length are considered both as a function of distance from the center of the volcano (Fig. 3.5A-B) and the normalized dike length (Fig. 3.5C-D). Despite large differences in paleodepth between the most proximal and distal samples, there is no systematic variation in margin porosity along the dike lengths, whether evaluated as a function of dike length, distance from the volcano center, or composition (Fig. 3.5). The full range of measured porosities (0-10%) is usually expressed at each location along the dikes. There are also no discernible trends in whether margin porosity is higher or lower at the most proximal or distal positions along dike length. Overall, the dikes have very low margin porosities along their lengths, with no correlation between position along the dike and measured values.

Our analysis shows that the dikes of Summer Coon have consistently low porosities, never exceeding ~11% (except for one anomalous sample from Dike E). Low porosity characterizes both the margins, where high shear may promote outgassing into the host rock, and the interiors, where shear stresses are lower. Overall, the silicic dikes at Summer Coon are remarkably uniform in porosity,

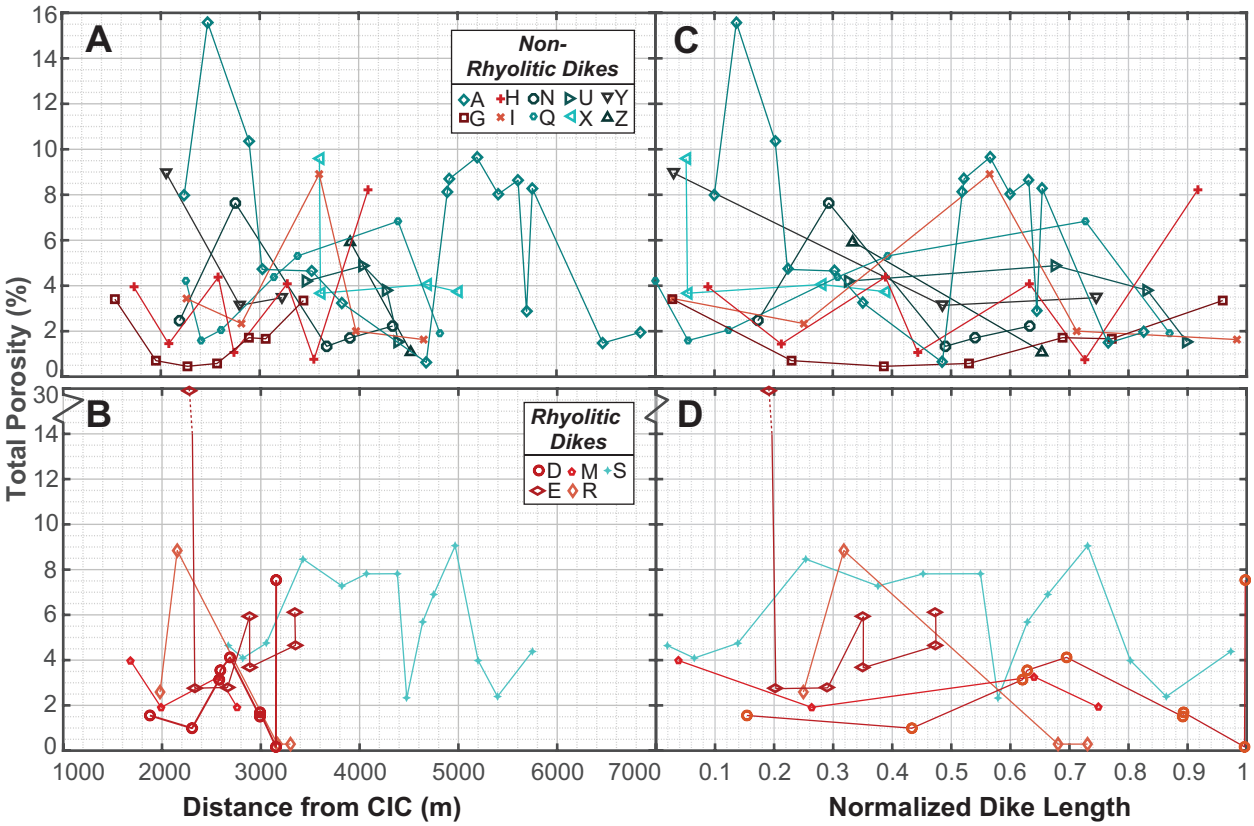

Figure 3.5. Sample margin porosity measurements over the length of each of the dikes. Dikes were divided by composition into non-rhyolitic and rhyolitic composition based on trends observed on the TAS (symbols correspond to Fig. 3.2). Total porosity is plotted as a function of distance from the central axis of the volcano (CIC) in panels **A** and **B**. In panels **C** and **D**, porosity is plotted over the normalized exposed length of each dike. In each panel, numbers to the right are increasing distance from the volcanic center (i.e.: more distal). Rhyolitic composition plots **B** and **D** feature a break in porosity between 15 to 30% to accurately show the measured high porosity of the most proximal sample of Dike E.

regardless of composition, dike length, or distance from the center of the volcano. Considering their exposure within the edifice and inferred paleodepths ranging from ~1500 m to near surface (Moats, 1990), solubility laws predict higher vesicularities if the magmas were hydrous and evolved under closed-system conditions (Liu et al., 2005). The observed low porosities therefore imply that the dikes have outgassed, likely facilitated by some combination of high shear and volatile migration through permeable pathways. In the following section, we test whether and how the processes of volatile exsolution and outgassing may have influenced the trajectories, ascent heights, and final arrest depths of these dominantly lateral propagating silicic dikes at Summer Coon.

3.3 MODELING THE DEPTH AND HEIGHT OF LATERAL DIKES

3.3.1 Model Set-Up

To explore how volatile exsolution and outgassing influence the geometry and intrusion depth of laterally propagating dikes at stratovolcanoes, we developed a coupled mechanical and thermodynamic modeling framework. Our goal is to evaluate how magma density changes associated with exsolution, combined with edifice-induced stresses, control the height and depth of lateral dikes as they propagate outward beneath a volcanic cone.

We treat the dike as a vertical, two-dimensional elastic crack subjected to external stresses and an internal pressure distribution. The crack mechanics are solved using an elastic fracture model that permits variable distributions of normal traction along the fracture walls, in order to capture potentially non-linear magma pressure and external stress distributions related to volatile exsolution and volcanic topography (Pollard & Townsend, 2018). To simulate a laterally propagating dike, we assume that neither the upper nor lower dike tips advance or close; specifically, we restrict our attention to cases where the stress intensity factor, K, at the upper and lower tips is zero ($K = 0$). This simplifying assumption reduces the number of possible dike configurations, but captures the conditions under which a dike may maintain a nearly constant vertical extent while propagating laterally. At each radial distance from the volcano center, we search for combinations of dike depth and height that satisfy this vertical stability criterion.

Boundary conditions include three principal contributions to the normal tractions acting on the dike. First, internal magma pressure reflects the weight of the magma column and incorporates depth-dependent changes in magma density driven by volatile exsolution. Second, a constant overpressure term accounts for pressurization from the source reservoir. Third, the external stress field includes lithostatic pressure modified by the perturbation imposed by the volcanic edifice. We calculate vertically stable dike geometries by performing a grid search over depth and height, computing stress intensity factors at the top and bottom of the fracture, and identifying the depth-height pairs that bring both values closest to zero. In this way, we track how stable dike dimensions vary with distance from the volcano center.

The external stress field is derived from a finite-element model of stresses beneath and within

an idealized Summer Coon-like stratovolcano (Fig. 3.6) (Scholz, 2025). We generated an edifice shape by fitting double Gaussian functions to the profiles of modern arc stratocones, constrained such that the basal cone slope is ~17°, in line with field data (Moats, 1990). The resulting cone has a total relief of ~2600 m, larger than previous constant-slope estimates but consistent with the presence of a slope break. We treat the rock-air interface as a traction-free boundary, apply roller conditions at the far field boundaries, and assume a Poisson's ratio of 0.35.

Magma density is modeled as a two-phase mixture of melt and an exsolved volatile phase, following

Eq. 1
$$\rho_{\mathrm{magma}} = \rho_{\mathrm{melt}} (1 - \varphi) + \rho_{\mathrm{gas}} \varphi$$

where ρ_{melt} is the melt density, ρ_{gas} is the gas density, and ϕ is the gas volume fraction. We compute melt density using the DensityX model of Iacovino & Till (2019), which accounts for the effects of pressure, temperature, and composition. To study the effects of melt chemistry on lateral dike geometry, we test two compositions based on the bulk chemistry of rocks sampled from two dikes at Summer Coon (Appendix Table B.1; one trachyte dike (Dike A) and the other a rhyolite dike (Dike D). These two dikes best approximate the compositional averages we found delimiting the non-rhyolitic (trachytic) from the rhyolitic dikes. For simplicity we use a constant temperature of 800° C. Gas density is calculated from the ideal gas law, acceptable for the low pressures characteristic of shallow (< few km) crustal dikes. The exsolved volatile fraction is determined using the solubility model of Liu et al. (2005) for water in rhyolite. Because density and magma pressure are coupled, we iterate between solving for volatile exsolution and adjusting the magma pressure distribution until the system converges. We found that solutions were unstable when porosity exceeds 50%, and therefore imposed an upper limit of 50%. This value is far greater than expected natural for porosities, since outgassing or fragmentation would likely occur before reaching such levels. In addition, field observations from Summer Coon dikes reveal porosities far lower than expected for such shallow intrusion depths, consistent with outgassing beginning at ~12-15%. To capture this effect, we run a suite of models with a 15% porosity cap to test how volatile loss influences dike stability.

To establish the impact of including volatile exsolution on stable dike propagation, we first

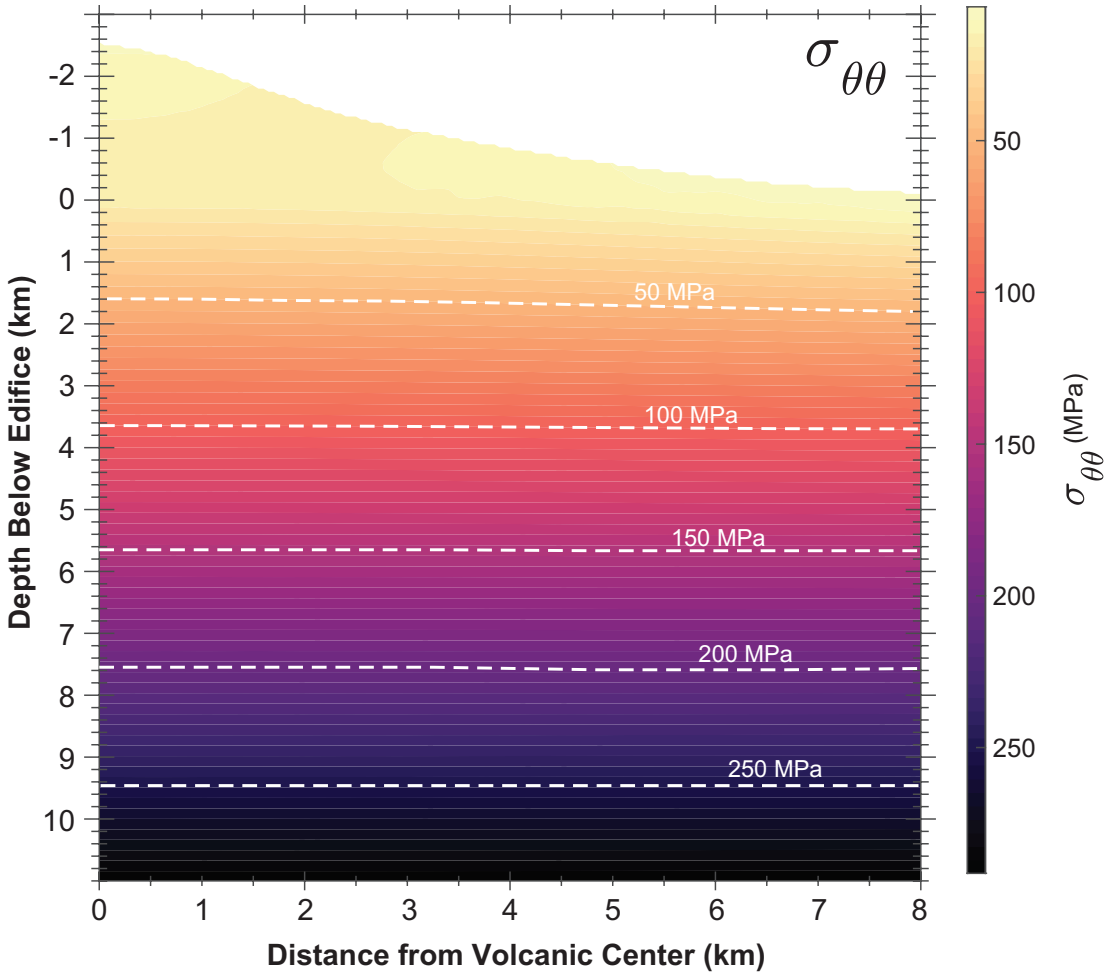

Figure 3.6. Modeled stresses in the theta-theta direction, as would act on dike opening, due to combined lithostatic and edifice stresses, where compression is positive. Dashed lines mark isobaric isopleths every 50 MPa beneath the edifice. Stresses within the edifice are both low with very low gradients. Modified from Scholz (2025).

modeled trachytic and rhyolitic compositions with an initial water content of 0 wt.%. This control run assumes no volatile exsolution during propagation, so that magma density is only a function of pressure, effectively uniform. This base line is similar to the conditions assumed for most current models of magma transport (e.g., Rivalta et al., 2015; Taisne & Tait, 2009). We model the vertically stable height and depth for three different possible overpressures (2, 4, and 6 MPa), which represent the magma pressure in excess of the external confining stress, evaluated at the dike center. After establishing our baseline expectations in the no exsolution case, we move on to considering volatile exsolution for trachytic and rhyolitic compositions with a total water content of 4 wt.%, and capping porosity at either 50% or 15%.

3.3.2 Model Results

3.3.2.1 No exsolution

For dry magmas and no exsolution, modeled trachyte dikes are only predicted to be vertically stable (and thus laterally propagating) for overpressures of 2 and 4 MPa (Fig. 3.7A). The dike heights range from 7 km for 2 MPa up to 10.7 km for 4 MPa, and are vertically stable for radial distances up to 4.2 km (4 MPa) to 6.2 km (2 MPa) from the volcanic center (Fig. 3.7A). While the top of the dike with 4 MPa overpressure is stable in the edifice at a height of 400 -580 m above the basement, the dike with only 2 MPa overpressure is not predicted to be stable within the edifice until a radial distance of 3.8 km, and then only reaches a height of 320 m above the basement. In contrast, the rhyolitic dikes are vertically stable at all three overpressure conditions in the absence of exsolution (Fig. 3.7B). These dikes are shorter than the trachytic case, from 5.2 km (2 MPa), 7.2km (4 MPa), up to 9.4 km (6 MPa), which is consistent with the lower density of rhyolite (here ranges from 2365-2410 kg/m^3) compared to trachyte (here 2490-2535 kg/m^3) and the expected relationship between the "closure height" of a fluid-filled fracture and the fluid-rock density contrast (Fig. 3.8) (Pollard & Townsend, 2018; Secor & Pollard, 1975). The rhyolites can be vertically stable to approximately the same radial distances as the trachytes (2 MPa: 5.8 km, 4 MPa: 4.7 km, 6 MPa: 2.5 km). The model rhyolitic dikes are all stable within the edifice from heights of 100-900 m above the basement over their entire lengths. In both the trachytic and rhyolitic runs, the stable dike heights become shorter with distance from the center of the volcano, with the stable bottoms decreasing in depth across all three overpressures, and the stable dike tops for 2 and 4 MPa increasing with increasing radial distance.

3.3.2.2 Volatile Exsolution for Capped 50% Porosity

When we cap the maximum porosity at 50%, we find vertically stable configurations for the model trachytic dikes at all overpressures, including the case of 6 MPa that was not predicted to have any stable configurations when volatile exsolution was neglected. The stable configurations include dike tops reaching ~40-1500 m above the basement (Fig. 3.7C). The dikes are significantly shorter compared to the dry cases, at 0.85-4.2 km high, with relatively uniform heights from proximal to distal locations.

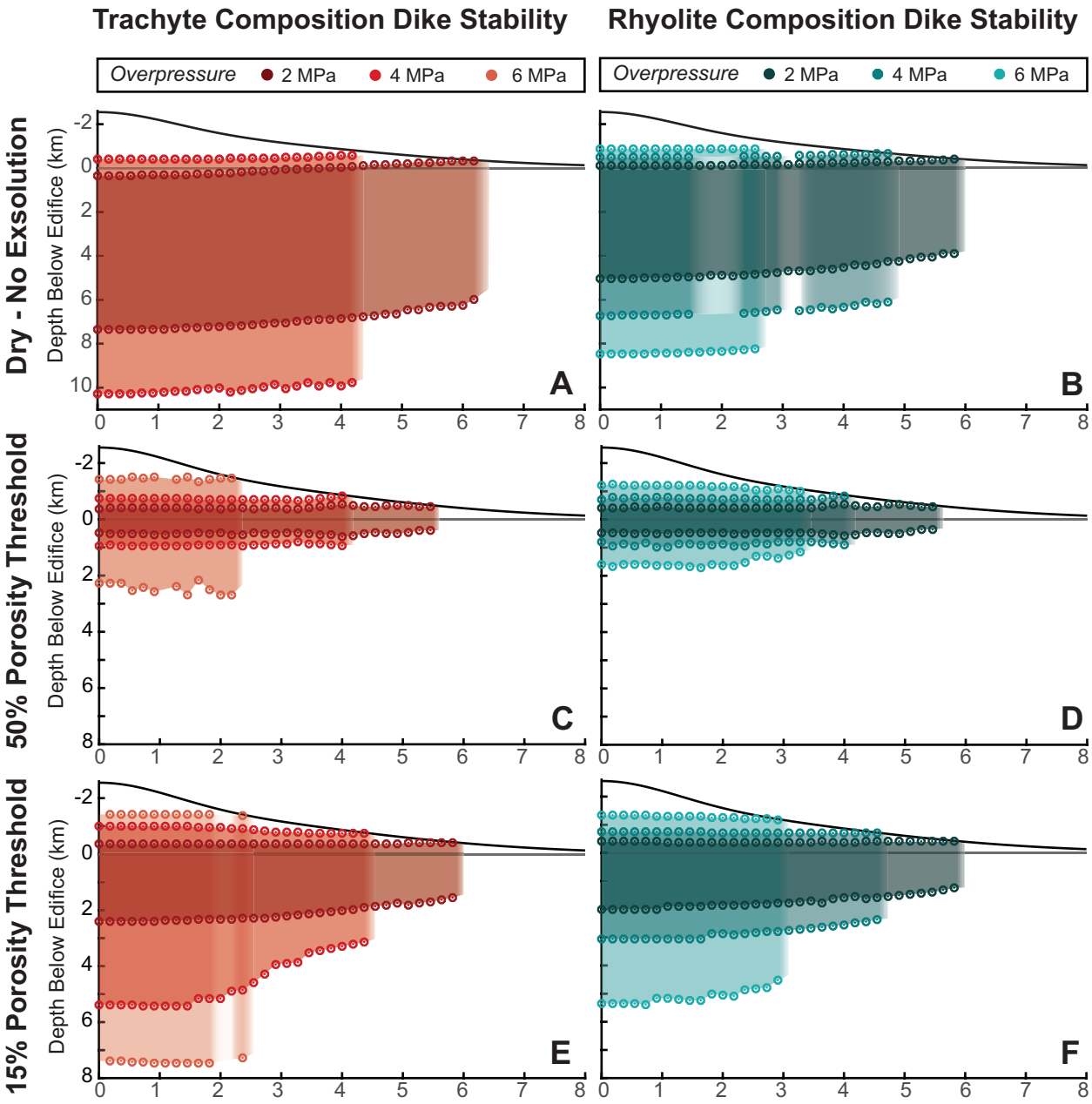

Figure 3.7. Stable dike outputs for the modeled scenarios of no exsolution (**A** and **B**), 50% porosity threshold (**C** and **D**), and 15% porosity threshold (**E** and **F**). The modeled location of stable dike top and bottoms where the stress intensity factor (*K*) was less than 25 MPa $m^{½}$ are marked by circles. Trachyte compositions are shown on the left in red, and rhyolitic compositions in teal on the right. Differences in overpressure are denoted by different shades, with 2 MPa runs being the darkest shade, 4 MPa runs being the intermediate shade, and 6 MPa runs being the lightest shade. Gaps in stability from the model are shown by gaps in circles, and the filled dike interiors grading to white.

0 wt.% H_2O - No Exsolution

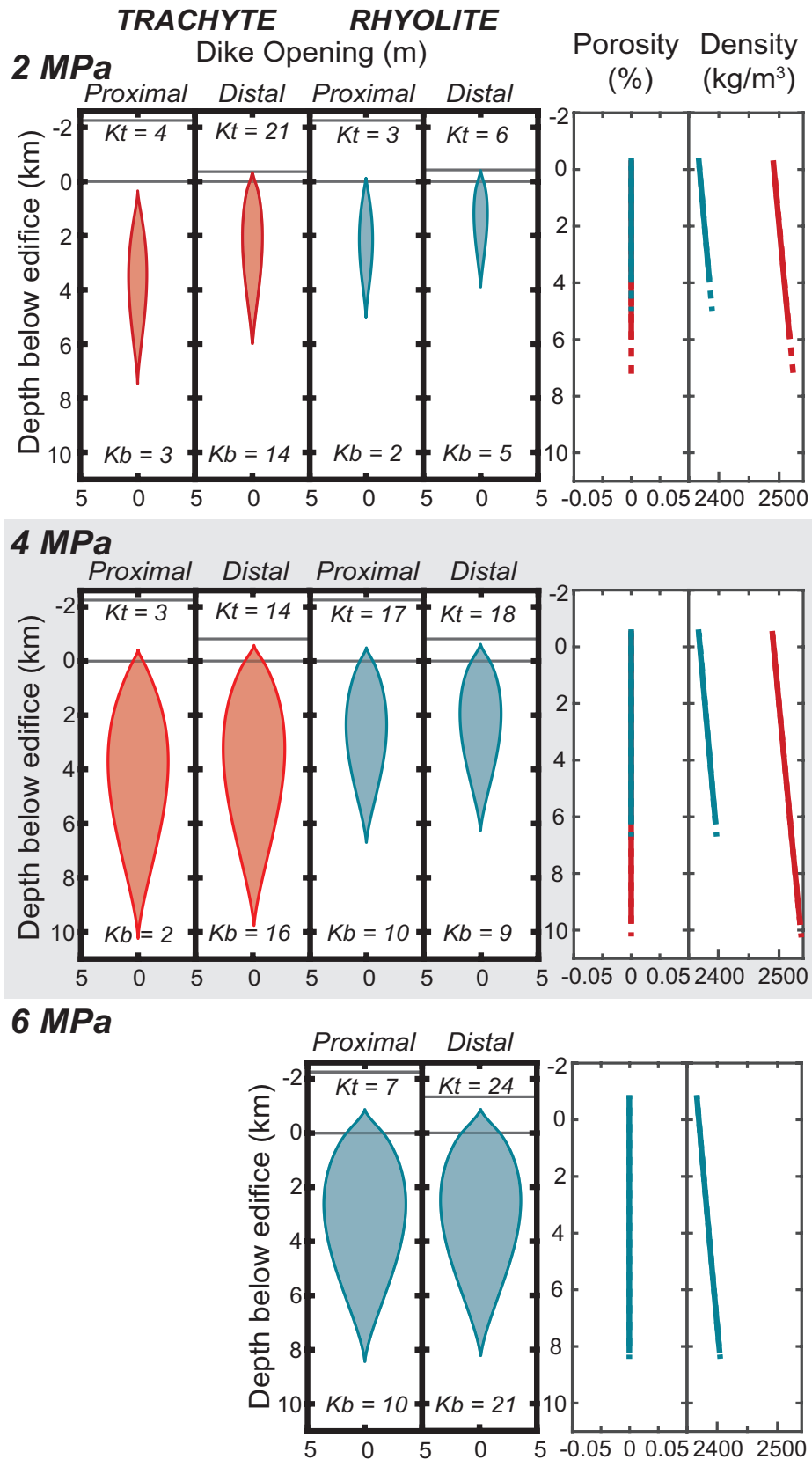

Figure 3.8. ***(Previous Page)*** Modeled dike opening for both trachytic and rhyolitic compositions for the no exsolution scenario for a dry magma, with the calculated stress intensity at the top (Kt) and bottom (Kb) of the dike marked. The left panel of each composition shows the most proximal opening (fixed at 0.9 km from the volcanic center), while the right panel shows the most distal, stable opening profile (trachytic: 6.2 km for 2 MPa, and 4.2 km for 4 MPa; rhyolitic: 5.8 km for 2 MPa, 4.2 km for 4 MPa, and 2.5 km for 6 MPa). Porosity and density profiles for each composition both proximally and distally are plotted in the far right panel. Red lines denote the trachytic compositions, and teal the rhyolitic compositions, with dashed lines marking the proximal profiles and solid lines the distal profile. Since there are no volatiles to exsolve, porosity stays fixed at 0%. Density varies for the dikes as a function of the initial composition, with the rhyolites being ~100 kg/m^3 less dense. Though there are no porosity related variations in density, there are pressure-induced variations causing density at the bottom of the dike to be higher than that at the top of the dike. Since the model did not find any stable configuration for the trachytic composition at 6 MPa overpressure in the no exsolution case, no plot is provided.

The shorter dike heights are consistent with the drastically lower densities for the dikes due to the high bubble fraction (trachyte: 1230-2100 kg/m^3 and 10-50% porosity, rhyolite: 1170-1750 kg/m^3 and 25-50% porosity). The radial distances over which dikes can be vertically stable are approximately the same as the no exsolution scenario (~2.2-5.5 km), before the dike tops would intersect the edifice surface.

The model rhyolitic dikes also all have vertically stable configurations within the edifice and, like the trachytic dikes, are stable higher into the edifice (410-1210 m above the basement) compared to the case with no volatile exsolution (Fig. 3.7D). The stable heights of the rhyolitic dikes are significantly shorter than the trachytic dikes and all of the cases without exsolution, at 0.8-2.8 km tall. This variability is also seen in dike lengths, where the 2 and 4 MPa dikes are shorter in length than the dry equivalents (4.0-5.5 km), while the 6 MPa scenario is stable to a radial distance of 800 m more than the no exsolution counterpart.

3.3.2.3 Volatile Exsolution for Capped 15% Porosity

In the third scenario, we simulate the effects of volatile outgassing by capping magma porosity at 15%, a value consistent with the upper limits determined from samples gathered in the field. In this scenario, model trachytic dikes are predicted to have vertically stable configurations within the edifice at a height of ~370-1430 m above the basement (Fig. 3.7E). The dikes are much taller than the 50% porosity runs, but shorter than the dry scenario, ranging in maximum height from 2.8-8.8 km. This is consistent with magma densities that fall between the no exsolution and 50% porosity models (trachyte: 2025-2350 kg/m^3, rhyolite: 1940-2250 kg/m^3) (Fig. 3.9). The dikes change variably in stable height

along their lengths (6 MPa: 100 m, 4 MPa: 2500 m, 2 MPa: 800 m; Fig. 3.7E). The 4 MPa case is the only one with a drastic change in the depth of the dike bottom, likely as a result of the dike bottom crossing a solubility threshold below which no exsolution would occur (Fig. 3.7E; Fig. 3.9).

Like the trachytic dikes with a 15% porosity cap, the rhyolitic dikes are all stable into the edifice (410-1340 m), but at slightly lower elevations than the trachytes (Fig. 3.7F). The dikes with a 15% porosity cap are also taller (2.5-6.7 km) than the dikes with a 50% porosity cap, and shorter than the dry dikes of same composition. The 4 and 6 MPa scenarios are considerably shorter, by 2.6 and 2.4 km respectively, than their trachytic counterparts. The stable top elevations vary minimally for the 2 and 4 MPa cases, but decrease by 140 m distally for the 6 MPa run. In contrast, the stable bottom depth decreases considerably with distance from the volcano center, and these stable depths are much deeper than the 50% porosity model, but shallower than the no exsolution model. They are also stable at shallower depths than was modeled for the trachytic compositions at 15% porosity. The dike lengths vary inconsistently from the 50% porosity scenario. The 2 and 4 MPa dikes are longer (5.8 and 4.5 km), but the 6 MPa dike is shorter by 400 m. The 6 MPa dike is stable higher in the edifice than its 50% porosity equivalent, and intersects the surface before it can propagate to the same radial distance. Unlike the 6 MPa trachytic dike in the outgassing scenario, the 6 MPa rhyolitic dike is stable along its entire length.

3.3.2.4 Summary of Key Model Trends

Several trends can be distilled from the multiple runs of our model based on overpressure, porosity, and composition. In all scenarios, higher overpressures produce taller dikes that are able to reach higher elevations within the edifice. The higher overpressure dikes are also shorter in length than the lower overpressure cases because the dikes would intersect the surface at smaller radial distances along their path. Lower overpressure dikes, because they do not propagate as high into the edifice, are stable out to greater distances from the volcanic center. Models considering volatile exsolution produce much shorter dikes than in the no exsolution scenario, with the 50% porosity models producing the shortest dikes while the 15% porosity models produce dikes of intermediate

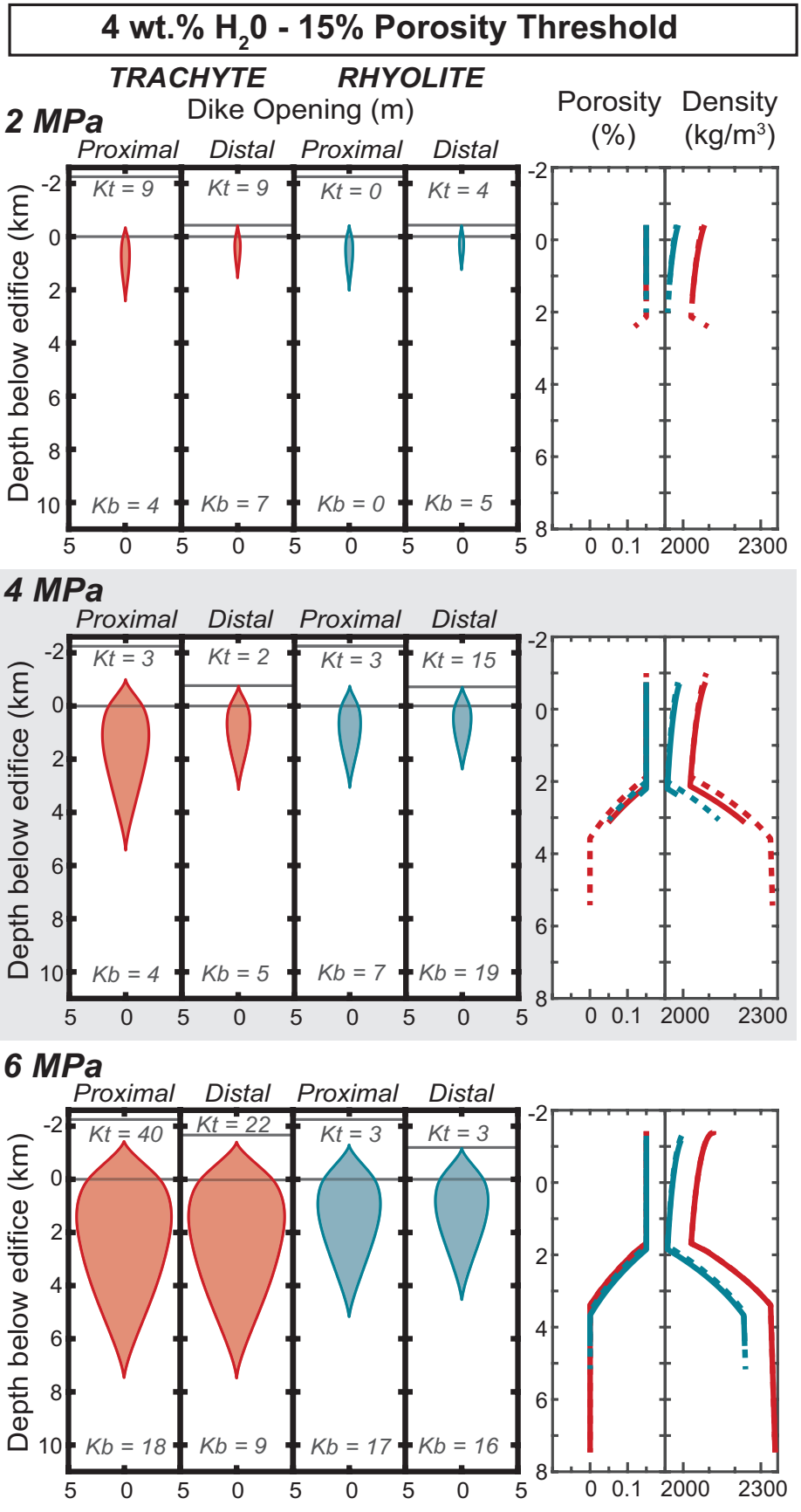
4 wt.% H20 - 15% Porosity Threshold
TRACHYTE
RHYOLITE
Dike Opening (m)
Porosity (%)
Density (kg/m3)
2 MPa
Proximal
Distal
Proximal
Distal
Depth below edifice (km)
Kt = 9
Kt = 9
Kt = 0
Kt = 4
Kb = 4
Kb = 7
Kb = 0
Kb = 5
4 MPa
Kt = 3
Kt = 2
Kt = 3
Kt = 15
Kb = 4
Kb = 5
Kb = 7
Kb = 19
6 MPa
Kt = 40
Kt = 22
Kt = 3
Kt = 3
Kb = 18
Kb = 9
Kb = 17
Kb = 16

Figure 3.9. ***(Previous Page)*** Dike opening, porosity, and density profiles for both trachytic and rhyolitic magmas containing initially 4 wt.% H_2O, and porosity capped by a percolation threshold of 15%. Taller dikes start with 0% porosity, but begin degassing at ~3.5 km depth until the 15% porosity threshold is reached at ~2.25 km depth, and above this depth porosity remains constant. These variations are reflected by changes in density, where the magma is higher density at depth, and proportionally decreases as exsolution occurs. Once the percolation threshold is reached, the magma slightly increases in density with decreasing depth as volatiles escape the system.

heights. The 50% porosity model dikes also have relatively stable heights along their length, while the 15% porosity model dikes vary in height by 720 m or more along their lengths (Fig. 3.7). Composition is also a significant factor in dike heights and stable propagation lengths. The 50% porosity and outgassed trachytic compositions are much taller than their rhyolitic counterparts, and as such, stable to higher elevations within the edifice, which results in generally shorter dike lengths because they intersect the surface at smaller radial distances.

3.4 DISCUSSION

3.4.1 Porosity, Outgassing & a Percolation Threshold

The silicic dikes at Summer Coon have extremely low porosities for intrusions emplaced at depths ranging from 1.2 km to near the paleosurface. When we consider volatile exsolution in our stability model, the dikes reach the 50% porosity limit we enforce at up to 500 m below the base of the edifice, resulting in magma densities as low as 1170 kg/m³ (Appendix Fig. B.2). Without the 50% porosity constraint, the dikes would be entirely unstable in the subsurface. This could produce a gas cap dike where the exsolved gasses and magmatic fluid are decoupled, with the gases propagating or escaping ahead of the magma (Maimon et al., 2012). If there were sufficient permeable pathways for gas to travel through and leave the dike in a gas cap, the remaining magma would be highly degassed. However, field exposures and thin sections from across Summer Coon show evidence of some syn-emplacement, coupled gas and fluid preserved as vesicle bands or elongated isolated vesicles (Fig. 3.2).

An alternate explanation for the low porosities measured is that the magma reached a percolation threshold (φ_C), or critical porosity at which the magma is permeable, allowing gases to travel through and escape the magma. The percolation threshold is regulated by the crystal content of the magma, with high crystal content aiding in magma outgassing, even in the deeper reservoir (Colombier

et al., 2020; Parmigiani et al., 2017). Image analysis of thin sections from Dikes A and S at Summer Coon show an average of 30% crystal area fraction along the dike, indicating they were derived from relatively crystal-rich magmas. Samples from the non-rhyolitic dikes also show similar crystal contents. To determine if this range of crystallinity promotes outgassing and could account for the low porosities measured, we estimate the percolation threshold at which degassing pathways would form under the non-rhyolitic magmatic conditions. We utilize the Parmigiani et al. (2017) model to calculate a percolation threshold (φ_C) since it is calibrated for crystal-rich magmas, assuming an average of 30% crystallinity (ε_x) for the dikes:

Eq. 2
$$\varphi_c = 2.75\varepsilon_x^3 - 2.79\varepsilon_x^2 + 0.6345\varepsilon_x + 0.997$$

This model is calibrated for a static magma at 100-250 MPa, which is at a higher pressure than anticipated at the depth of intrusion for the dikes at Summer Coon (Parmigiani et al., 2017), but we expect minimal pressure influence compared to the influence of shear on reducing the percolation threshold (e.g., Caricchi et al., 2011). We find a percolation threshold of 11% for these dikes, so that sufficient connectivity only requires minimal porosity to promote outgassing. Our measured average porosities, both margin and interior, all fall below this theoretical threshold (Fig. 3.4A-B).

The percolation threshold we calculated for crystal-rich magmas is not appropriate for three of the rhyolite dikes (D, E and R), which are extremely crystal-poor. Experimentation on crystal-free, rhyolitic melts suggest that the percolation threshold may reach as high as 50-90% porosity (Giachetti et al., 2019; Lindoo et al., 2016). The low porosities observed in these dikes, and in the non-rhyolitic dikes, may be modulated by a different process. High shear, especially within a highly viscous fluid, promotes bubble coalescence, and creates pathways for gas to escape both at the conduit margins as well as through the magma (Caricchi et al., 2011; Okumura et al., 2010, 2013). Shear coalescence thus promotes outgassing at much lower porosities than the theoretical percolation threshold in a static state (Caricchi et al., 2011). Dikes of every composition at Summer Coon show evidence of high shear in both the margins and interiors through strong flow fabrics (Aksit et al., 2025; Harp & Valentine, 2018; Poland et al., 2004), and in the crystal-poor rhyolites through prevalent flow-banding. We posit that high shear, combined with a lower percolation threshold for crystal-rich magmas, promoted the

low porosities observed at Summer Coon. Our model of dike stability that caps porosity at 15% is the best to capture this proposed dynamic exsolution and volatile loss through shear-induced permeable networks.

3.4.2 Edifice Stresses and Degassing Promote Lateral Propagation

We utilize a topographically-controlled stress distribution model to determine propagation stability under a probable Summer Coon-sized edifice (Moats, 1990; Scholz, 2025). To test the conditions under which dikes would stably, laterally propagate, we assumed they would be trapped vertically, so that the dikes are not opening or closing along the dike top ($Kt \approx 0$), (Pollard & Townsend, 2017). Our edifice stress model produces low gradients in confining stress in the theta-theta direction across a continuum from the basement to the edifice (Fig. 3.6). The low stress gradients in the edifice effectively trap the dikes within the volcano by promoting the closure of the upper tips, thus driving lateral propagation. These results are contrary to the long-standing paradigm that the stress perturbation of the edifice itself acts as a barrier for propagation (Pinel & Jaupart, 2000, 2004). According to this paradigm, if the magma is capable of making it into the edifice, it must necessarily ascend buoyantly and erupt, having overcome the maximum stress barrier to propagation (Pinel & Jaupart 2000). This runs counter to the plethora of natural examples where propagation occurred in edifice, but the dikes are interpreted to have arrested without eruption, including Summer Coon as well as Spanish Peaks CO, and Sunlight Volcano WY (Feeley & Cosca, 2003; Roman & Jaupart, 2014). Our model shows that if magma can get into the edifice, the low stress gradient of the volcano itself can trap magma and encourage intra-edifice lateral transport.

Previous modeling has demonstrated the difficulty of getting seemingly buoyant magma to propagate into an edifice (Pinel & Jaupart, 2004; Scholz, 2025). In our run of dry magmas without exsolution, despite the magmas having lower densities than the host rock, the dikes are trapped beneath the edifice at lower overpressures proximally (Fig. 3.7A-B). Only with higher overpressures are the dikes able to ascend into the edifice, but they are still stable to lower elevations within the volcano than when incorporating exsolution (Fig. 3.7). The rhyolites are stable to slightly higher elevations than the

trachytes since their base density is lower than the trachtyes (Fig. 3.7A-B). Dikes are able to overcome the edifice stresses, intrude into, and remain stable within the edifice at all overpressures when volatile exsolution and outgassing are considered. This is likely due to the larger gradient in pressure-dependent density due to the inclusion of bubbles (50% porosity- trachytes: 1230-2100 kg/m^3, rhyolites: 1170-1750 kg/m^3; 15% porosity- trachytes: 2025-2350 kg/m^3, rhyolites: 1940-2250 kg/m^3). If only considering the 15% porosity model, which is constrained by measurements from Summer Coon, the dikes are stable at the level of exposure at the observed distances from the volcanic axis, even at lower overpressures.

Our work demonstrates that lateral propagation in a volcanic edifice is encouraged both by stresses due to volcanic topography and by degassing. The volcanic edifice produces low gradients in stress, which traps buoyant magmas undergoing dynamic density changes due to volatile exsolution and outgassing during transport. This results in the stable, intra-edifice, lateral propagation of dikes that may arrest in the volcano, especially if overpressures remain low.

3.4.3 Inferred Volumes of Intrusion

An ongoing problem in modeling volcanic processes is estimating the volume of magmatic products, whether to gauge the size of eruption or to better understand magma reservoirs (e.g., Caricchi et al., 2016; Karakas et al., 2017). Field data from Summer Coon produces good constraints on lengths as well as width changes of the silicic dikes at the level of exposure (~300 m above the volcano base), but we are missing the third dimension in the field that is necessary to compute probable volumes for the dikes. Our field-informed model produces a range of stable dike heights under an edifice for an initial magmatic overpressure of 2-6 MPa, and can be combined with field measurements to calculate a range of volumes for intrusion.

Here we calculate the maximum magmatic volumes required for emplacement based off observations of Dike A, the longest trachytic composition dike exposed at Summer Coon, with widths calculated from field and Google Earth measurements. We also calculate the minimum volume required to emplace a dike utilizing data from the smallest of the rhyolitic dikes, Dike D, for which

high resolution widths were mapped in the field. For an average width of 33 m from Dike A, and using the modeled stable height and length estimates in the case of dry magma with no exsolution, emplacement would require 1.36 to 1.46 km^3. However, if the outgassing model is considered with a percolation threshold of 15%, only 0.46 to 0.75 km^3 of magma would be required to emplace a dike at the geometry observed at the level of exposure. Outgassed magma would only necessitate 34-51% of the volume of magma as the no exsolution scenario for similar field exposures. This reduction in volume of emplacement between no exsolution and the degassing scenarios is also clear when applied to the small rhyolite data. Dike D, with an average width of 4.7 m, and using the stable heights and lengths calculated from the rhyolite model, would need 0.12 to 0.15 km^3 of magma for emplacement in the no exsolution case. When taking into account outgassing, this drops to 0.06 to 0.08 km3, or only 44-78% of the magma volume required for intrusion in the no exsolution.

These volume estimates demonstrate both the importance of considering exsolution in modeling dike emplacement, as well as the variation in volume estimates based off the unknown quantity of dike height. Exsolution and outgassing, by reducing the stable height of dikes in the subsurface, lead to considerably lower estimates for magma volume than that implied by the tall dikes modeled for dry magmas. Additionally, while overpressure does influence the volume required for intrusion, height controlled by outgassing has a much greater impact on emplacement volumes. While volume estimates can be constrained by field data, there is great variability in possible dike heights under a volcanic edifice, depending on the model applied. By considering the role of outgassing, we show that these heights may be considerably shorter than dry magma models suggest, which in turn requires a fraction of the volume required for intrusions observed at stratovolcanoes.

3.4.4 Field vs Model Differences

Our model of exsolution and outgassing impacts on dike stability is informed by direct field observations of a syn-emplacement, coupled gas and magma phase, and measurements of the minimum total porosity from dikes across the volcano. These observations are used to constrain our 15% capped porosity runs, which demonstrate that exsolution can promote in-edifice lateral propagation. However,

the model does not accurately recreate all of the field relations we observed, such as dike widths at the level of exposure, or the distal widening noted for several dikes (Moats, 1990; Poland et al., 2008). The dike opening model used for calculating stress intensity factors provides a maximum dike width at different locations along the dike. We utilized a shear modulus of 1 GPa, which produced widths of <1-8 m at the current level of exposure, which is considerably smaller than the average thickness we measured of ~20 m for most of the silicic dikes. One possibility to explain the discrepancy in dike widths is that the experimentally-derived shear modulus we used is too large. There is considerable variation in the volcano modeling literature as to an appropriate value of shear modulus (from 0.04 to >30 GPa) (Heap et al., 2020 and the sources therein). Many of these studies utilize laboratory-derived values (e.g., Holohan et al., 2011; Rubin & Pollard, 1987), volcanic rocks at the crustal scale may behave differently than at the laboratory scale, and actually have very low shear moduli.

An alternate explanation for the difference between model and field observations of dike thickness is that our overpressures are too low. Increasing overpressure results in wider dikes (outgassed trachytes: <0.5 m opening at 2 MPa, ~5 m opening at 6 MPa) per the relationship:

Eq. 3
$$t = P_0 a \frac{(1-\nu)}{\mu} \left[1 - \left(\frac{y}{a}\right)^2\right]^{1/2}$$

Where t is the dike thickness, P_o is the overpressure, a is the dike half-height, ν is Poisson's ratio, μ is the shear modulus, and y is the distance from the dike center. However, as our model shows, increasing pressure decreases the realm of stability and results in shorter dikes than those observed at Summer Coon. If the dikes were emplaced at higher overpressures than we modeled, they may have had stable lateral intrusion close to the edifice, but unstably propagated through the edifice at the flanks. This change in propagation direction, where it laterally propagated and switched to inclined or vertical intrusion, is inferred for Dike S (Aksit et al., 2025). This is well-documented at modern volcanoes such as Mt. Etna and Miyakejima where dikes will erupt at a flank vent, but continue propagating down-slope even after erupting (Acocella et al., 2003; Geshi et al., 2020). There is also the possibility that the large dikes were not intruded in a single pulse but formed from multiple intrusion events, which would only require smaller magmatic overpressures during intrusion. While we interpret several dikes (i.e.: Dike D) to have intruded as a single event, there is not sufficient evidence to completely rule this process out for

all Summer Coon silicic dikes.

Many of the dikes at Summer Coon are observed to get wider towards the distal ends (Moats, 1990; Poland et al., 2008). The dikes modeled here have either relatively stable widths at the level of exposure, or decrease in thickness as they approach the distal flanks (Fig. 3.9). Our model does not consider free surface effects due to the boundary at the edifice surface, which can modify the traction calculations performed to determine dike opening. Close to the volcanic center, where the dikes are deeper in the subsurface, free surface effects would have a negligible influence. However, as the dikes get closer to the edifice surface, the free surface effects could play an important role in controlling propagation and opening (Rivalta & Dahm, 2006).

3.5 CONCLUSION

In this work, we modeled the impact of volatile exsolution and outgassing on dike stability under a volcanic edifice to explain the patterns in flow direction and porosity found for large silicic dikes at Summer Coon volcano in Colorado. The dikes are inferred to have intruded laterally (Aksit et al., 2025), and have significantly low porosities (< 8% total), which we interpret as the result of outgassing through permeable pathways during propagation aided both by a low percolation threshold in a crystal-rich magmas, and high shear during intrusion. These observations led us to test how bubble growth and escape during emplacement could promote the formation of lateral dikes. Dikes are able to enter the edifice and remain stable to larger radial distances when including dynamic volatile exsolution and outgassing, which in turn modulates magmatic density during propagation. Even at the lowest overpressures modeled, dikes can enter into the volcano to the level of exposure and at the radial distances observed at Summer Coon. This suggests that modeling magma at a static density, without even considering pressure-related variations, underestimates the buoyancy of magma and its ability to enter the edifice. Once in the volcanic edifice, edifice stresses effectively trap the magma, encouraging lateral propagation. Our field-informed model for active outgassing during propagation produces blade-shaped dikes as previously argued in modeling literature (Townsend et al., 2017), and at lower volumes than would be necessary when neglecting exsolution.

3.6 BRIDGE

This chapter applied field data on porosity preserved in fifteen of the large, silicic dikes at Summer Coon to a model on dike stability and lateral propagation within a volcanic edifice. I found that volatile exsolution and subsequent outgassing, in combination with edifice stresses acting as a trap for magmas, promotes in-edifice propagation and propagation toward the flanks. For the crystal-rich trachyte dikes, I argue that outgassing is regulated by a low percolation threshold in combination with high shear at the dike margins. The rhyolite dikes, in contrast, are extremely crystal-poor but show evidence of high shear that I argue promotes outgassing to produce the low porosities measured. An alternate hypothesis for the low porosities of the rhyolites is that they were actually emplaced as a pyroclastic mix through which volatiles were lost, and the degassed fragments were amalgamated and sintered in-conduit to form the material observed at Summer Coon today. In the following chapter, I explore this possibility by mapping and characterizing different zones observed within Dike D from the micro- to the macroscale.



How to EMPLACE your RHYOLITE

CHAPTER 4

How to emplace your rhyolite: Field and microtextural evidence of emplacement mechanisms for rhyolitic dike propagation within a stratovolcano

This work was conducted in collaboration with Meredith Townsend, Thomas Giachetti, Katie Springer, Kathy Cashman, and Andrew Harp

4.1 INTRODUCTION

Rhyolitic eruption dynamics are highly complex, encompassing the entire spectrum of behavior from explosive to effusive. The eruptions of Chaitén in 2008 and Cordón Caulle in 2011-2012 were the first rhyolitic eruptions to be directly observed by volcanologists and were characterized by an initial explosive phase, followed by a prolonged period of transitionary 'hybrid' behavior, and concluded by dominantly effusive activity (Castro et al., 2012; Lara, 2009; Schipper et al., 2013). This variability in observed surface dynamics over the course of an eruption may be influenced by large scale controls like the ambient stress field (Mullet & Segall, 2021; Pinel & Jaupart, 2000), host rock properties (Kennedy et al., 2010; Schneider et al., 2012), and/or magmatic composition and water content (Degruyter et al., 2017; Eichelberger, 1995). Conduit processes occurring at depth, such as the evolution of conduit geometry (Aravena et al., 2018; Houghton et al., 2004; Mitchell, 2005), the thermal evolution of the conduit walls (Kolzenburg et al., 2019), or the nature of the conduit controlling open- or closed-system degassing (Cassidy et al., 2018; Kennedy et al., 2010; Wadsworth et al., 2020), also regulate observed eruption behavior. These processes are however either poorly captured, or uncaptured, by modern geophysical techniques. Likewise, sampling and study of eruptive products poorly constrain the evolution and minutiae of deeper conduit processes during rhyolitic magma intrusion and eruption.

There is an outstanding debate on the evolution of rhyolitic material during eruptions to produce the effusive flows observed during the final phase of activity. Rhyolitic lavas, such as those observed at the Roche Rosse flow in Lipari, Italy, and Glass Mountain at Medicine Lake Volcano in California are highly degassed, containing <0.25-0.5 wt.% H2O (Giachetti et al., 2015, 2020; Shields

et al., 2016). Several contrasting explanations have been posited to explain the low volatile content of erupted rhyolites, related to degassing processes within the deeper conduit. One end-member scenario is that rhyolitic magma, as a highly viscous fluid, experiences high shear in the conduit, which promotes brittle fragmentation at the margins and outgassing through shear-induced pathways into the host rock (Gonnermann & Manga, 2003; Rust et al., 2004). This mechanical fragmentation model requires that strain rates during intrusion exceed the brittle strength of the magma (Gonnermann & Manga, 2003). In this model, and the complementary tuffisite model whereby shear induces fractures within the conduit along which volatiles can travel, magma continues to flow as a coherent viscous fluid (e.g., Rust et al., 2004; Tuffen et al., 2003; Tuffen & Dingwell, 2005). In the alternate end-member, rhyolitic material explosively fragments at depth due to the overpressure of bubbles exceeding the strength of the magma, creating a pyroclastic mix of gas and ash through which volatiles quickly outgas. This explosive pyroclastic mixture, which has undergone "cryptic fragmentation" at depth, sinters in the conduit to reform a viscous magma (Wadsworth et al., 2022). Characteristics, such as margin brecciation, tuffisite formation and morphology, and sintering textures, can help distinguish these mechanisms from each other.

Previous work has been done to characterize rhyolitic conduits and track the evolution of magmatic material over the course of volcanic activity (e.g., Stasiuk et al., 1996; Tuffen et al., 2003; Unwin et al., 2023; Walker et al., 2017; Wolff, 1986). One particularly well-characterized example is the Mule Creek Vent in New Mexico, a preserved rhyolitic vent connected to an effusive lava flow, interpreted to have undergone the same eruptive sequence as the eruption of Cordón Caulle in 2011-2012 (Stasiuk et al., 1996; Unwin et al., 2023). This vent records initial opening and widening in pyroclastic breccia deposits that incorporate large amounts of country rock and were accreted to the conduit margins (Stasiuk et al., 1996; Unwin et al., 2023). The pyroclastic breccia is bounded by a lithic-poor, vitrophyre breccia, interpreted to have formed through the accretion and welding of pyroclasts into obsidian on the margins, and includes some in situ fractured clasts (Stasiuk et al., 1996; Unwin et al., 2023). This transitions into a coherent vitrophyre, which marks the waning of explosive activity, and at the very center of the vent a flow-banded rhyolite emplaced during the final effusive activity (Unwin

et al., 2023). Tuffisites, ash, and clast-filled fractures are observed cutting into the host rock, across the vitrophyre breccia, and within the vitrophyre and rhyolite lava units (Stasiuk et al., 1996; Unwin et al., 2023). While tuffisites can form from purely shear-induced fracturing (e.g., Stasiuk et al., 1996; Tuffen et al., 2003; Castro et al., 2012), the tuffisites at Mule Creek are inferred to have formed from pyroclastic mixtures creating fractures during explosive activity. An explosive, fragmented origin for the final rhyolitic lava is interpreted from the presence of host rock lithics in sheared tuffisites within this interior (Unwin et al., 2023). The presence of different lithologies, lithic nature and proportions, and vesicle contents, as well as tuffisite morphology, all indicate an entirely explosive origin for this vent (Unwin et al., 2023).

While Mule Creek vent exposes 350 m of the shallow conduit and records the evolution of material from initial explosive to final effusive phases of an eruption, only 150 m of this exposure would have been below the original paleosurface, a depth well above the expected fragmentation depth during the explosive phase of the eruption. Additionally, Mule Creek preserves an area of focused activity above a single eruptive, conduit (Stasiuk et al., 1996). This is in contrast to a myriad of examples of rhyolitic eruptions occurring not from a single vent, but from dike-fed rhyolitic fissures at a distance from a volcanic center (e.g., Devil's Chain, South Sister volcano, Glass Mountain flows at Medicine Lake Volcano; Donnelly-Nolan et al., 2008; Fierstein et al., 2011; Fink & Pollard, 1983). There remains a gap in analyzing the deep, non-cylindrical conduit, such as would have fed many of the recent rhyolitic eruptions in the Cascades arc, at Mono-Inyo craters in California, and at Chaitén and Cordón Caulle (Castro et al., 2013; Sieh & Bursik, 1986; Wicks et al., 2011). To address this gap, we present field observations and data from a well-exposed rhyolitic dike intruded within the paleo-edifice of Summer Coon volcano in Colorado. We collected mapping data, macroscale zonal observations, and measured kinematic indicators to interpret the emplacement dynamics of this dike over the course of intrusion. From microscale textural analysis of the different zones, we aim to determine the nature of the magmatic material during intrusion, whether it was emplaced as a coherent viscous fluid, or as a fragmented, pyroclastic mixture. This work sheds light on the processes occurring in the deeper rhyolitic conduit, and aims to link subsurface material characteristics to what is observed in eruptive deposits.

4.2 GEOLOGIC BACKGROUND

Summer Coon is an eroded stratovolcano in the San Juan Volcanic Field in Colorado, active between 33.5-32.8 Ma (Lipman et al., 2024). Over this period of activity, Summer Coon had three distinct phases of magmatism: an early basaltic-andesite phase, a middle rhyolitic phase, and a late intermediate phase (andesite to trachyte) (Lipman, 1968; Mertzman, 1972). What remains of the edifice is primarily composed of basaltic-andesite breccia, along with smaller preserved rhyolite and dacite flows (Fig. 4.1; Lipman, 1968; Lipman et al., 2024; Mertzman, 1972). Reconstructions of the edifice from this preserved stratigraphy suggest that the peak of the edifice was originally at least ~2200 m above the base level of the volcano, and that the current level of exposure within the eroded edifice is ~300 m above the volcano base (Harp, 2021; Moats, 1990). Erosion has exposed hundreds of radial dikes about the center of the volcano, which represent the entire array of magmatism expressed at Summer Coon in terms of magma composition (Lipman, 1968; Lipman et al., 2024). Of these dikes, several hundred are smaller basaltic-andesite dikes and approximately twenty are large intermediate-to-felsic dikes (Lipman, 1968; Mertzman, 1972).

Three of the well-exposed, large silicic dikes (Dikes D, E, and R; Fig. 4.1) are continuously low-silica rhyolites, traceable from the hydrothermal zone around the central intrusive complex (CIC) at the volcanic center out to the distal volcanic flanks. Three other silicic dikes (Dikes I, M, and S) have isolated segments or sections with a rhyolitic composition, but with a lower wt.% SiO_2 content (Chapter 3, Fig. 3.3). The continuously rhyolitic dikes have exposed lengths of 1.5 to 3.5 km, and range in width from around 1-47 m. These are estimated to have been emplaced at depths up to 1.2 km proximally and 0.75 km (D) to near surface (E, R) distally (Moats, 1990). While the northeast rhyolitic dikes D and E show no conclusive evidence of eruptive vents, Dike R is associated with a rhyolitic lava flow or dome at Rattlesnake Ridge in the southwest (Harp, 2018; Lipman, 1968). These dikes are inferred to have intruded out toward the volcanic flanks, as previous work at Summer Coon has shown that the larger silicic dikes laterally propagated, at least in segments proximal to the edifice center (Aksit et al., 2025; Poland et al., 2004). With this interpretation, the rhyolite dikes record not just intrusion histories at various paleodepths beneath the edifice surface, but also over the course of propagation from proximal

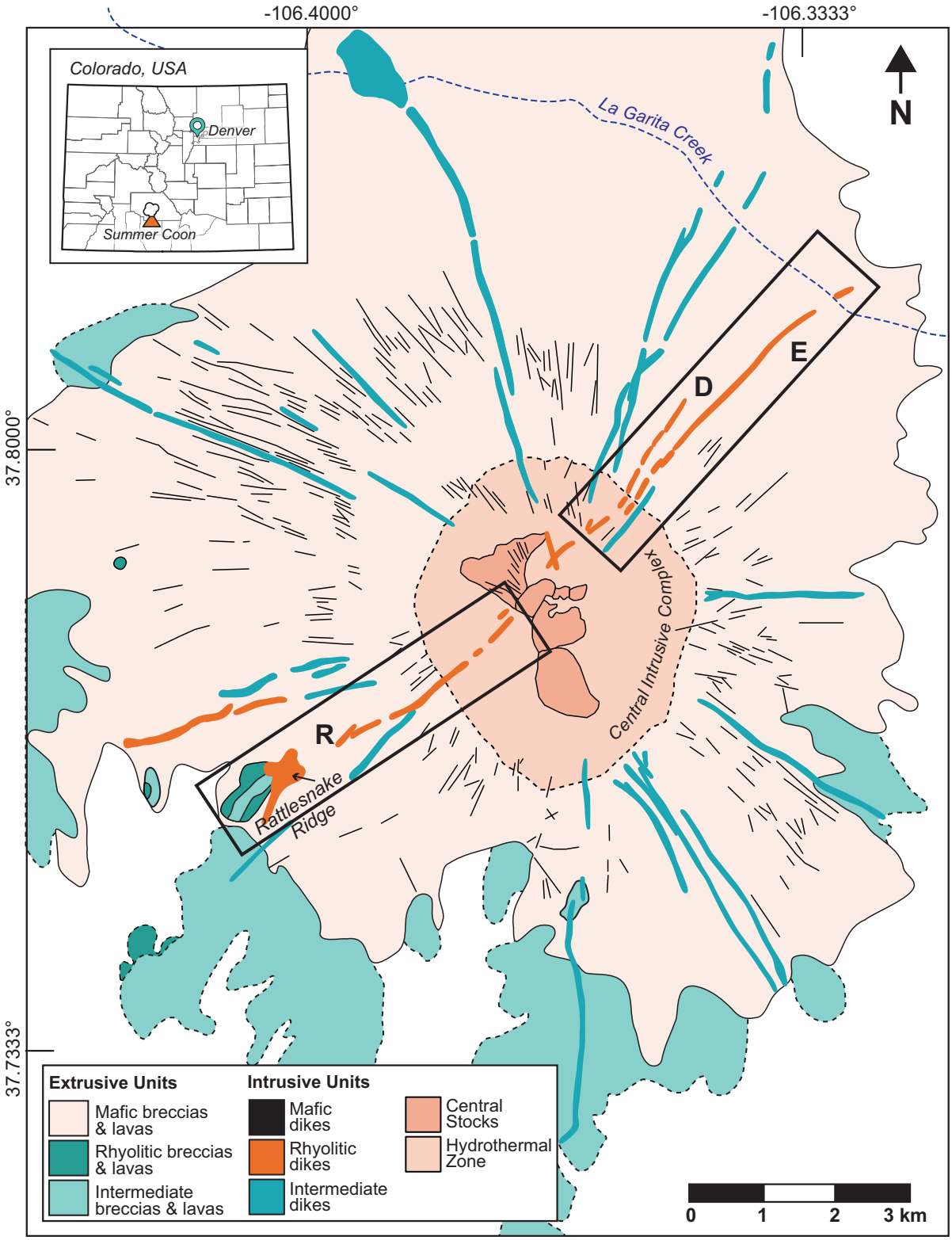

Figure 4.1. Simplified geologic map of Summer Coon volcano featuring eruptive and intrusive deposits, modified from Lipman (1976). The continuously rhyolitic dikes (D, E, and R) described here are outlined in the subset boxes. The eruptive flow associated with Dike R is marked at Rattlesnake Ridge. Dike widths and segments are not to scale.

to the vent to distal. These features make the rhyolitic dikes at Summer Coon an ideal site to study the evolution of rhyolitic material and the conduit over the course of a magmatic event.

Here, we focus on characterizing the morphology and material of Dike D to begin untangling the processes occurring within the deeper rhyolitic conduit at a stratovolcano. Dike D was selected as it has similar features (e.g., segmentation, interior zoning) as the other rhyolitic dikes, but has low relief that aids in mapping and identifying variations on a meter scale. Additionally, it has excellent field exposure for ~1 km of its 1.5 km visible length, and a distinct termination. We present macro-scale mapping data and observed kinematic indicator evidence, such as flow-banding, striations, and stretched clasts, to interpret the emplacement dynamics during intrusion. From micro-scale analysis of margin and interior material, we interpret magmatic characteristics and changes during intrusion to track the evolution of this dike from initial opening to final cooling.

4.3 METHODOLOGY

Geologic mapping of Dike D was carried out in the summers of 2022 and 2023, and covered one kilometer of exposure beginning outside the hydrothermally altered zone of the CIC (Harp, 2021; Harp, 2018; Harp & Valentine, 2018). Meter-scale, on-the-ground mapping was supplemented with a drone survey to create an orthorectified image of the dike, and aid in the identification of segment ends and stepovers. We identified three distinguishable, right-stepping echelon segments outside of the hydrothermally-altered central intrusive complex (Fig. 4.2). More segments likely exist closer to the center of the edifice further west, but the hydrothermal zone about the central stocks has altered and obscured dike material more proximally (Fig. 4.2) (Harp, 2018). The host rock in which this dike intruded is entirely basaltic-andesite breccia at the level of exposure.

In initial surveys of the dike, three distinct zones were identified: a brecciated, obsidian-rich margin (BrM), a resistant, glassy, flow-banded interior zone (GfB), and a highly fractured, platy interior zone (PI) (Fig. 4.3). Subsequent mapping focused on measuring zonal thicknesses along the entire dike length and sampling each zone from all dike segments proximal to distal. To reconstruct the dynamics of intrusion, we measured various shear sense and kinematic indicators in the field as exposure permitted,

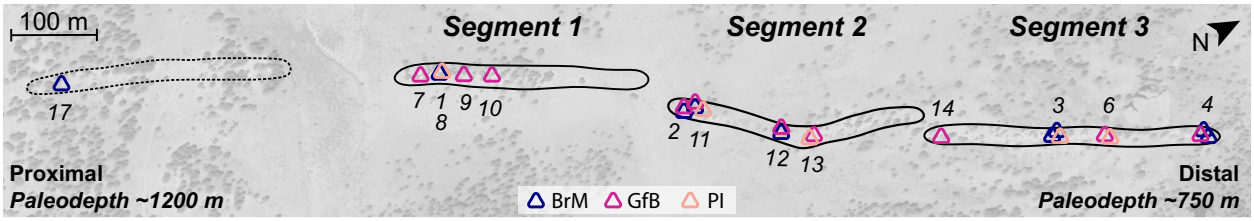

Figure 4.2. Dike D outlined over Google Earth imagery of the exposure (Google, n.d.). The most proximal, dashed segment lies closer to the hydrothermally altered zone and was not mapped in this study. The mapped segments are outlined in solid lines and labeled. Sampling location numbers corresponding to the samples analyzed in this work are marked, and samples are color coded to the zone they are collected from (purple for the brecciated margin (BrM), magenta for the glassy flow-banded interior (GfB) and light pink for the platy interior (PI)). Dike outlines widths are not to scale. Paleodepth estimates from Moats (1990) are marked at the proximal and distal ends of the dike.

including platy fractures, clasts and stretched obsidian in margins, striations, vesicle bands, flow-banding and fold orientations (Fig. 4.3) (e.g., Walker et al., 2017).

Bulk-rock geochemistry of both a proximal and distal interior sample was measured by X-ray fluorescence spectroscopy at Washington State University's Peter Hooper GeoAnalytical Laboratory. Interior samples were selected over margin samples to avoid potential contamination from host rock or lithic clasts seen in the brecciated zone. This data is used to correlate segments from proximal to distal, and to distinguish Dike D from the other rhyolitic dikes at Summer Coon.

Thirty-six samples were collected in total, 12 BrM, 18 GfB, and 6 PI samples. Of these, 19 oriented and one unoriented sample were cut for thin sections (8 BrM, 8 GfB, 4 PI) (Fig. 4.2), which were prepared by Spectrum Petrographics Inc. Thin sections were fully imaged in plane light using a Nikon Super CoolScan 5000 ED Film Scanner at a resolution of 157 pixels per millimeter. Glass and host rock clasts were hand-traced on images of five brecciated margin samples in Adobe Illustrator for particles with a minimum width of 15 pixels (95 microns) (Fig. 4.4). All particles smaller than 100 square pixels and/or cut by the edge of the image were not considered in the analysis. The size and shape characteristics (area, perimeter, Feret diameters, dimensions of best-fit ellipse, etc.) of each particle in 2D were obtained using the regionprops function of MATLAB. An equivalent diameter was calculated for each particle by approximating a disc of the same area as the particle. Particles from each thin section were then sorted by their equivalent diameter into 30 regular logarithmic bins ranging from 0.1 to 10 mm. By plotting the cumulative number density of particles as a function of their equivalent diameter in

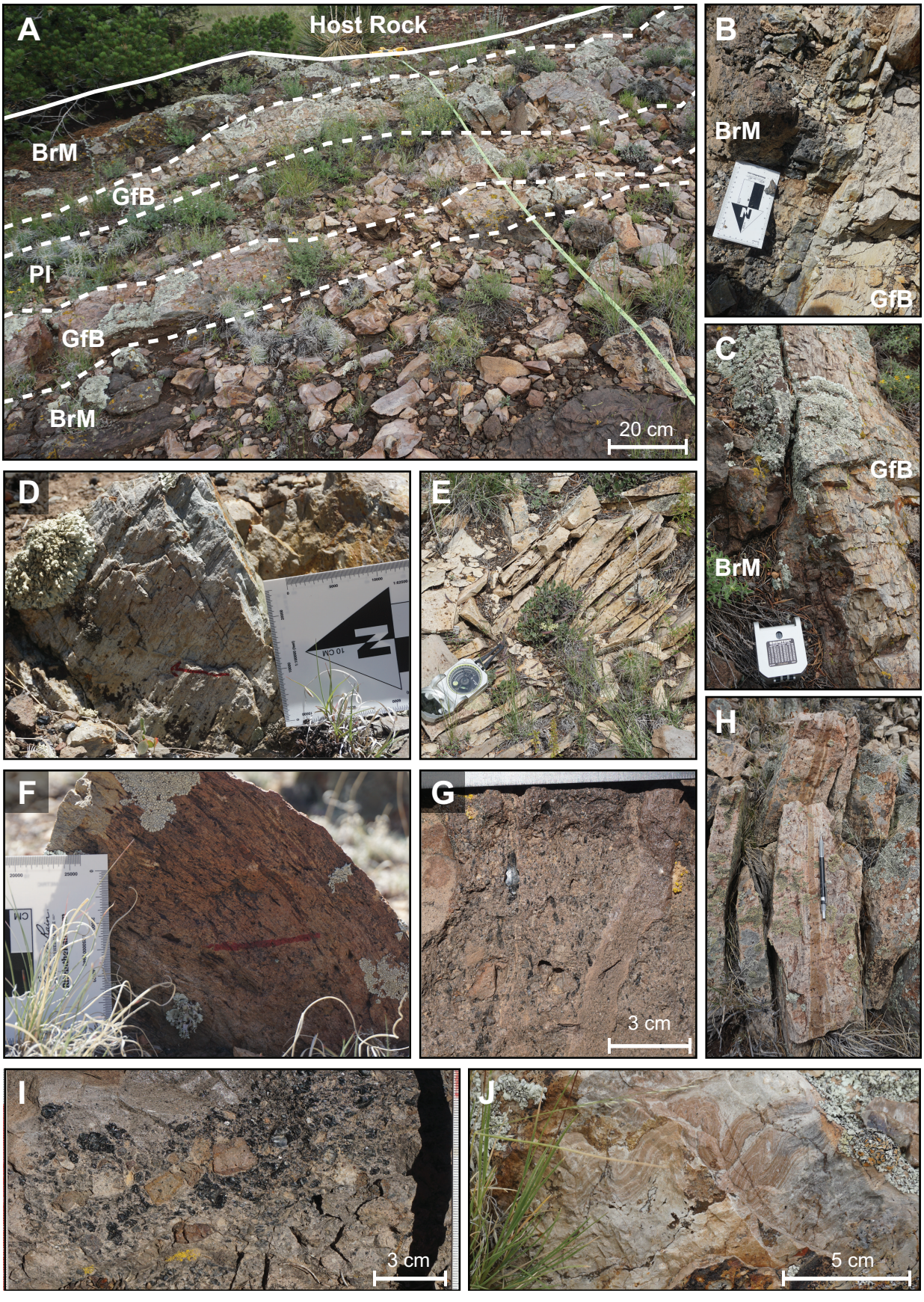
A
Host Rock
BrM
GfB
Pl
GfB
BrM
20 cm
B
BrM
GfB
C
GfB
BrM
D
E
F
G
3 cm
H
I
3 cm
J
5 cm

Figure 4.3. ***(Previous Page)*** Field photos from Dike D highlighting key features and kinematic indicators measured. (**A**) shows an outcrop exposing all three zones. (**B**) shows a gradational contact between the BrM and the GfB, while (**C**) shows an example of an abrupt contact between these two zones. (**D**) shows striations in the GfB, where the red line marks horizontal. (**E**) is an example of plates seen in the PI. (**F**) shows both vesicles and striations in outcrop in the GfB. (**G**) and (**I**) are examples of stretched obsidian and aligned clasts. (**H**) and (**J**) show flow-banding, with (**J**) displaying folding in the banding.

a double logarithmic plot, we determined whether the glass and/or host rock distributions were fractal, and if so, we calculated their fractal dimension. This analysis, accompanied by a comparison of the size and shape distributions of the clasts from proximal to distal, enables us to determine the mode of brecciation or fragmentation during the initial stages of intrusion recorded in the brecciated margin.

Backscattered-electron (BSE) images of six thin sections, a pair of GfB and PI for all three segments, were obtained using the ThermoFisher Scientific Apreo 2 scanning electron microscope (SEM) at the University of Oregon to look for textural evidence of fragmentation and cooling histories. Thin sections were imaged at 250×, 500×, and 1000× magnification to look for sintering and flow textures, and differences in glass character in the brecciated margins. Interior samples were further processed in Fiji to isolate and quantify proportions of three phases (pore space, pure silica, and microlites) between the GfB and PI (Schindelin et al., 2012). These proportions are used to look for variations between the interior zones that could be related to differences in cooling time or changes in intruded material during propagation.

The microscale variations in porosity measured via thin section are compared to total porosity measurements collected using helium pycnometry from all zones. Helium pycnometry was carried out for 19 cubes of volumes ranging from 10.5-43 cm^3, as measured using the Archimedes principle. A single sample <10 cc was measured from the platy interior, due to the thin nature of the plates and size constraint of the reference chamber. Solid cubes were measured in a 100 cm^3 reference chamber AccuPyc II 1340 Helium Pycnometer, while a corresponding portion of powdered material was measured in a 10 cm^3 chamber (Klug & Cashman, 1994). Total porosity changes are tracked for each zone over the length of the dike to look for changes in densification, which could indicate emplacement mechanism, and address degassing and volatile loss during propagation.

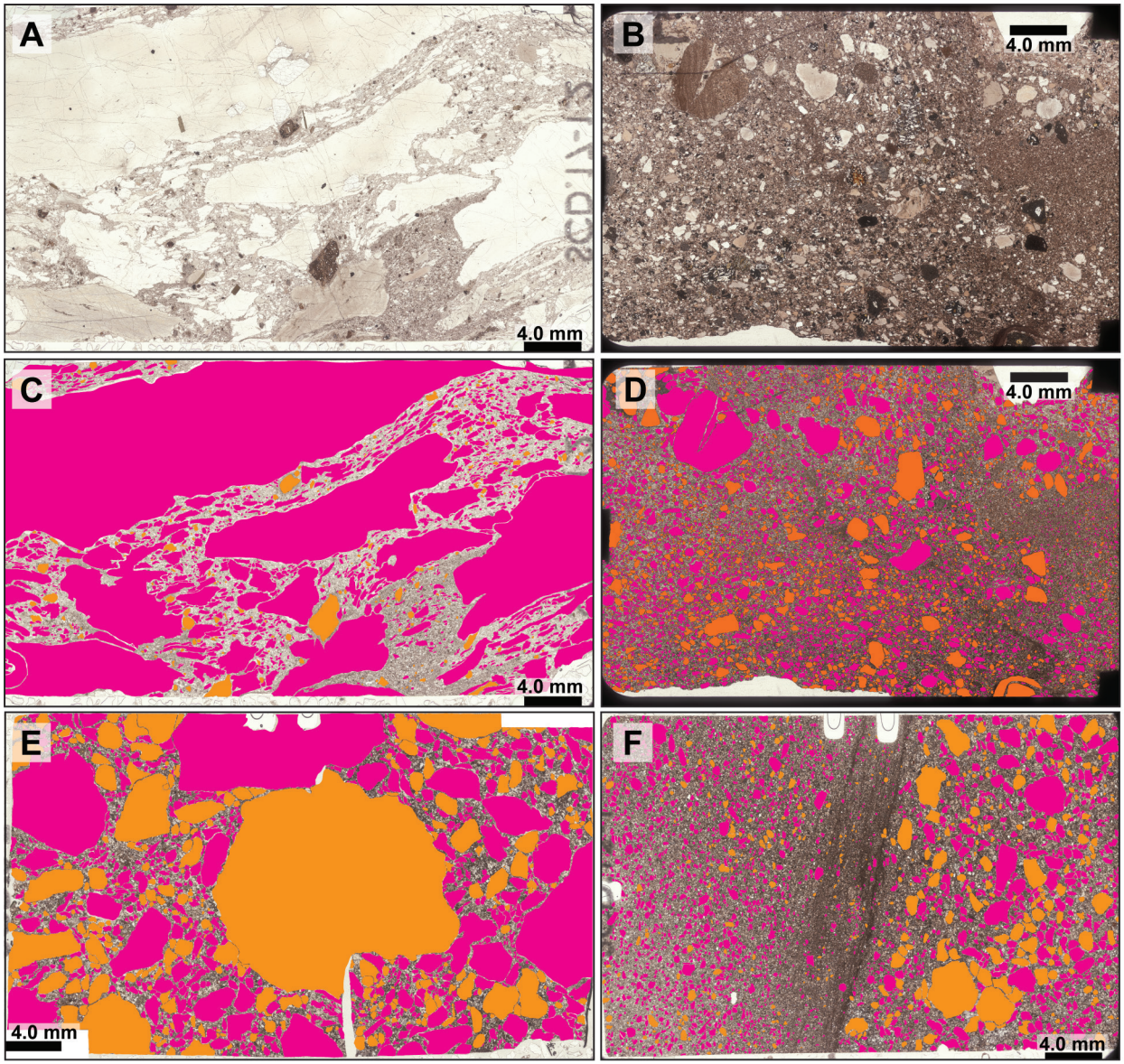

Figure 4.4. Selected brecciated margin thin sections used for analysis here, in plain light at the same scale. **(A)** is the most proximal, unoriented sample (SCD.17-1.2) and **(B)** is the most distal oriented sample (SCD.4-1). Glass clasts are identified as clear to light beige particles, while host rock clasts are dark, variably crystalline particles. The glassy matrix is the darker reddish material. **(C)** is SCD.17-1.2 and **(D)** is the traced SCD.4-1, with host rocks outlined in orange and glass in pink. **(E)** is another example of BrM analyzed more proximally in the second segment (SCD.5-2), and **(F)** more distally in the second segment (SCD.12-1) Clasts smaller than 15 pixels wide were not traced. SCD.12-1 shows three distinct zones, a larger grained right zone, a very fine grained middle zone, and an intermediate grained left zone. These zones were analyzed separately to capture the heterogeneity of the sample.

4.4 FIELD OBSERVATIONS

We identified the beginning of the first, traceable segment (Segment 1) 672 m beyond the first appearance of the dike proximal to the CIC (Fig. 4.1; Fig. 4.2) (Lipman, 1968), and it is 273 m long with an average strike of N25°E (Fig. 4.2). The first outcrop of the second segment is 47 m north of the first segment, after a 38 m right step. This second segment continues for 283 m, beginning at an average strike of N38°E and turning to the north to end with an average strike of N16°E before stepping right 27.6 m to start the third segment. The third segment is 311 m long with an average strike of N19°E, and terminates at a smaller, previously unmapped mafic dike aligned northwest-southeast, perpendicular to the strike of Dike D. Dike widths range from ~1 m up to 9.1 m, with widths generally decreasing near segment ends (Fig. 4.5). The paleodepth for the start of Segment 1 is estimated to be ~1.1 km, and the most distal paleodepth at the end of Segment 3 is ~750 m (Moats, 1990).

The three zones identified (brecciated margin, glassy flow-banded and platy interiors) are seen on both sides of the dike, although exposure of these zones is neither symmetrical nor continuous across the dike (Fig. 4.5; Fig. 4.3). These zones have defined characteristics from the macro- to the micro-scale, and feature various kinematic indicators that inform on the emplacement and cooling history of Dike D. Here, we report on identified striations, vesicle bands, flow-banding, and aligned clasts that are interpreted to reflect the direction of magma intrusion (e.g., Smith, 1975; Walker et al., 2017). We also measured the orientation of fractures in the platy interior to look for trends in alignment along dike length to infer the cause of their formation.

4.4.1 Brecciated Margin (BrM)

The brecciated margin, where visible, is the outermost zone of intruded dike material in direct contact with the host rock. This zone ranges in width from 20 cm to 2.3 m for a single side of the dike (Fig. 4.5). In many locations, the brecciated margin is not seen in-place in outcrop, but may still be seen in the loose, eroded float over the dike. Where it is present, both the west and east margins combined account for anywhere from 4.3 to 100% of the dike width, averaging ~15% for the mapped segments (Fig. 4.5).

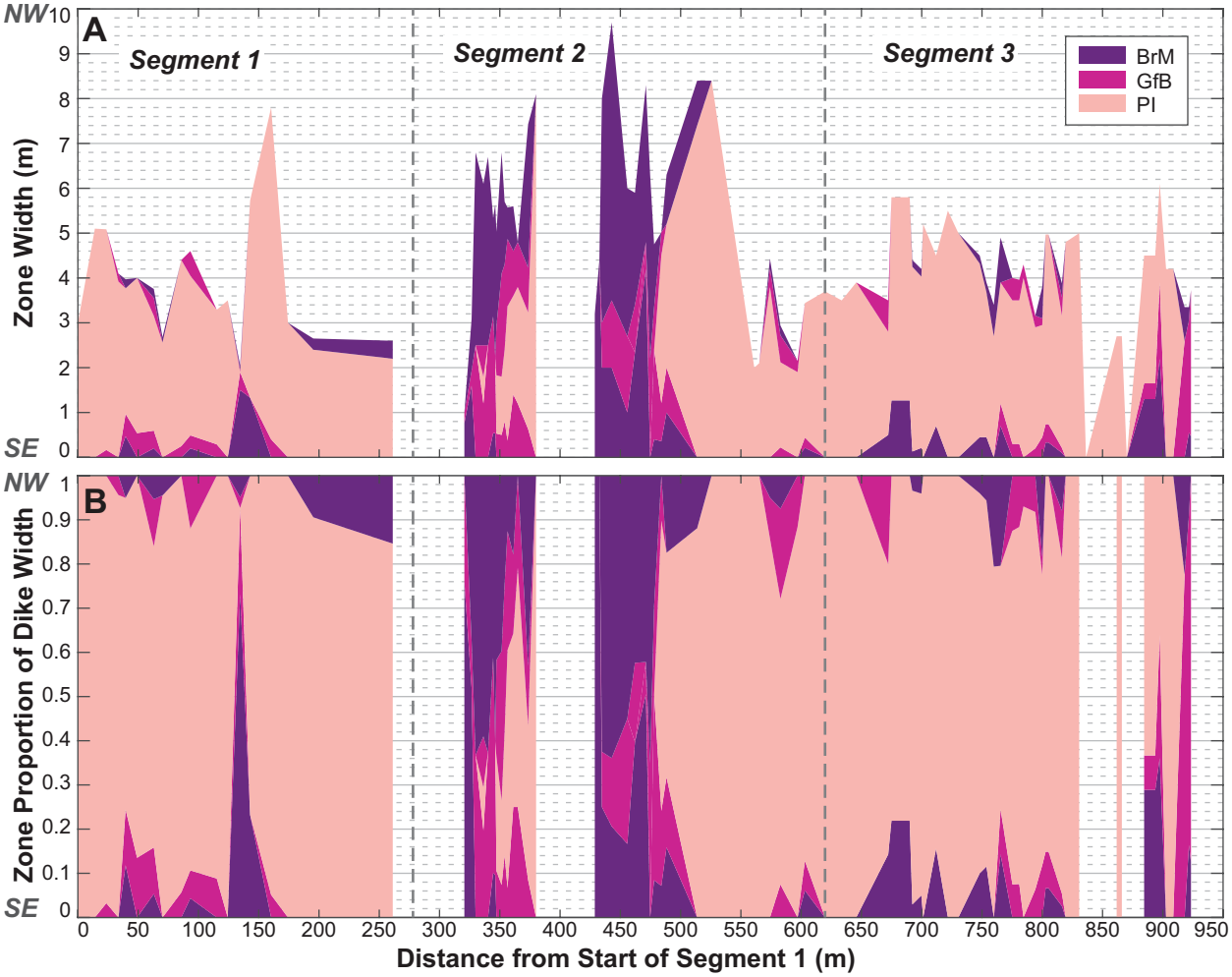

Figure 4.5. Zonal thicknesses along the length of Dike D from the beginning of Segment 1, presented in (**A**) as the width measured in the field and in (**B**) as each zone's proportion of the total width of the dike. Brecciated margins are dark purple, glassy flow-banded zones are magenta, and play interiors are light pink. Vertical dashed lines mark the end of segments, where they are observed to step. Areas without conclusive data are depicted as gaps. The top of each graph marks the northwest margin of the dike, and the bottom denotes the southeast margin.

This zone is a highly friable, clastogenic zone, featuring host rock clasts and obsidian fragments ranging in diameter from sub-millimeter to several centimeters. These clasts are often aligned or stretched, indicating local flow dynamics during emplacement (Fig. 4.6B-D; Fig. 4.7). There is heterogeneity within this zone where bands of finer-grained material are in contact with bands featuring larger clasts, which is also evident in image analysis of SCD.12-1 (Fig. 4.6C-D; Fig. 4.4). At the thin section scale, this zone has variable glass to host rock proportions along the dike length. Proximal samples are characterized by ductilely-deformed glass (Fig. 4.4A; Fig. 4.6E), while glass in the distal samples shows

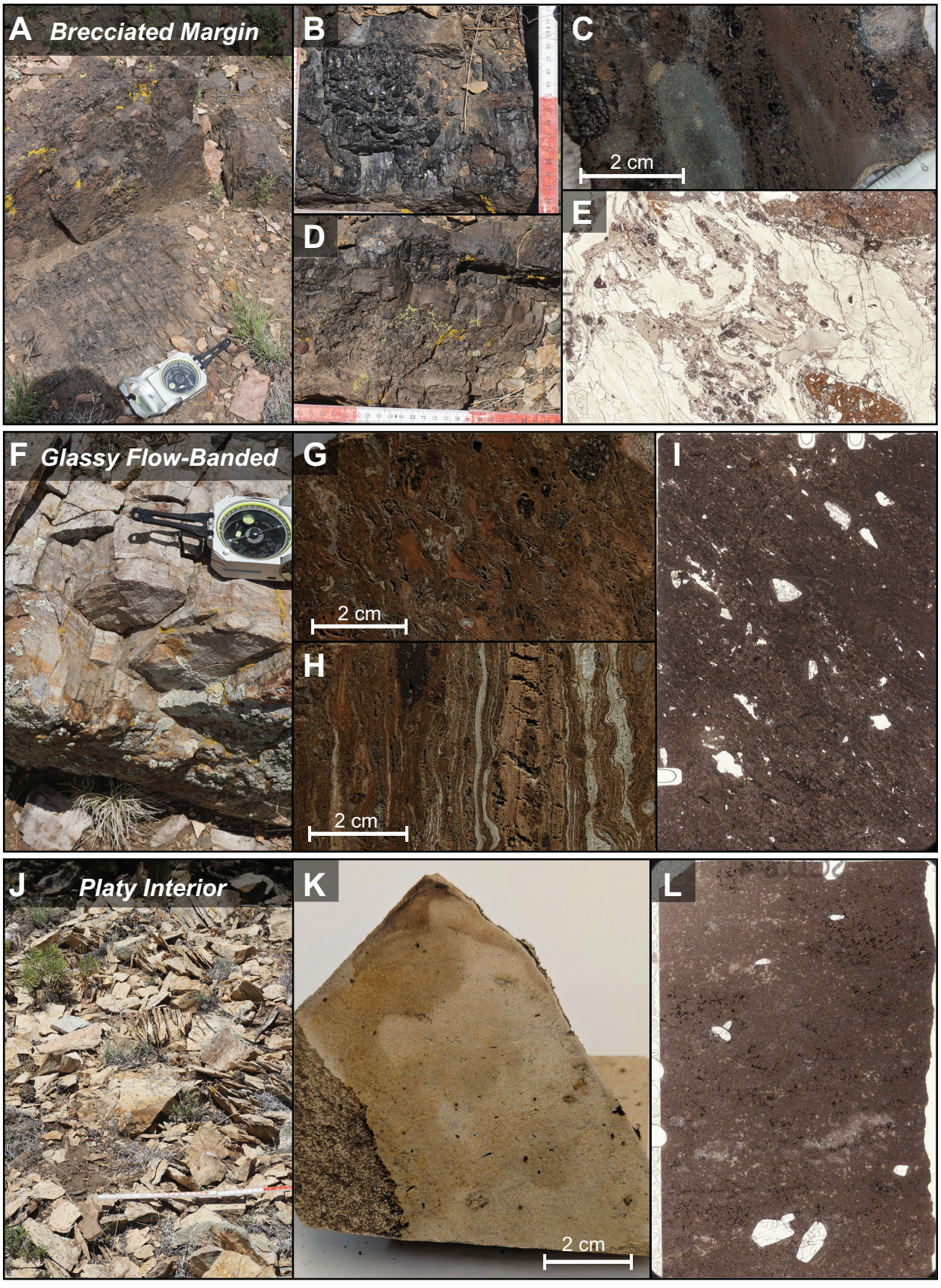
A Brecciated Margin
B
C
2 cm
D
E
F Glassy Flow-Banded
G
2 cm
H
2 cm
I
J Platy Interior
K
2 cm
L

Figure 4.6. ***(Previous page)*** Field photos (**A, B D, F, J**), hand sample images (**B, D**), and plane light thin section images (**E, I, L**) from each of the zones identified in this work. (**A-E**) show the variety and heterogeneity of textures observed at the various scales in the brecciated margin. (**F-I**) show the glassy flow-banded interior, with (**G**) displaying the typical, tortuous banding seen in this zone, and (**H**) displaying a unique example of banding accompanied by fracture (SCD.6-1). (**J-I**) show the platy interior, with (**K**) and (**L**) highlighting the crystal-poor, amorphous nature of this zone.

evidence of brittle deformation (Fig. 4.4B). Results of image analysis from this zone are presented in a following discussion.

4.4.2 Glassy Flow-Banded Interior (GfB)

The glassy flow-banded zone is a resistant interior zone in direct contact with the brecciated margin (Fig. 4.6). At times this contact is abrupt (Fig. 4.6B), but at other times it is gradational into the BrM (Fig. 4.6C). The GfB forms resistant ledges 25 cm to 1.7 m wide on a single side, accounting for approximately 3-87% of the dike width where visible (Fig. 4.5). On average, the glassy flow-banded interior makes up only 9% of the observed dike width.

As with the BrM, there is some heterogeneity in how the GfB presents in the field and hand-sample. Generally, the glassy flow-banded interior appears as a dense, variably banded and folded unit (Fig. 4.6). Occasionally millimeter-sized host rock clasts or xenoliths are present, but it is distinctly obsidian- and crystal-poor. Aligned pore space is visible at all scales of imaging in this layer, and in some samples displays evidence of being folded. In thin section, this zone has an amorphous matrix, which is composed of a pure silica phase and microlites when viewed in the SEM, along with visible aligned pore space (Fig. 4.4).

4.4.3 Platy Interior (PI)

The interior-most zone, and that most seen in the field, is the platy interior defined by the plate-like, vertical fractures that are ubiquitous throughout (Fig. 4.6). This zone is usually in contact with the glassy flow-banded interior, however there are portions in Segment 3 where the platy interior is flanked by brecciated margin (Fig. 4.5). Where it is in contact with the GfB, the contact is gradational and paralleled by the onset of platy fractures. This zone forms the majority of what was mapped, with PI

widths ranging from 60 cm up to 7.4 m, making up 10-100% of the mapped width. On average the platy interior forms 71% of the observed dike width, although this is taken to be a maximum estimate since areas with BrM and GfB in the float were not given thickness values for these zones, but the dike width was estimated from the presence of basaltic-andesite breccia on either side of the dike.

The platy interior is relatively homogenous compared to the BrM and GfB. The greatest variation is in the size of interior plates (0.1-5 cm thick), and the orientation of plates across the dike at various locations (Fig. 4.7). In hand sample, these are extremely crystal poor, have small pores, and are generally structureless, though some isolated areas with visible flow-banding exist (Fig. 4.6). In thin section, these also show an amorphous matrix composed of pure silica pockets and microlites, similar to the GfB, but this is accompanied by less-connected pore space than the GfB (Fig. 4.4).

4.4.4 Kinematic Indicators

Orientation data from platy interior fractures, limited vesicle banding, striations, flow-banding, stretched obsidian, and aligned clasts are used to interpret the dynamics of magma emplacement and cooling within Dike D. Strikes were recorded from the map view of the dike to provide information about magmatic material flow patterns in relation to the dike walls (Fig. 4.7). The plunges of different indicators, taken face parallel to the dike margin, are presented to inform on flow direction relative to volcano base where measurement was possible (Fig. 4.8). Plates are observed in the platy interior of every segment. Plates closer to the margin tend to be parallel with the localized direction of dike strike (Fig. 4.7). There are areas where interior plates are actually near perpendicular to strike, usually at the very center of the dike, with visible curvature connecting fractured plate areas nearer the margins. Vesicle bands, only observed in Segment 1 and the beginning of Segment 2, also have strikes roughly parallel to dike strike. Flow-banding is ubiquitous along Dike D, and is recorded in both the brecciated margin and glassy flow-banded interior. There is great heterogeneity in the strike of the banding, with areas that vary >30° from the dike strike, but with others that are near parallel to strike (Fig. 4.7). This heterogeneity is also reflected in the strikes of stretched obsidian and clasts seen dominantly in the brecciated margin, but also in small areas of the glassy flow-banded interior.

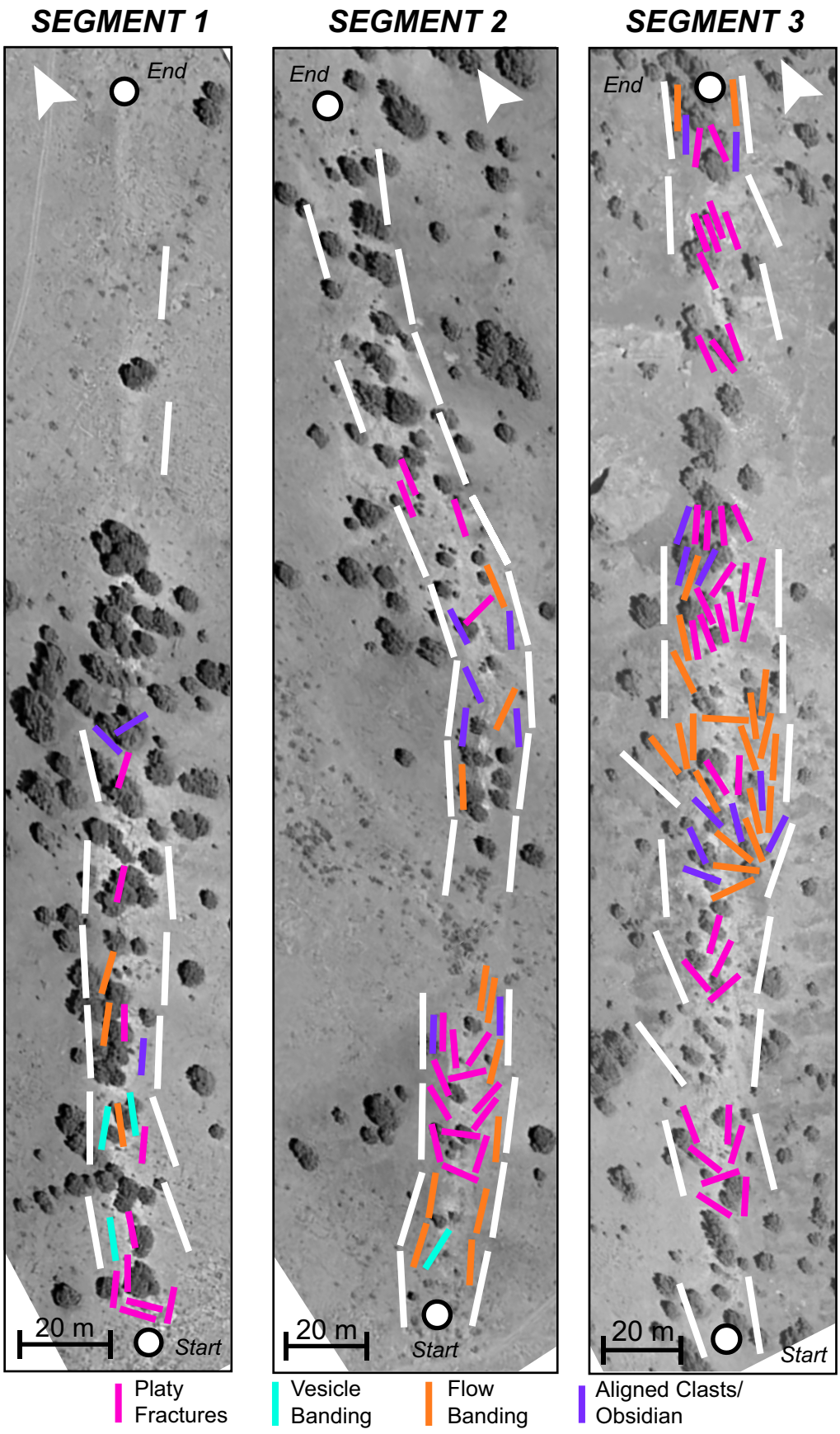
SEGMENT 1
SEGMENT 2
SEGMENT 3
End
End
End
20 m
20 m
20 m
Start
Start
Start
Platy Fractures
Vesicle Banding
Flow Banding
Aligned Clasts/ Obsidian

Figure 4.7. ***(Previous Page)*** Field measurements of the orientation of various kinematic indicators in map view plotted on Google Earth imagery of Dike D (Google, n.d.). Segment starts, from the center of the volcano, and segment ends toward the flanks are marked by circles. White lines denote the strike collected at the brecciated margin along the dike, pink lines the orientation of platy fractures, cyan lines vesicle banding, orange lines flow banding, and purple lines aligned host rock clasts and obsidian clasts. Dike widths are not accurately portrayed or to scale.

Plunges of vesicle banding, striations, flow-banding, and oriented clasts also mirror the heterogeneity observed in strikes of these indicators. In Segment 1, some areas have features with low-angle plunges (<30°), but others have intermediate to high-angle (<60°) plunges (Fig. 4.8). Even in a single outcrop, the measured plunge can vary >20°. In Segment 2, a single area of striations in the GfB produced a high-angle plunge (Fig. 4.8). This contrasts with Segment 3 in which oriented obsidian and host rock clasts are dominantly low- to intermediate-angle in the brecciated margin, with one area in the GfB showing a high-angle two-thirds along the length of the dike (Fig. 4.8). This difference in orientation of flow indicators between the BrM and GfB may reflect initially lateral intrusion of Dike D (recorded in the margins) with variation in flow after initial intrusion. This is consistent with what was found for Dike S in Chapter 2, where proximal margins recorded initially lateral propagation and interiors showed more vertical flow.

4.5 RESULTS – IMAGE ANALYSIS

4.5.1 Brecciated Margins

Traced images of the brecciated margins were compared for glass and host rock clast size distributions, aspect ratio, circularity, and fractal dimension to determine the conduit processes and brecciation style during intrusion. Aspect ratio and circularity are shape parameters that both approximate 1 for purely spherical particles. Aspect ratios above 1 describe elongate particles, and increase as the length of one axis becomes greater than the other axis. Circularity approaches 0 as particles become more irregular in shape. Particles can also be described by a solidity parameter, which measures the concavity of a particle where values approach 0 as the shape is less approximated by a closed circle. We look for changes in these parameters to interpret if the particles were formed and altered via explosive or mechanical fragmentation.

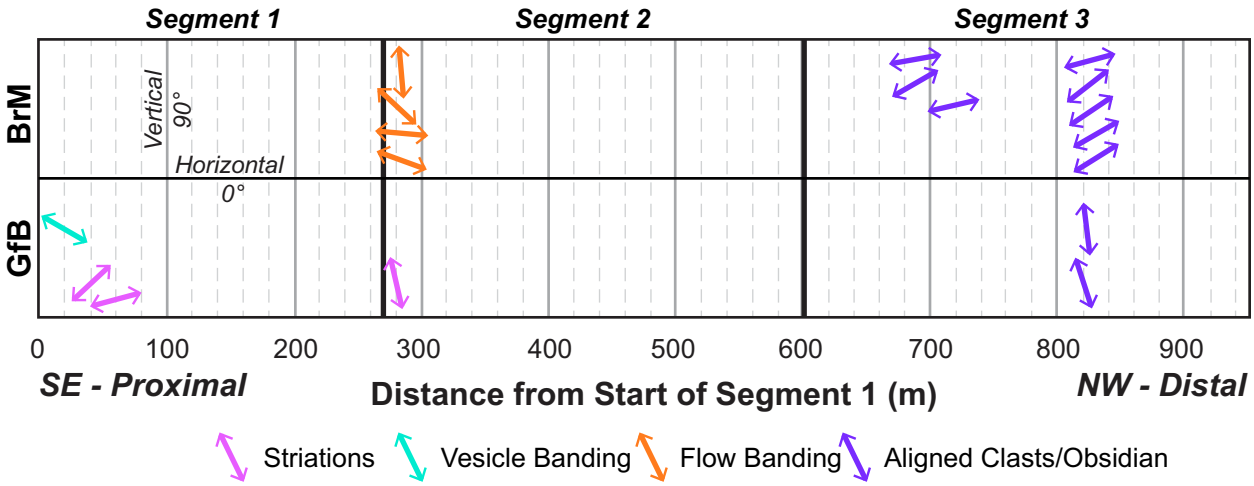

Figure 4.8. Graph of the plunges measured for various kinematic indicators along the length of the dike, color-coded to indicator type. Vertical lines mark 90° plunge, and the horizontal marks 0° plunge. Double-headed arrows indicate the implied sense of flow and ambiguity in direction. This data was only recorded in the BrM (top of graph) and GfB (bottom of graph).

The median diameter of particles within each thin section varies by more than an order of magnitude along the dike (Fig. 4.9B). There is a gap in our analysis of particles smaller than the resolution of our images (<10-2 mm), and of particles larger than the size of the thin sections (approximately >10 mm). In thin section, glass clast sizes range from 0.25-3.8 mm, and host rock clasts from 0.18-1.27 mm. The host rock particles are generally larger than the glass particles at all locations, except at the most proximal one (SCD.17-1.2). The largest glass clasts are seen in the two most proximal samples, but there is no greater correlation between the median diameter of either clast type and the sample location.

Fractal dimension was found for each thin section from the absolute value of slope of the logarithmic particle number density plotted against the logarithmic particle equivalent diameter (Fig. 4.9A) (e.g., Kaminski & Jaupart, 1998). Sample SCD.12-1 is very heterogeneous within a single thin section, and each zone in this thin section was analyzed separately (Fig. 4.4F). Fractal dimensions of the host rock and glass clasts were determined separately. Fractal dimension varies from 2.76 to 4.39, and generally increases as particle size decreases (Fig. 4.9C). The lowest fractal dimension is in the deepest sample, most proximal to the start of Dike D, however fractal dimension varies considerably from ~3.2 to 4.4 at more distant locations (Fig. 4.9D).

Several trends are seen between sample fractal dimensions and the other shape parameters.

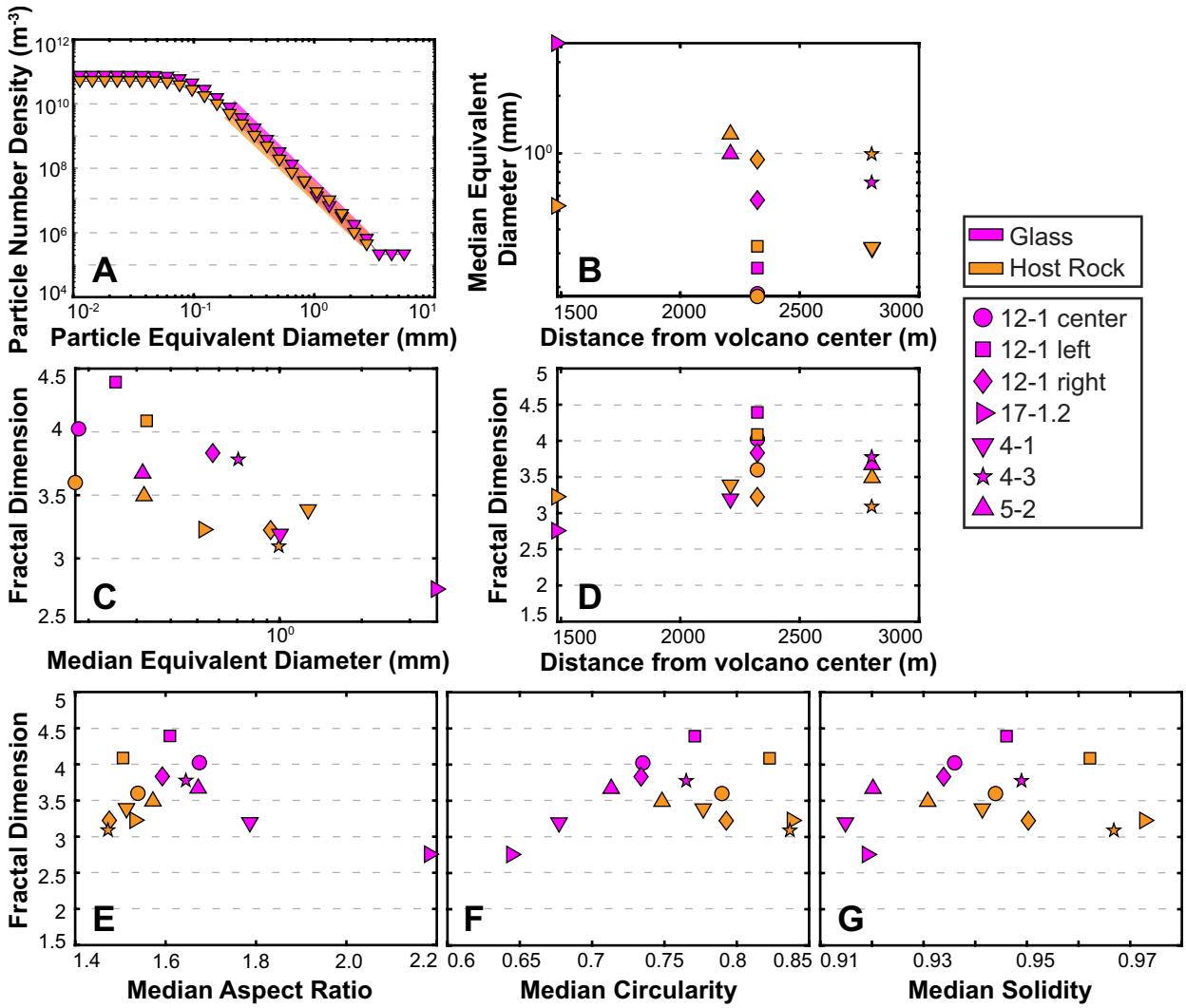

Figure 4.9. Results from the brecciated margin analysis to determine the fractal dimension for both glass and host rocks particles (example from sample 4-1 shown in panel (**A**)), and the relationship between fractal dimension and other shape parameters along Dike D (panels **B**-**G**). (**A**) shows the particle number density and particle equivalent diameters plotted to calculate the fractal dimension from the absolute value of the slope of the linear portion of the plot, shown by the heavier orange and pink lines. (**B**) and (**D**) look at the median diameter and fractal dimension for each location as a function of distance along the dike. (**C**) plots fractal dimension against the median diameter for each sample. Panels (**E**), (**F**), and (**G**) show how fractal dimension is related to three main shape parameters (aspect ratio, circularity, solidity) in both the glass and host rock.

Median diameter is negatively correlated with fractal dimension, where the fractal dimension is increasing as particle size decreases (Fig. 4.9C). Glass fractal dimensions are positively correlated with median circularity (i.e., as the particle gets more rounded), while the host rock shows no significant correlation between fractal dimension and circularity (Fig. 4.9F). There is a negative correlation between glass clast aspect ratio and fractal dimension (Fig. 4.9E), but as with the circularity, there is no

significant relationship between the host rock aspect ratio and fractal dimension.

4.5.2 SEM Interiors

SEM imaging of glassy flow-banded and platy interior samples allows for the quantification of differences in pore space, pure silica, and microlite phases between zones. Pore space is visible as black areas in SEM, and is dominantly bounded by microlites, either as large, connected pore space or in the interstitial space between microlites (Fig. 4.10). There is a small fraction of porosity that arises from fractures within silica phase zones (Fig. 4.10). Average pore space area fractions range from 6-21%, with some thin sections showing significant variation within the sample (Fig. 4.10). There is a slight increase in pore space from the glassy flow-banded zone (10 ± 6%) to the platy interior (15 ± 6%), but no significant variation in porosity exists between zones (Fig. 4.11).

The silica phase in thin section, measured by EDS as pure SiO_2, is visible as dark grey, amorphous areas, at times bounded by distinct microlites, and at other times fading into nebulous microlite zones (Fig. 4.10). Microlites are the lightest grey areas in SEM and tend to have a more tabular appearance, but some areas of microlites are more acicular and others formless. The silica phase area proportion of the glassy flow-banded zone is significantly greater (44 ± 6%) than that of the platy interior (26 ± 4%) (Fig. 4.11). This is in contrast to a significant increase in microlite area fraction from the glassy flow-banded (47 ± 5%) to the platy interior (59 ± 7%).

4.5.3 Porosity Variations

Porosity measurements using Helium Pycnometry, were completed on all three mapped zones. The total porosity measured was low, less than 25%, across all zones for Dike D (Fig. 4.12). The majority of this porosity is connected porosity. There are no trends in porosity changes from proximal (deeper) to distal (shallower) along the dike. The brecciated margin is consistently low porosity (<5%) but does present some variations even in a single location, as seen in sample 4-3 which has a porosity of 7.5% while sample 4-1 at the same location has a porosity of <0.5%. Generally, the glassy flow-banded zone and the platy interior have a higher porosity than the margin at the same location, with total porosities

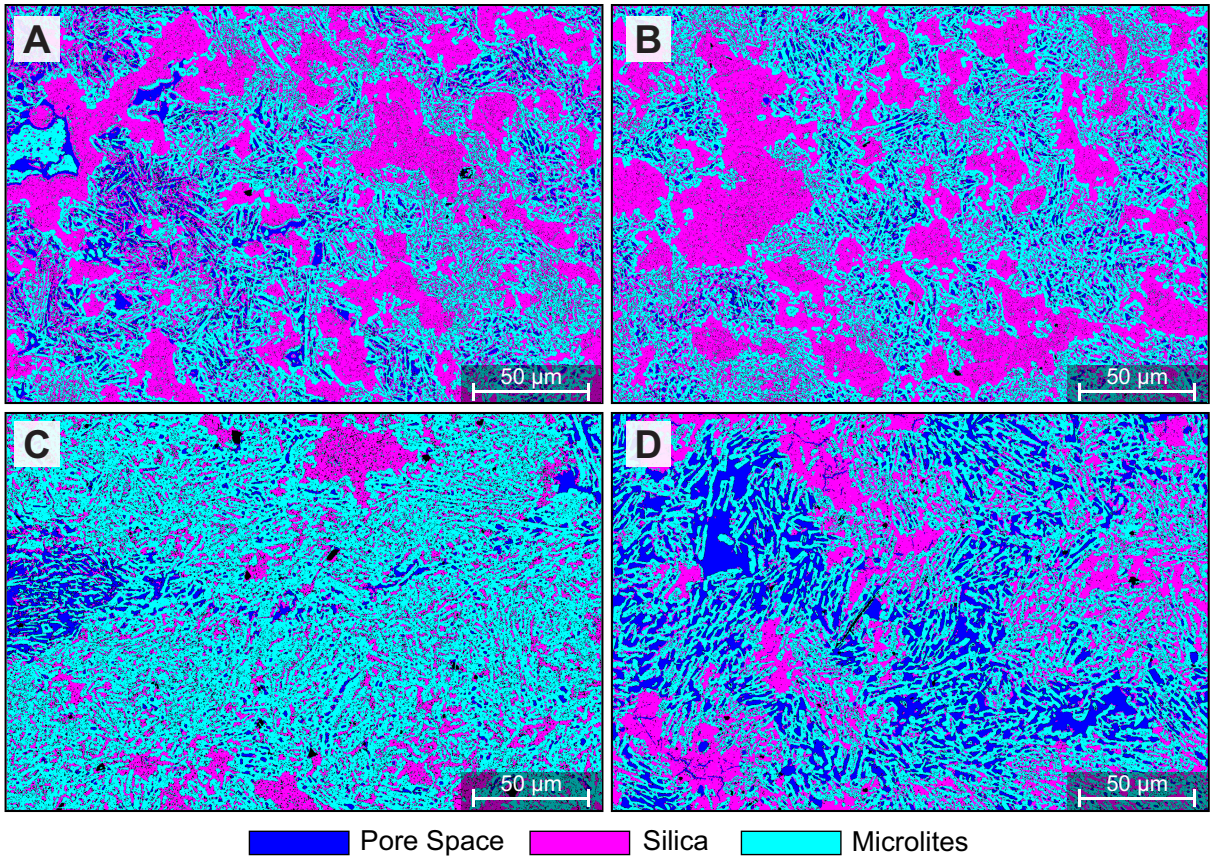

Figure 4.10. Composite images produced in Fiji of the three phases identified from SEM imagery in the interior zones, where pores are dark blue, glass is magenta, and microlites are cyan. (**A**) and (**B**) are from distal GfB sample SCD.4-5, and (**C**) and (**D**) are the corresponding distal PI sample SCD.6-4. These examples highlight the difference in microlite and glass fraction between interior zones, as well as the nature of pores observed at the micro-scale.

ranging from 3.6 to 22% (Fig. 4.12). There are no consistent trends between the interior zones in whether the GfB or PI has a higher porosity (GfB: 9.9 ± 6%, PI: 11.6 ±6%).

Helium pycnometry data and the porosity measured from the SEM image analysis both demonstrate the heterogeneity of these samples. While the general trends of pycnometry between the glassy flow-banded and platy interior zones are within the margin of error of the SEM analysis, the SEM imagery captures more variation within a single sample. Samples 7-1 and 13-2 have similar porosities from both techniques, and imagery shows consistent porosity from different areas within the sample. Samples 13-1 and 6-4, however, have considerable variation from one location to another as seen on the SEM images (13-1: 1%-20%, 6-4: 6-20%), and the pycnometry only more closely captures the lower porosity zone in each. There is complete disagreement between techniques for samples 4-5 and 8-1,

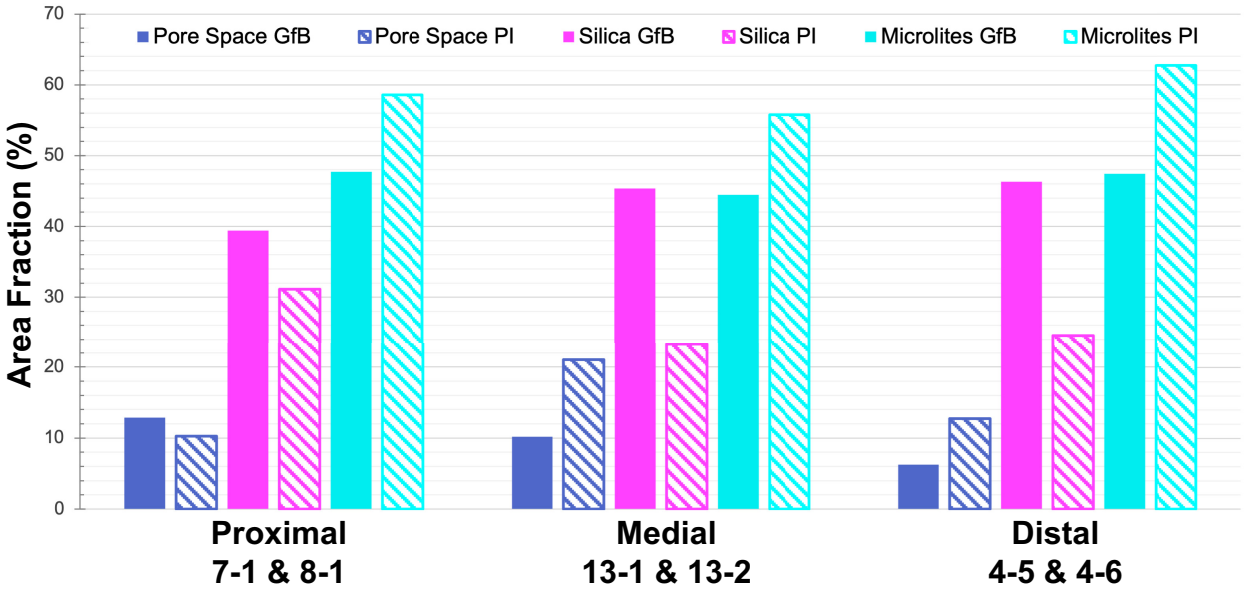

Figure 4.11. Plot of the area fraction of pore space, microlites and glass measured using SEM imagery for the glassy flow-banded zone (solid bars) and platy interior (striped bars). Colors correspond to the composite images output by Fiji, where dark blue is pore space, cyan is microlites, and magenta is the silica phase. Paired samples (i.e.: proximal GfB & PI) are shown, with proximal samples on the left, medial samples in the middle, and distal samples on the right.

where the SEM porosity is relatively consistent, but the pycnometer measurements were much higher.

4.6 DISCUSSION

4.6.1 Fragmentation Style of the Brecciated Margins

The brecciated margin records the initial stages of intrusion of Dike D, and as such is the best indicator of what the emplacement mechanisms for this dike were. Our analysis of host rock and glass clasts preserved in the margin produced fractal dimensions above 2.76, with an average >3.0 (Fig. 4.9). This is greater than the fractal dimension that may be expected for the primary fragmentation of volcanic glass (around 2.5 ± 0.3; e.g., Kaminski & Jaupart, 1998). The higher fractal dimension found for both host rock and glass clasts is consistent with secondary fragmentation as would be expected by mechanical grinding at the margin. This is further supported by the correlation between fractal dimension and shape parameters for analyzed clasts. Continuous grinding of particles reduces particle size, and in Dike D margins the particles with the greatest fractal dimension are those with the lowest median diameter (Fig. 4.9C).

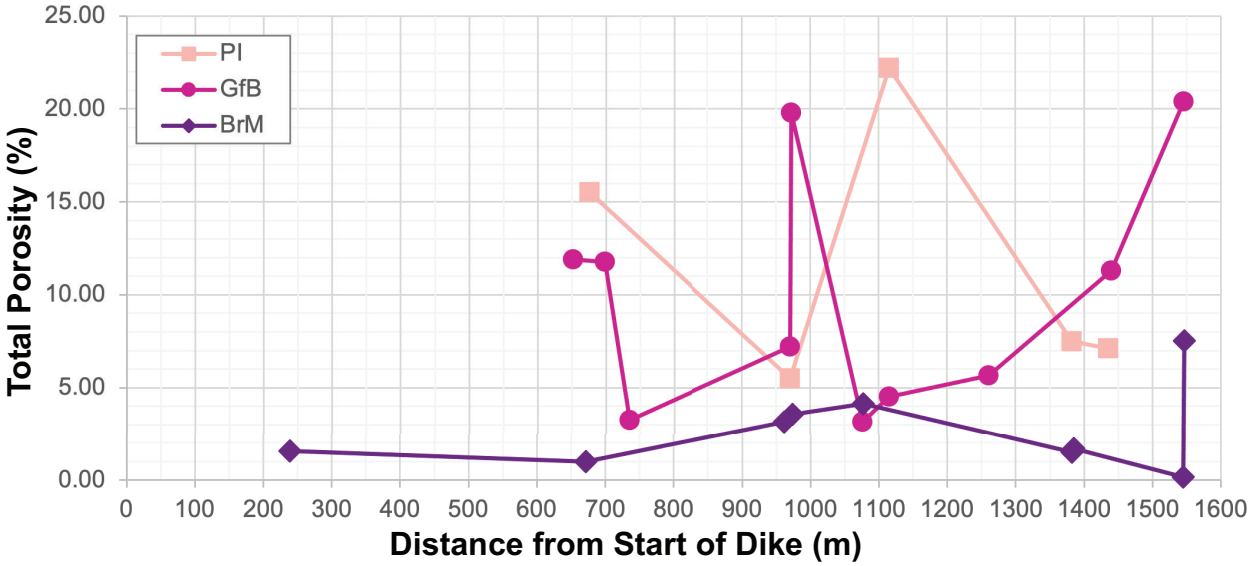

Figure 4.12. Total porosity of each observed zone measured via helium pycnometry along the length of the dike, where 0 m is the proximal beginning of the dike, nearest to the central axis of the volcano, and 1550 m is the distal end of the dike. Error bars for porosity measurements are smaller than the size of the markers.

The relationship between fractal dimension and other shape parameters varies whether comparing the glass or host rock fragments. Glass particles increase in both circularity and solidity but decrease in aspect ratio as fractal dimension increases (Fig. 4.9E-G). This is consistent with grinding, where continued grinding leads to smaller, more spherical particles. The host rock clasts, in contrast, increase in aspect ratio and generally decrease in circularity and solidity as fractal dimension increases (Fig. 4.9E-G). For these particles, grinding increases the fractal dimension and reduces size, but host rock particles become more irregular in shape rather than more uniform.

A possible explanation for this difference in shape parameters is that the glass was more ductile during shear and fragmentation than the host rock clasts. Evidence of this is seen in thin sections and SEM imagery. Proximal margin glass as seen in samples SCD.17-1.2 and SCD.1-1 is stretched and elongated, deformed without visible fracturing (Fig. 4.4A). SEM imagery of these samples shows sintering textures between clasts, which indicates higher temperatures were present (Fig. 4.13A). Distal glass may still have been warm and ductile, but also shows evidence of brittle fracture (Fig. 4.4B). The host rock would have been the ambient temperature of the edifice, much cooler than the intruded magma of Dike D, and therefore more brittle than the glass.

Field observations, particle analysis, and thin section and SEM imagery together support that

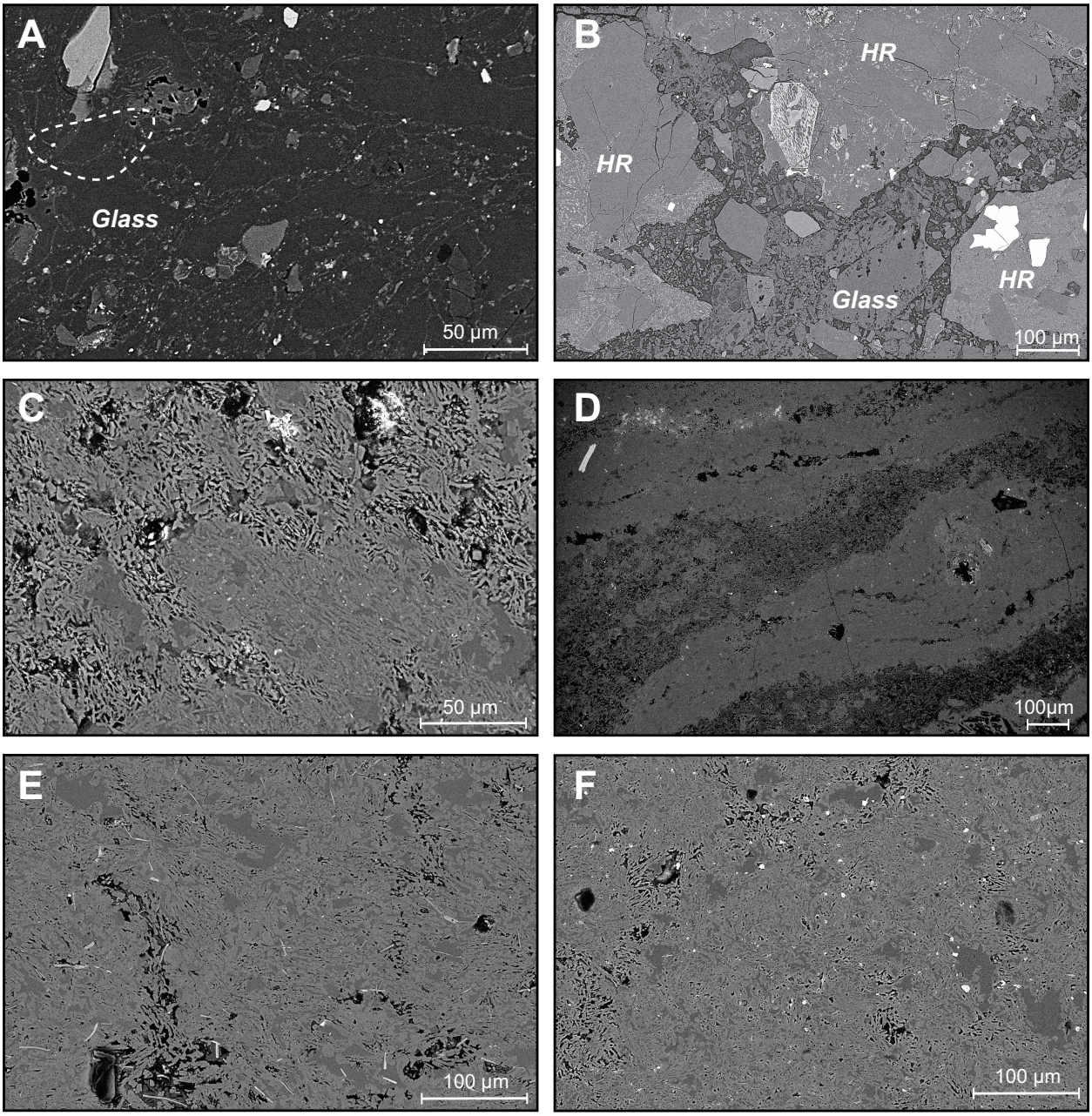

Figure 4.13. Backscatter electron imagery of proximal and distal brecciated margin, glassy flow-banded interior, and platy interior samples. **(A)** shows sintering between glass (outlined by the dashed line) in the proximal SCD.1-1 BrM sample. **(B)** is a representative distal BrM sample (SCD.4-3) showing distinctive host rock (labeled *HR*) and glass clasts, surrounded by interstitial glass. **(C)** is a proximal GfB sample (SCD.7-1) displaying the pore space (black), pure glass (dark grey), and microlite (light grey) phases isolated in the composite images (Fig. 4.10). Bright white crystals are oxides. **(D)** is from distal GfB sample SCD.6-1, with abundant pore space and flow-banding. **(E)** is the proximal PI (SCD.8-1) and **(F)** the distal PI (SCD.3-2), displaying the same phases as **(C)**, with the pore space showing evidence of the potentially collapsed permeable networks we hypothesize resulted from shear post-emplacement.

the brecciated margin was formed through mechanical or shear fragmentation of a coherent, viscous magma as it intruded within the host rock. Highly viscous material experiencing sufficiently large strain rates can shift from effusive or viscous flow to shear fragmentation, or brittle failure under shear (Gonnermann & Manga, 2003; Tuffen et al., 2003). High strain rates at the margins of the dike during intrusion could have driven mechanical fragmentation of margin material. Margin glass and obsidian would have formed as the magma cooled on contact with the host rock, or fractured through shear and reannealed, and was reincorporated as the magma continued to flow (e.g., Rust et al., 2004). Closer to the edifice, and at deeper depths, the glass was newly formed, hot and ductile. As the dike propagated, this glass was cooling as new glass was formed, so that by the distal, shallower segments, multiple phases of glass formation were incorporated, with varying degrees of fragmentation (e.g. Fig. 4A-B). As bits of glass were reincorporated, host rock was also plucked from the conduit wall, and continually ground during transport. The heterogeneity observed within the margins at all scales would come about from the incorporation of new material in the course of intrusion, so that newly incorporated material was larger, and less modified. Stretched obsidian and aligned clasts in outcrop indicate that the flow and shear directions during intrusion were dominantly margin parallel, but that areas with localized differences may have come about from differences in conduit geometry.

4.6.2 Intrusion and Cooling of the Interiors

The interiors preserve evidence of the evolution of the dike after initial intrusion (recorded by the brecciated margin) to the final stage of cooling and solidification. Gradational contacts observed between the brecciated margin and glassy flow-banded interior support our preferred model for emplacement of a highly viscous magma experiencing high strain rates at the margin, where the more interior material experiences lower strain rates and thus does not fragment (e.g., Gonnermann & Manga, 2003). The interior zones are buffered from contact with the conduit walls by the brecciated margin material, and incorporate little to no host rock clasts. Highly developed flow-banding in the GfB, and to a limited extent in the PI, is indicative of the shear produced by flow during intrusion. Folding in the flow-banding implies progressive shear occurred within the dike, as shear due to flow first developed

the banding, and continued shear folded the banding (Fig. 4.3) (e.g., Tuffen & Dingwell, 2005) Strikes of the flow-banding in the GfB are dominantly margin parallel, but do show some variation (Fig. 4.7). These variations may have come about as the brecciated margin cooled, blocking the flow of interior material, or due to changes in conduit geometry (i.e., size or orientation) along the dike path.

Textural analysis of the thin sections and SEM imagery provides insight into the cooling process of both interior zones. Both the GfB and PI have very similar textures of pore, silica, and microlite phases along the entire length of the dike. In the platy interior, there is an increase in microlite content that is matched by a reduction in the silica phase compared to the glassy flow-banded zone. This implies that the glassy flow-banded and platy interior formed from the same crystal-poor, viscous material, but that the platy interior took longer to cool allowing more time for microlites to crystallize (Hammer & Rutherford, 2002).

The porosity of the interiors does not vary significantly between zones, but field evidence and micro-scale imagery of the pore space does allow us to interpret its formation. Some of the pore space is interpreted as a syn-emplacement feature, as is evident from stretched vesicle bands within the dike (Fig. 4.3; Fig. 4.7). Other areas in glassy flow-banded samples display characteristics of shear-induced porosity, evidenced by ragged open spaces aligned with flow-banding, or even as echelon fractures (Fig. 4.6). These fractures are further evidence of shear within the interior, and are a unique example of localized brittle failure in the GfB after flow-banding had developed. At the micro-scale, the presence of pores raggedly surrounded by microlites is more indicative of vesicles formed via contraction during cooling than of bubbles formed by diffusion post-emplacement (Fig. 4.13). This is supported by both fracture pore space seen in the pockets of silicia phase, and large pores surrounding large, isolated crystals that would also form during contraction (Fig. 4.13). There are indicators that some permeable networks existed prior to cooling. In these locations, larger porous areas are linked by smaller elongate porous paths, which may be evidence of permeable pathways that potentially collapsed through shear (Fig. 4.10). The orientation of plates in the platy interior zone are also interpreted as a contractive, cooling feature, forming along either pre-existing planes, like flow-banding, or along possible fractures formed by micro-scale permeable networks. Gradational contacts between the GfB and PI, and plate

development, likely arises from protracted cooling of the interior.

4.6.3 A Question of Sintering

While we posit that the interiors formed by flow of a viscous fluid buffered from interaction with the conduit wall by brecciated margin material and with textural differences resulting from cooling timespans, we must look at how long these dikes took to cool. The argument for the dikes being emplaced as a pyroclastic mixture would require the interior material to cool slowly enough to be completely re-sintered, and the textures of original fragmentation and relict clasts overprinted (e.g. Wadsworth et al., 2022). To investigate this possibility, we use a one dimensional heat conduction equation for an infinite sheet, as is appropriate for a dike (Carslaw & Jaeger, 1959):

Eq. 1
$$\mathrm{T} = \frac{1}{2}\left[\mathrm{erf}\left(\frac{\mathrm{a}-\mathrm{x}}{2\sqrt{\mathrm{kt}}}\right) + \mathrm{erf}\left(\frac{\mathrm{a}+\mathrm{x}}{2\sqrt{\mathrm{kt}}}\right)\right] + (\mathrm{T_m} - \mathrm{T_b}) + \mathrm{T_b}$$

where *a* is the dike half-width in meters, *x* is the distance in meters from the dike center, *k* is the thermal diffusivity (m^2/s) of the magma, T_m is the initial magma temperature (°C), T_b is the background temperature of the volcano (°C). We produce temperature profiles to calculate the timescales of cooling required for the magma to reach the glass transition temperature, the temperature above which rhyolitic glass is in a viscous deformation regime and fragmented rhyolitic material may sinter into a coherent, flowing magma (Gardner et al., 2017; Romine et al., 2012). The glass transition temperature ranges from ~465-620°C for rhyolitic compositions with 2.2 wt.% to 0.49 wt.% H_2O (Gardner et al., 2017; Romine et al., 2012). We use a thermal diffusivity of 5.1x10-7 m^2/s as is appropriate for rhyolitic melt (Romine et al., 2012), assume a median temperature for rhyolitic fragmented material of 800°C, and apply a slightly elevated background temperature of 50°C for the volcanic edifice (Gardner et al., 2018; Kolzenburg et al., 2019; Romine et al., 2012). Previous work on sintering timescales of obsidian ash shows that at the depths of intrusion for Dike D (~1200-700 m), for a material at 800°C, sintering can occur on timescales of about 10^2 to 10^4 seconds (Gardner et al., 2017). Sintering occurs on faster timescales for smaller particles and at higher temperatures, and occurs at slower timescales for larger particles and lower temperatures (Gardener et al., 2018).

For an average dike width of 4.5 m, a glass transition temperature of 620°C would only be

crossed in the outermost ~10 cm of the dike at the upper timescale of sintering (10^4 s) (Fig. 4.14). For purely conductive cooling, it would take 42 days for the center of the dike to cool below the glass transition temperature. These timescales are much longer than would be necessary for the complete sintering of pyroclastic fragments, and represent the upper bound of cooling for low water content glass at the highest expected glass transition temperature (Gardner et al., 2017, 2018; Romine et al., 2012). As our cooling analysis shows, it is within the realm of possibility that Dike D could have formed through the intrusion of a pyroclastic mixture of gas and ash that remained above the glass transition temperature long enough to sinter and continue to viscously flow (e.g., Wadsworth et al., 2022). However, given that shear fragmentation is strongly indicated by our analysis of the brecciated margins as the initial mechanism of emplacement, we argue that there is not sufficient evidence to suggest a change in style between emplacement of the margin and interior.

4.6.4 Comparison to Exposed Conduits

Shallow rhyolitic conduits, such as the Mule Creek Vent, have many similar features to what we observe in Dike D. Each of these conduits preserves a brecciated outer margin, a lithic-poor, glassy (vitrophyre) layer in contact with the breccia, and a flow-banded interior with developed platy fractures (Stasiuk et al., 1996; Unwin et al., 2023). While Mule Creek is directly linked to surface pyroclastic deposits, and partially cuts them, Dike D has no such correlation at Summer Coon. The greatest difference between the two exposures is the prevalence of tuffisites, whether within the conduit itself or cutting into the host rock. At Mule Creek Vent, these ash and clast filled fractures are interpreted as forming during the initial explosive opening of the conduit, and later interior-cutting tuffisites formed during continued eruption and opening via explosive processes (Unwin et al., 2023). At Dike D, in contrast, we did not observe any tuffisite veins crossing from the dike into the host rock, either because dike opening was an efficient degassing mechanism in advance of viscous magma propagation, or because continued shear fragmentation at the margin produced permeable networks for degassing (e.g. Rust et al., 2004). Additionally, no tuffisites were observed laterally cutting the zones of the dike. Where finer-grained zones are observed in the brecciated margin, we argue that these could have formed

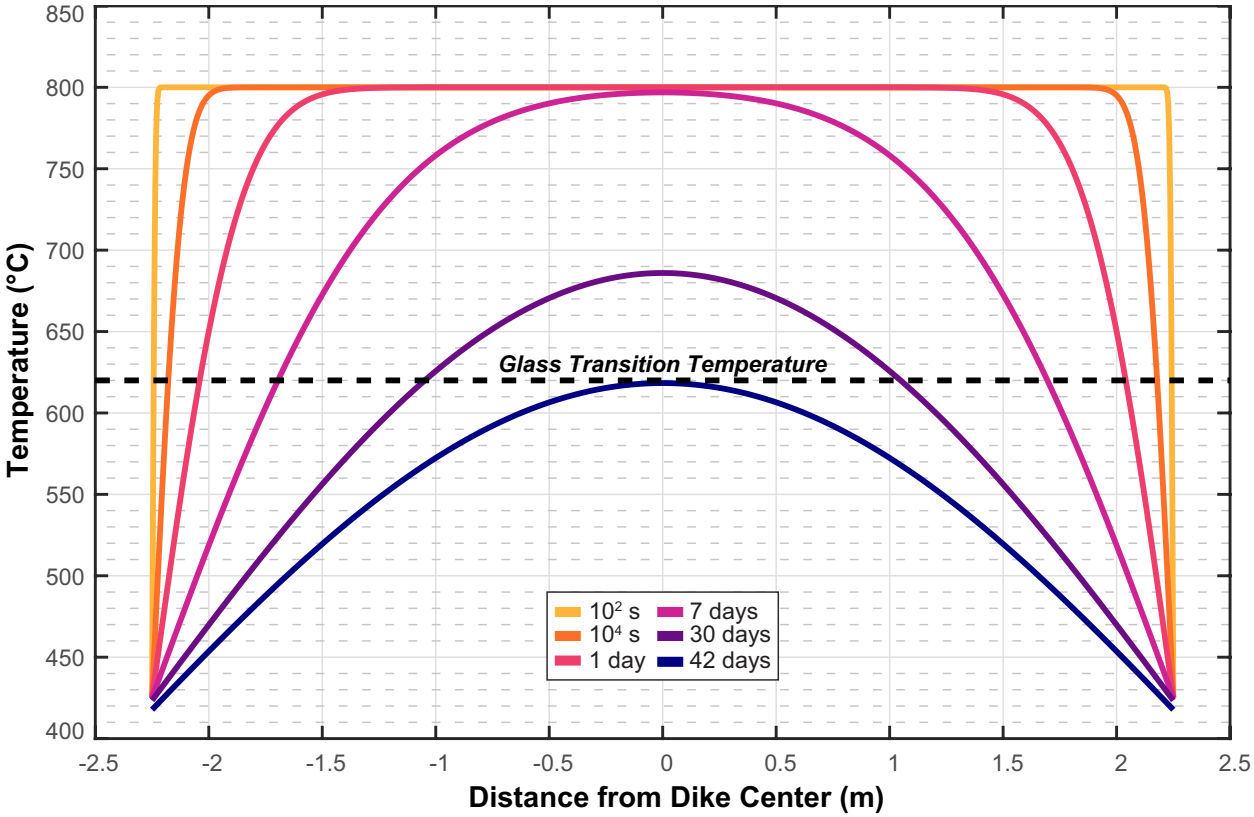

Figure 4.14. Conductive cooling curves for a 4.5 m-wide rhyolitic dike, with an initial magma temperature of 800°C and intruded into a volcanic edifice with a background temperature of 50°C. Curves for 10^2 and 10^4 s are the timescales expected for pyroclasts to sinter at 1100-700 m depth (e.g., Gardner et al., 2017). The dashed line at 620°C represents the glass transition temperature for a rhyolitic melt with 0.5 wt.% H_2O (e.g., Romine et al., 2012). The center of the dike would take 42 days to cool below this glass transition temperature, or even longer at higher water contents or higher initial temperatures (Gardner et al., 2017).

either via shear-induced fracture, as Tuffen et al. (2003, 2005) postulated for tuffisite formation, or due to strain localization during shear flow resulting in grain-size reduction, such as was observed at Mt. St. Helens during the 2004-2008 dome extrusion (Cashman et al., 2008). This tuffisite evidence, in combination with our interior textural characterization, and brecciated margin analysis, suggests emplacement aligned with the mechanical fragmentation model for Dike D, distinct from the explosive fragmentation mechanism proposed for the entire evolution of the Mule Creek Vent (Unwin et al., 2023).

4.6.5 Direction of Future Work

This work presents a look at a deeper rhyolitic conduit, intruded as a dike within a

stratovolcano. Dike D is relatively short compared to the other rhyolite dikes exposed at Summer Coon, and there is not sufficient evidence to suggest it erupted, or intruded as an open conduit with an associated vent. Dikes E and R, however, are much larger, and at least one of them is associated with an extrusive dome or lava flow (Fig. 4.1). Our interpretation that Dike D intruded as a highly viscous magma experiencing high strain rates and undergoing mechanical fragmentation at the margins but not the interiors, is based on the prevalence and characteristics of zones observed along the dike. These three zones have also been observed in Dike E. The erupted Dike R, however, is dominated by a wide glassy flow-banded zone, with some plates, but only sparsely preserved brecciated margin. There are also many locations where the glassy flow-banded zone is in direct contact with the host rock. Future work on the question of the nature of rhyolitic material intruded at depth should compare the material preserved in Dike D, E, and R, to investigate the ubiquity of these textures and inferred processes in the deeper conduit. This research avenue could determine if there is a difference in conduit interaction or the nature of material that intrudes in a closed conduit, and material that manages to erupt. Further work on constraining the strain-rate, viscosity, dike pressures, and intrusion timescales of intruded magma may also aid in unravelling the differences between rhyolitic dikes at Summer Coon.

4.7 CONCLUSION

Rhyolitic dikes at Summer Coon volcano provide an excellent opportunity to interpret emplacement mechanisms and the dynamics of high-silica magma intrusion at stratovolcanoes. The zones, kinematic indicators, and textures preserved in intruded material can shed light on the deeper conduit processes that modulate eruption dynamics observed at modern rhyolitic eruptions. Dike D is interpreted to have laterally intruded initially, and as such records the evolution of material during propagation over a ~500 m difference in emplacement depth. Three observed zones within the dike, the brecciated margin, the glassy flow-banded interior, and the innermost platy interior, record the following stages of propagation:

(1) Initial intrusion of a viscous magma experiencing high shear, and a high degree of interaction with the dike wall (i.e., host rock). Due to high strain rates at the dike wall,

the magma surpasses its yield strength and brittlely fractures, perhaps multiple times during intrusion, leading to the formation of glass clasts. Host rock clasts are variably plucked from the conduit wall and ground during transport. These clasts align with the direction of flow during intrusion. Fine-grained zones develop in the margin either as shear-induced tuffisite fractures, or from strain localization.

(2) Brecciated margins buffer the interior flowing, viscous, microlite-rich magma from interaction with the dike walls, allowing the formation of highly-developed flow-banding aligned in the direction of magma flow through the conduit. Shear continues in this zone, producing folding within flow-bands, and as the magma cools enough, continued shear produces localized echelon fracture development. Permeable networks may form paths for volatile transport within this zone, but these networks collapse under progressive shear.

(3) Flow continues until either magma source volumes are tapped, or overpressures required for continued fracture growth are no longer met. At this stage, the final magma intruded in the center of the volcano stops flowing and begins conductively cooling. This magma is the same as the glassy flow-banded zone, but protracted cooling of this zone allows for the growth of more microlites than in the GfB, and the development of plates as cooling progresses, and contraction occurs. This contraction also leads to the formation of microscale pore space.

The intrusion of Dike D is controlled by its viscosity and the strain rates experienced during emplacement of different layers. These factors in turn dictate the transition from viscous flow to mechanical fragmentation (Gonnermann & Manga, 2003). This research demonstrates the importance of textural characterization in interpreting emplacement mechanisms. Future work should explore the ubiquity of this process in the emplacement of other rhyolitic dikes at Summer Coon, particularly around a known feeder dike, Dike R.

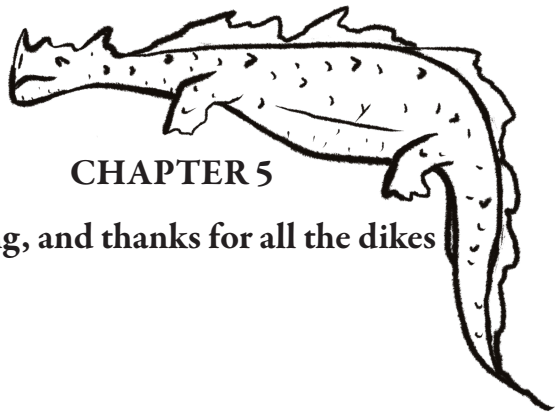

CHAPTER 5
So long, and thanks for all the dikes

Determining the controls on magmatic intrusions in modern arc settings is complicated due to their subsurface nature, a scarcity of tracked diking events at stratovolcanoes, and the ambiguity inherent in geophysical interpretation when diking is observed. The investigation of dikes exposed at eroded stratovolcanoes offers a complementary approach to determine the hierarchy of controlling factors on dike pathways. In this work at Summer Coon volcano, I combine field observations of ancient silicic dikes exposed within the paleo-edifice with lab analyses of magmatic properties and physics-based numerical modeling to investigate the factors influencing dike propagation at stratovolcanoes. I first establish that propagation trajectories proximal to the edifice are dominantly lateral, but vary distally between two silicic dikes as a result of buoyancy differences. With propagation trajectories ascertained, and after determining that the dikes of Summer Coon have characteristically low-porosities, I then utilize numerical modeling to determine that dynamic volatile exsolution and outgassing, in combination with a large volcanic edifice, could encourage the lateral emplacement interpreted for the silicic dikes. In the analysis of the silicic dikes, two distinct groupings emerged: crystal-rich andesites to rhyodacites, and crystal-poor true rhyolites. The rhyolite dikes all have a distinct morphology, and my final work on one of these dikes suggests that the crystal-poor, high viscosity rhyolite dikes develop this morphology through brittle fragmentation from high shear at the margins and viscous flow in the interiors.

From the research presented in this dissertation, several larger themes and conclusions emerge on dike propagation at stratovolcanoes, and dike modeling more generally. The first is that lateral propagation is recorded in the large, silicic dikes, and that this is encouraged both by external stresses

due to topographic loading by an edifice, as well as magmatic factors like buoyancy. This aligns with work by Pinel and Jaupart (2000; 2004) that describes a critical edifice height and overpressure level for which magma of a given critical density will laterally propagate. This may explain why the early-phase basaltic-andesite dikes at Summer Coon have more inclined to vertical fabrics even though compositionally they should be denser and have greater difficultly buoyantly ascending (e.g., Harp & Valentine, 2018). If the edifice of Summer Coon was smaller during the initial magmatic phase, the dikes might not necessarily encounter a large stress barrier to vertical ascent. This leads to the second theme of this research – magmatic properties do influence dike propagation in the shallow sub-surface. While we did not find any correlation between small-scale variations in properties and flow directions, this work shows that larger-scale internal processes can significantly influence magma transport. One such way is through compositionally-controlled density, which is in turn influenced by magmatic water content and volatile exsolution, where low densities and higher porosities promote intrusion into the edifice. Another way is through the development of permeable networks for gas to escape in higher-crystallinity magmas, which regulates magmatic buoyancy and encourages lateral propagation. In crystal-poor magmas, compositionally-controlled viscosity, in tandem with high shear rates during intrusion, promotes outgassing through mechanical fragmentation, and serves as the mechanism modulating lateral propagation.

This work has several important implications for both modeling and conducting fieldwork on dikes. As evidenced throughout this dissertation, dynamic processes occurring within a dike should not be ignored. If propagation is occurring on equivalent timescales as processes like microlite growth, cooling, or exsolution, these processes will actively influence magma buoyancy and/or viscosity. As was shown in the modeling presented in *Chapter 3*, dynamic processes like exsolution and outgassing can significantly impact the stability of dikes in the subsurface. Considering dynamic processes during intrusion may also solve outstanding modeling "problems," like getting magma to enter an edifice, or the volume and overpressure of magma necessary for "large" intrusions, and bring models more in line with physical observations. This work also shows the necessity in fieldwork of higher density sampling along the entire dike length, and sampling away from segmentation, to fully characterize magma flow

and magmatic properties in dikes. An unexpected result from this work were the strong flow fabrics observed in the interiors of Dikes A and S. This implies that even for these large dikes, shear remains high enough in the dike center through to the final pulse of magma for fabrics to develop. This characteristic allows us to track the evolution of magma flow through dikes; by sampling the margins, we can determine the initial propagation direction of the dike, and by sampling the interiors, we can interpret dynamics of magma flow up to final cooling.

While this work answers many questions it set out to address, as with any good research, many questions remain. Further work on flow fabrics across the crystal-rich silicic dikes is necessary to determine if the dikes at Summer Coon propagate more like Dike A (purely lateral) or like Dike S (lateral to inclined/vertical). Preliminary work (e.g., Aksit et al., 2023) suggests purely lateral emplacement for two of the other silicic dikes (H & I), but hints at vertical propagation proximally and lateral propagation medially and distally for Dike G. A greater comparison across the dikes, along with an analysis of the similarities/differences in properties between these dikes, will allow us to speak more broadly about propagation controls, and further support our model for dike stability and lateral propagation. While a broader analysis of magma transport directions at Summer Coon will strengthen our model, further work can be done on our model to address the difference between model opening widths and those observed in the field. Finally, as alluded to in the final chapter, the research on rhyolite propagation is on a single, purely intruded (e.g., closed-system) conduit. To determine if mechanical/shear fragmentation is a possible mechanism of emplacement for the open-system feeder Dike R, comparative microtextural analysis of these dikes would be beneficial. A comparison with other rhyolitic systems, such as the Mono-Inyo dome rhyolites or Glass Mountain flow at Medicine Lake, could help untangle differences between intruded versus erupted rhyolites. But, for now, au revoir Summer Coon. So long, and thanks for all the dikes!

APPENDIX A

Supplementary Material for *Chapter 2: The Dikes Must (Laterally) Flow*

Previously published in the Bulletin of Volcanology

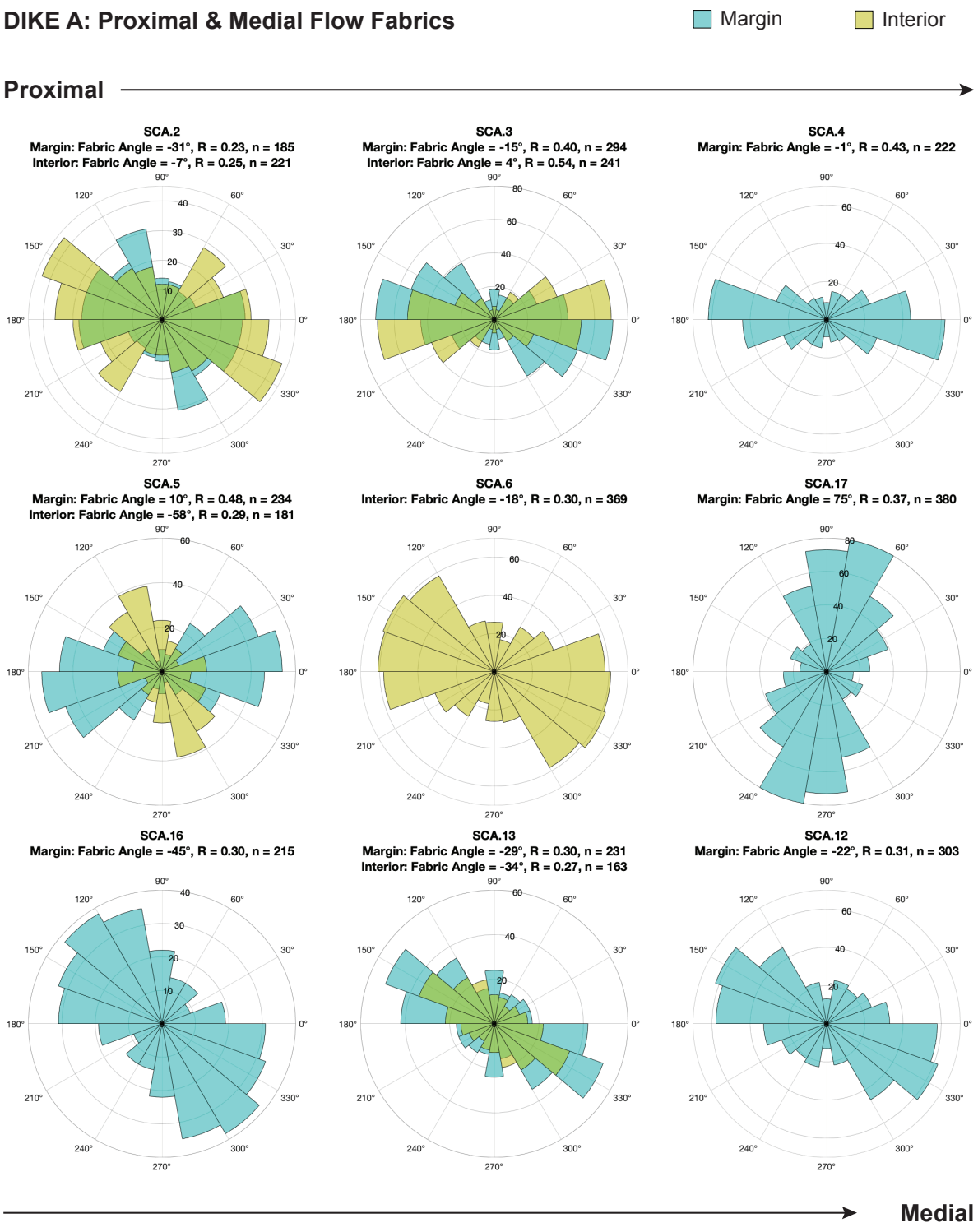

Figure A.1a. Complete, significant flow fabrics for Dike A proximal and medial segments.

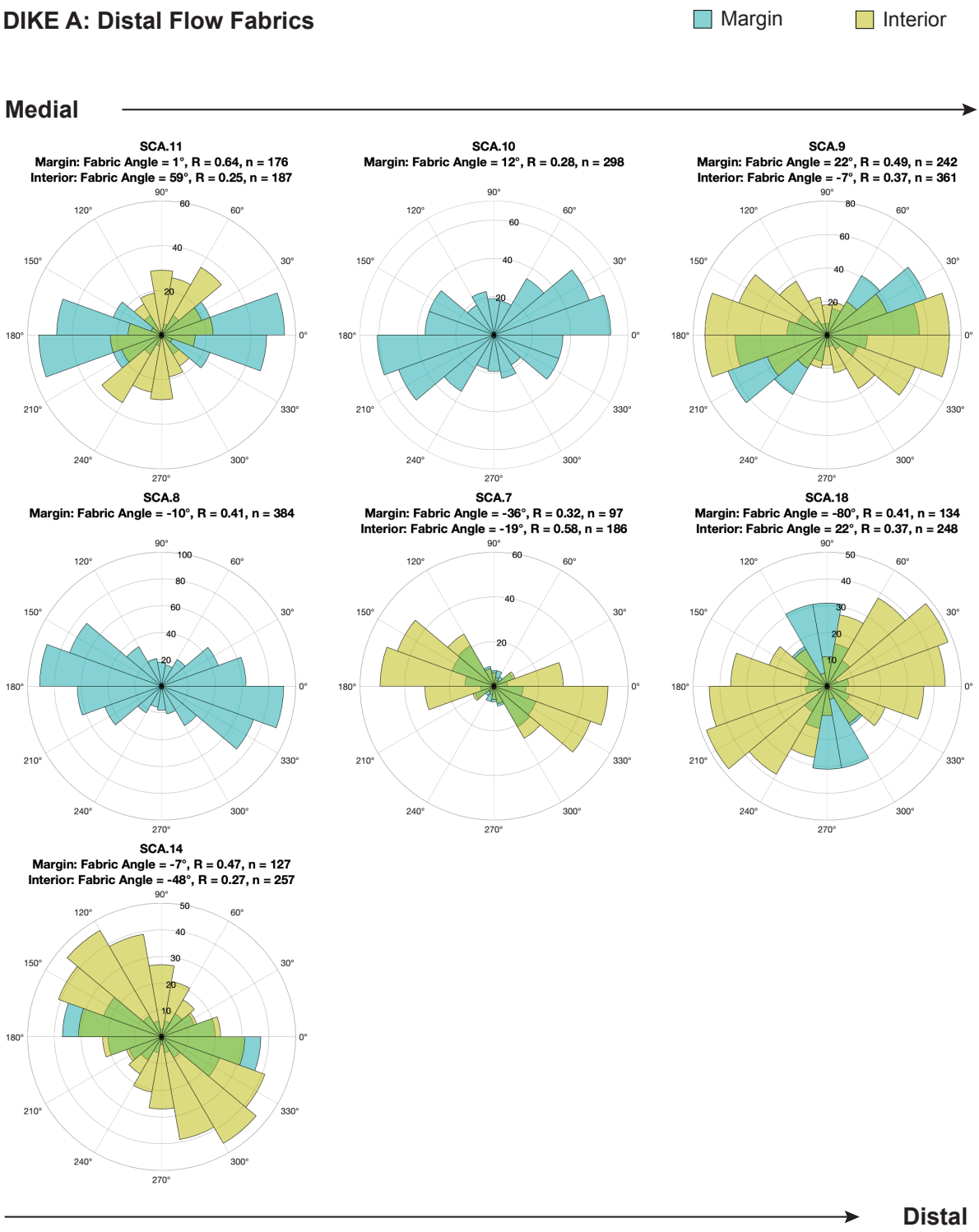

Figure A.1b. Complete, significant flow fabrics for Dike A distal segments.

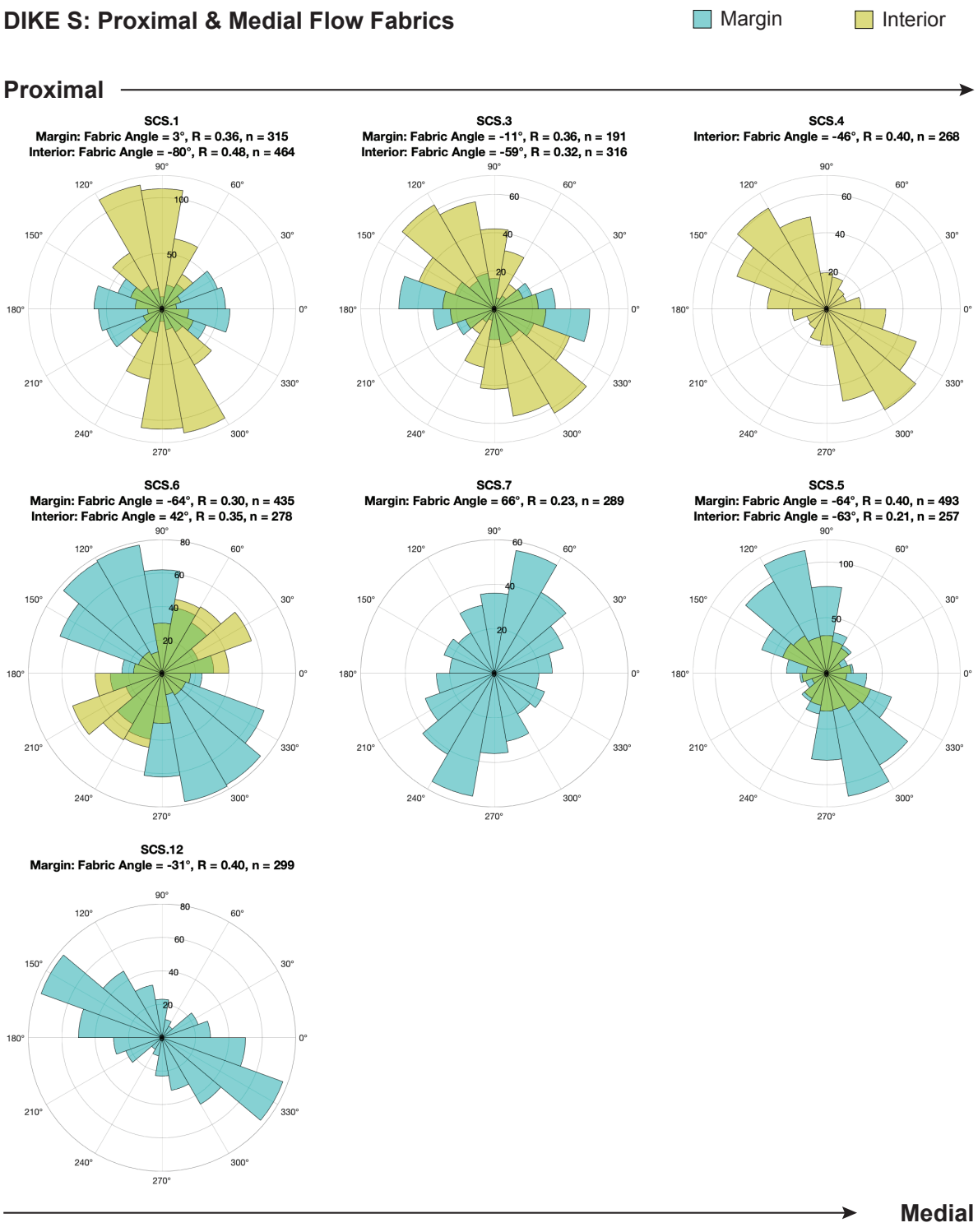

Figure A.2a. Complete significant flow fabrics for Dike S proximal and medial segments.

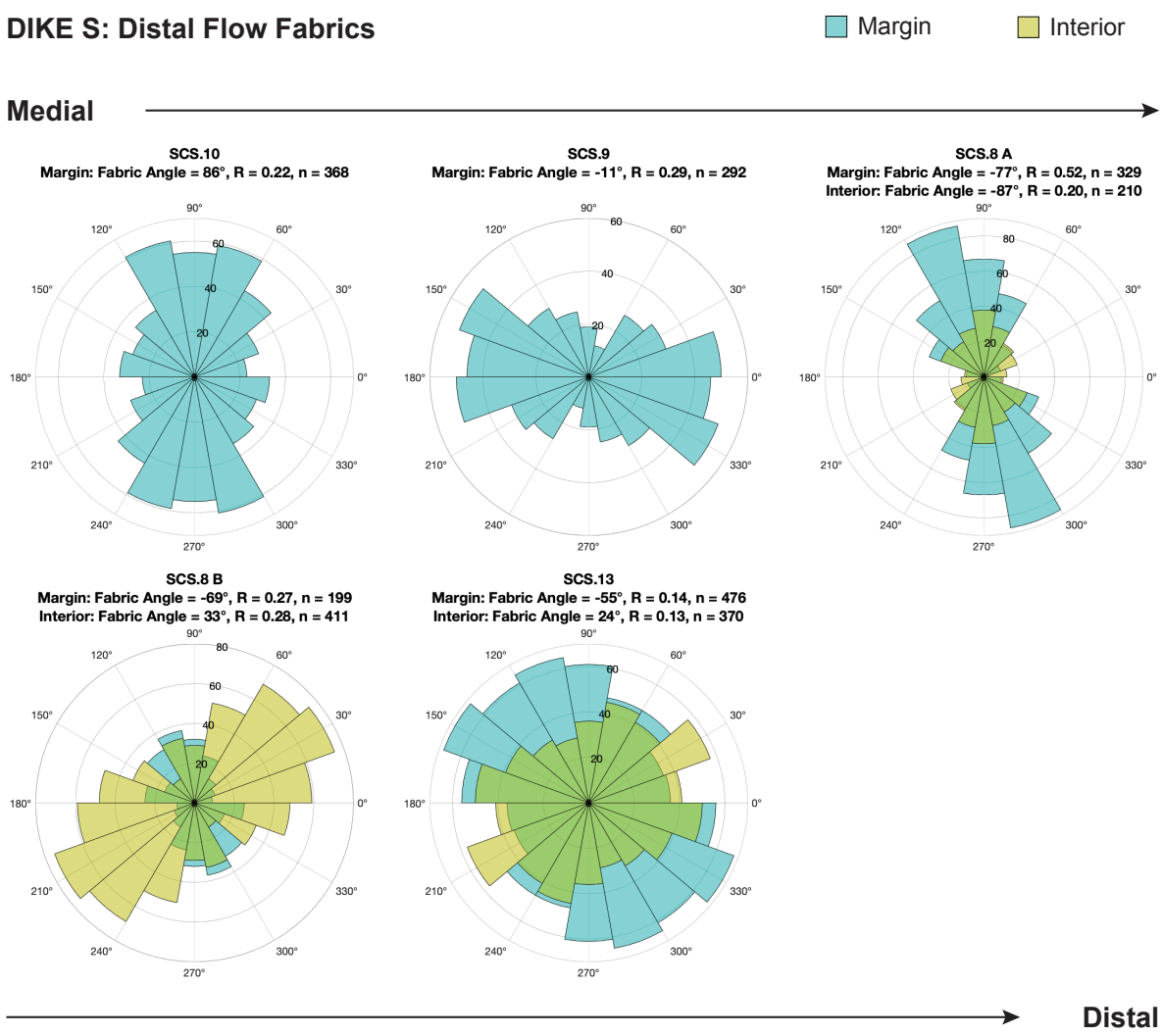

Figure A.2b. Complete flow fabrics for Dike S distal segments. Note that 4 samples (2 interior, 2 margin) were taken at sampling location SCS.8. Location SCS.13 yielded no significant fabric values.

Table A.1a. Complete data collected for Dike A.

Dike A Measurements	Sample ID#	Latitude	Longitude	Normalized Distance from Dike Start	Moats (1990) Closest Thickness	Dike Thickness (m)	Fabric Angle (°)	Fabric Number of Crystals (*n*)	Fabric *R-value*
Margin									
Proximal	**SCA.2-1**	37.797956	-106.372754	0.10	15.50	29.5	149	185	0.23
	SCA.3-1	37.799985	-106.373623	0.14	15.50	26.9	165	294	0.40
	SCA.4-1	37.803412	-106.375616	0.20	10.10	25.5	179	222	0.43
	SCA.5-1	37.804678	-106.375631	0.22	7.00	21.1	10	234	0.48
Medial	**SCA.6-1**	37.80957	-106.375185	0.30	13.70	25.8	117	183	0.14
	SCA.17-1	37.812095	-106.376606	0.35	40.50	33.6	75	380	0.37
	SCA.16-1	37.819361	-106.379736	0.49	16.20	56.7	135	215	0.30
	SCA.13.1	37.821353	-106.379808	0.52	44.80	30.2	151	231	0.30
	SCA.12-1	37.821461	-106.380139	0.52	44.80	25.2	158	303	0.31
Distal	**SCA.11-1**	37.823886	-106.380929	0.57	46.60	31	1	176	0.64
	SCA.10-1	37.825818	-106.381414	0.60	52.70	41.2	12	298	0.28
	SCA.9-1	37.827516	-106.382159	0.63	48.80	43	22	242	0.49
	SCA.8-1	37.828279	-106.382355	0.65	48.80	39	170	384	0.41
	SCA.7-3	37.828757	-106.382669	0.65	48.80	38	144	97	0.32
	SCA.18-1	37.834349	-106.387168	0.77	63.10	42.7	100	134	0.41
	SCA.14-3	37.837524	-106.388849	0.83	50.90	55.2	173	127	0.47
Interior									
Proximal	**SCA.2-2**	37.797972	-106.37284	0.10			173	221	0.25
	SCA.3-2	37.800004	-106.373667	0.14			4	241	0.54
	SCA.5-2	37.804654	-106.375609	0.22			122	181	0.29
Medial	**SCA.6-2**	37.809946	-106.375195	0.31			162	369	0.30
	SCA.13-4	37.821191	-106.380001	0.52			146	163	0.27
Distal	**SCA.11-2**	37.823874	-106.380914	0.57			60	305	0.25
	SCA.9-3	37.827517	-106.382056	0.63			173	361	0.37
	SCA.7-2	37.82876	-106.382634	0.65			161	186	0.58
	SCA.18-2	37.834331	-106.386019	0.76			22	248	0.37
	SCA.14-1	37.837149	-106.389178	0.82			132	257	0.27

Table A.1b. Complete data collected for Dike A continued.

Dike A Measurements	Sample ID#	Mean Fabric Angle (°) (segment)	Mean Fabric *R-value*	Total Porosity (%)	Error in Porosity (% of total)	Bulk density (kg/m^3)	Solid density (kg/m^3)
Margin		**167**	**0.57**				
Proximal	**SCA.2-1**	171	0.86	7.98	4.59	2401	2609
	SCA.3-1			15.57	3.41	2218	2627
	SCA.4-1			10.35	1.03	2456	2740
	SCA.5-1			4.72	2.84	2524	2650
Medial	**SCA.6-1**	141	0.52	4.65	1.41	2556	2681
	SCA.17-1			3.24	3.37	2569	2655
	SCA.16-1			0.63	22.21	2591	2608
	SCA.13.1			8.13	1.12	2481	2701
	SCA.12-1			8.70	4.10	2422	2653
Distal	**SCA.11-1**	175	0.57	9.65	8.42	2422	2673
	SCA.10-1			8.02	2.08	2422	2634
	SCA.9-1			8.64	4.39	2411	2639
	SCA.8-1			2.88	3.04	2538	2613
	SCA.7-3			8.27	2.11	2452	2673
	SCA.18-1			1.48	2.44	2567	2605
	SCA.14-3			1.95	5.61	2557	2608
Interior		**164**	**0.53**				
Proximal	**SCA.2-2**	163	0.60	3.23	1.47	2540	2625
	SCA.3-2			6.53	0.74	2483	2657
	SCA.5-2			10.37	2.68	2352	2624
Medial	**SCA.6-2**	154	0.96	9.99	1.04	2527	2807
	SCA.13-4			12.70	0.66	2351	2693
Distal	**SCA.11-2**	176	0.38	6.27	1.13	2544	2714
	SCA.9-3			3.83	1.00	2575	2677
	SCA.7-2			4.07	5.10	2578	2688
	SCA.18-2			6.53	1.58	2510	2686
	SCA.14-1			7.02	1.19	2473	2660

Table A.2a. Complete data collected for Dike S.

Dike S Measurements	Sample ID#	Latitude	Longitude	Normalized Distance from Dike Start	Moats (1990) Closest Thickness	Dike Thickness (m)	Fabric Angle (°)	Fabric Number of Crystals (*n*)	Fabric *R-value*
Proximal Margin	**SCS.1-3**	37.773951	-106.393448	0.02	5.90	11.5	3	315	0.36
	SCS.2-3	37.773694	-106.395086	0.06	6.10	13.2	156	315	0.12
	SCS.3-1	37.77325	-106.397729	0.14	6.90	12	169	191	0.36
	SCS.4-4	37.772457	-106.401822	0.25	13.10	16	100	234	0.11
Medial Margin	**SCS.6-1**	37.772163	-106.406315	0.38	15.20	20.1	116	435	0.30
	SCS.7-1	37.771444	-106.408990	0.45	29.00	29.7	66	289	0.23
	SCS.5-3	37.770709	-106.412432	0.55	35.10	21.7	116	493	0.40
	SCU.4-1	37.770981	-106.413609	0.58	35.1	32.2	19	256	0.05
	SCS.12-1	37.770006	-106.415214	0.63	36.60	38	149	299	0.40
Distal Margin	**SCS.11-1**	37.769586	-106.416396	0.66	38.10	34.6	62	356	0.14
	SCS.10-1	37.76923	-106.418824	0.73	33.50	74.5	86	368	0.22
	SCS.9-1	37.767769	-106.421092	0.80	82.30	81	169	292	0.29
	SCS.8-6	37.767255	-106.423222	0.86	109.70	72.2	103	329	0.52
	SCS.8-7	37.767121	-106.423395	0.87	109.70	72.2	111	199	0.27
	SCS.13-1	37.76668	-106.427176	0.97	114.30	52.4	125	476	0.14
Proximal Interior	**SCS.1-1**	37.773958	-106.393405	0.02			100	464	0.48
	SCS.2-1	37.773665	-106.395114	0.07			168	305	0.13
	SCS.3-2	37.773269	-106.397731	0.14			121	316	0.32
	SCS.4-2	37.772448	-106.401704	0.25			134	268	0.40
Medial Interior	**SCS.6-3**	37.772061	-106.406376	0.38			42	371	0.35
	SCS.5-2	37.770652	-106.412297	0.55			117	257	0.21
	SCS.12-3	37.769821	-106.415184	0.63			130	307	0.07
Distal Interior	**SCS.10-3**	37.769042	-106.41876	0.73			-	-	-
	SCS.8-3	37.767396	-106.423379	0.87			93	210	0.20
	SCS.8-1	37.767566	-106.423469	0.87			33	411	0.28
	SCS.13-2	37.766783	-106.428225	1.00			24	370	0.13

Table A.2b. Complete data collected for Dike S continued.

Dike S Measurements	Sample ID#	Mean Fabric Angle (°) (segment)	Mean Fabric *R-value*	Total Porosity (%)	Error in Porosity (% of total)	Bulk density (kg/m^3)	Solid density (kg/m^3)
Proximal Margin	**SCS.1-3**	176	0.97	4.64	4.45	2475	2595
	SCS.2-3			4.09	1.28	2488	2594
	SCS.3-1			4.75	0.82	2482	2606
	SCS.4-4			8.46	0.66	2431	2656
Medial Margin	**SCS.6-1**	115	0.56	7.28	0.47	2418	2608
	SCS.7-1			7.81	0.72	2387	2589
	SCS.5-3			7.82	1.25	2393	2596
	SCU.4-1			2.33	0.58	2520	2580
	SCS.12-1			5.69	1.20	2427	2574
Distal Margin	**SCS.11-1**	109	0.54	6.91	2.77	2416	2595
	SCS.10-1			9.05	3.55	2354	2588
	SCS.9-1			3.99	2.83	2472	2575
	SCS.8-6			2.39	4.17	2522	2584
	SCS.8-7			-			
	SCS.13-1			4.38	2.42	2457	2569
Proximal Interior	**SCS.1-1**	118	0.88	5.70	1.07	2432	2579
	SCS.2-1			4.85	0.50	2508	2636
	SCS.3-2			8.16	0.45	2444	2662
	SCS.4-2			8.71	1.69	2433	2665
Medial Interior	**SCS.6-3**	80	0.26	9.24	0.95	2428	2676
	SCS.5-2			6.11	0.96	2506	2669
	SCS.12-3			11.36	1.00	2298	2592
Distal Interior	**SCS.10-3**	63	0.50	9.34	2.92	2267	2500
	SCS.8-3			1.08	7.36	2517	2544
	SCS.8-1			4.41	1.72	2463	2577
	SCS.13-2			7.16	1.65	2395	2580

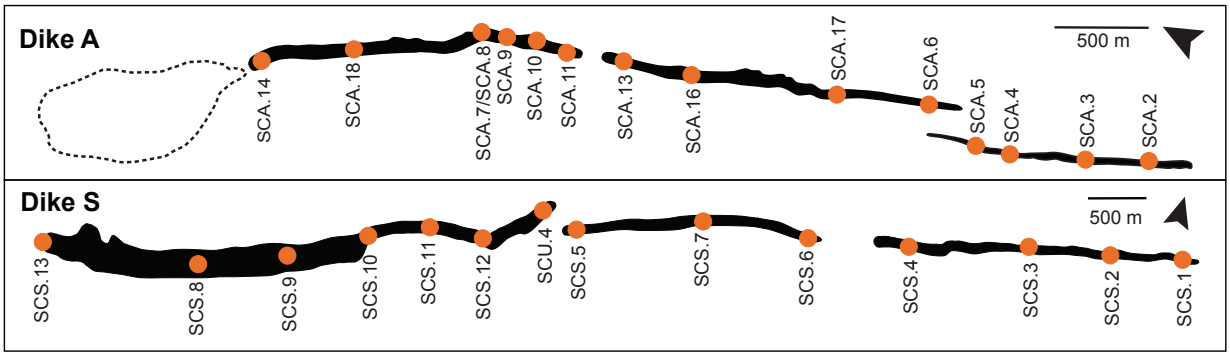

Figure A.3. Sampling site locations presented in this paper for Dikes A and S with sample identification numbers labeled. Refer to Supplemental Material Tables 1 and 2 for GPS coordinates and data collected at each location

Table A.3. Complete normalized bulk rock geochemistry results for Dike A and Dike S.

Dike A Normalized Bulk Rock Geochemistry:

	Margin-Proximal	*Interior-Proximal*	*Margin-Medial*	*Distal-Margin*	*Distal-Interior*	*Distal-Interior*
	SCA.2-3	**SCA.2-2**	**SCA.7-3**	**SCA.14-3**	**SCA.14-1**	**SCA.14-2**
SiO2	64.9599534	65.608471	65.4620684	64.6954706	64.9962759	65.3459694
TiO2	0.62025079	0.63559041	0.629349	0.64092712	0.64783024	0.63361999
Al2O3	15.7214152	15.6669518	15.4180116	15.8184925	15.5317779	15.4926239
FeO*	3.95325532	4.4284326	4.70619765	4.5613003	4.6618748	4.49757223
MnO	0.05918125	0.04966028	0.05429916	0.08234239	0.05762752	0.06364441
MgO	1.98623656	2.24266644	1.89188669	2.32635068	2.21437035	2.28070919
CaO	4.86742876	3.63651938	3.75865532	4.10622881	3.65778335	3.74382468
Na2O	3.61374963	3.78978303	3.87630519	3.99620146	3.92684635	3.99487214
K2O	3.97360256	3.69138022	3.94293014	3.52260548	4.04623927	3.69117431
P2O5	0.24492653	0.25054478	0.26029691	0.25008066	0.25937431	0.25598974
Total	100	100	100	100	100	100

Dike S Normalized Bulk Rock Geochemistry:

	Interior-Proximal	*Margin-Proximal*	*Margin-Medial*	*Margin-Distal*	*Interior-Distal*
	SCS.2-1	**SCS.3-4**	**SCU.4-3**	**SCS.8-1**	**SCS.8-3**
SiO2	69.6563282	68.2932905	69.489836	69.4930524	70.337053
TiO2	0.36395706	0.3586587	0.36130736	0.39010213	0.33431916
Al2O3	15.863594	16.4631773	15.5926549	15.434306	15.3246017
FeO*	2.41875637	2.71627865	2.78766012	3.17305738	2.68717847
MnO	0.03515721	0.05861597	0.04988763	0.02637933	0.03051917
MgO	0.56990642	0.73278446	0.67524667	0.64918354	0.56485324
CaO	2.24956228	2.5411462	2.42443788	2.27049076	2.16954544
Na2O	4.20598132	4.47925281	4.3148262	4.22820708	4.29574769
K2O	4.4799479	4.18849367	4.13865737	4.18217007	4.12674901
P2O5	0.15680916	0.16830171	0.16548582	0.15305134	0.12943311
Total	100	100	100	100	100

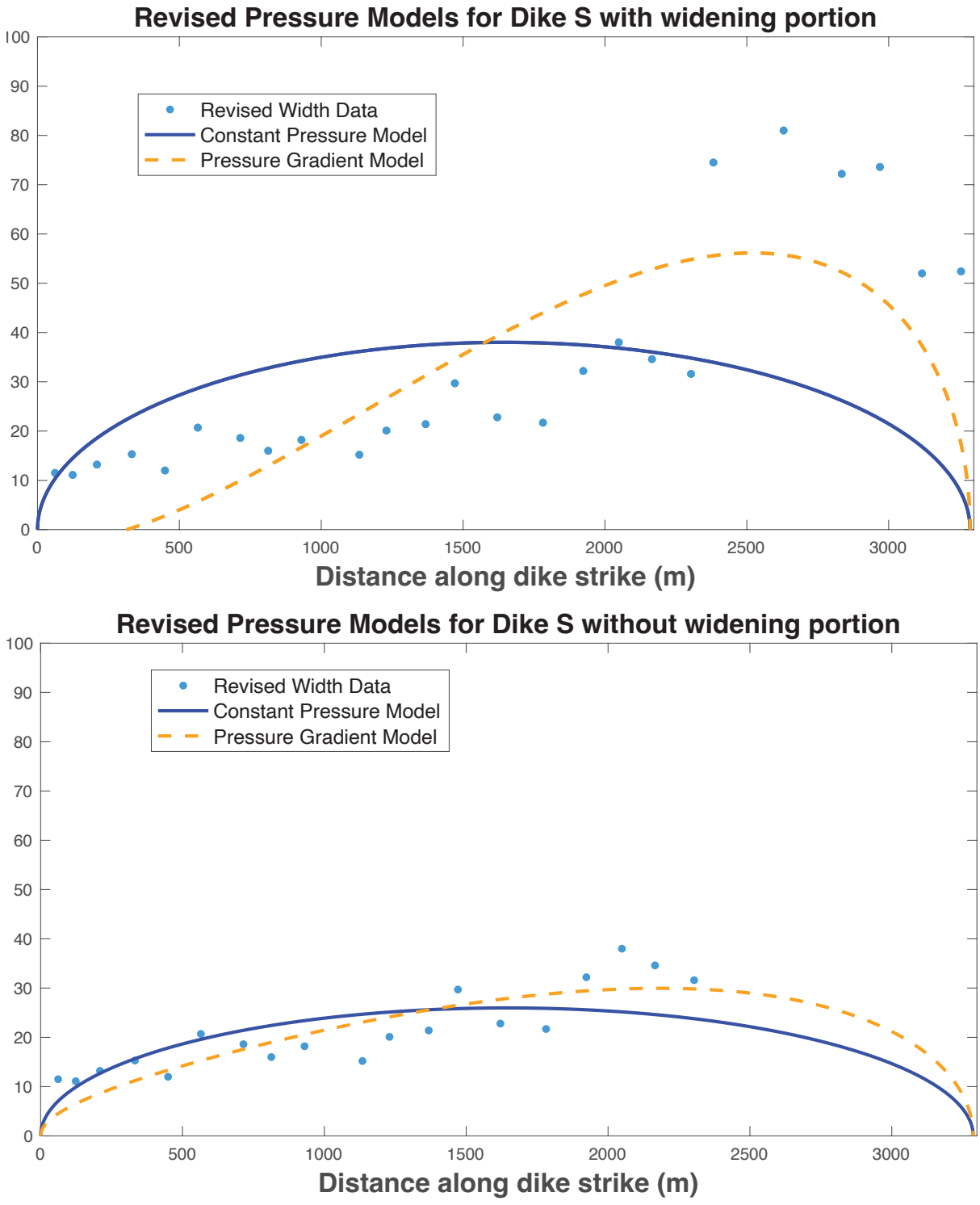

Figure A.4. Pressure models calculated for Dike S including and excluding the distal widening portion. After Poland et al. (2008) revised for updated Google Earth and ground measurements of dike widths.

APPENDIX B

Supplementary Material for *Chapter 3: Mostly Gasless*

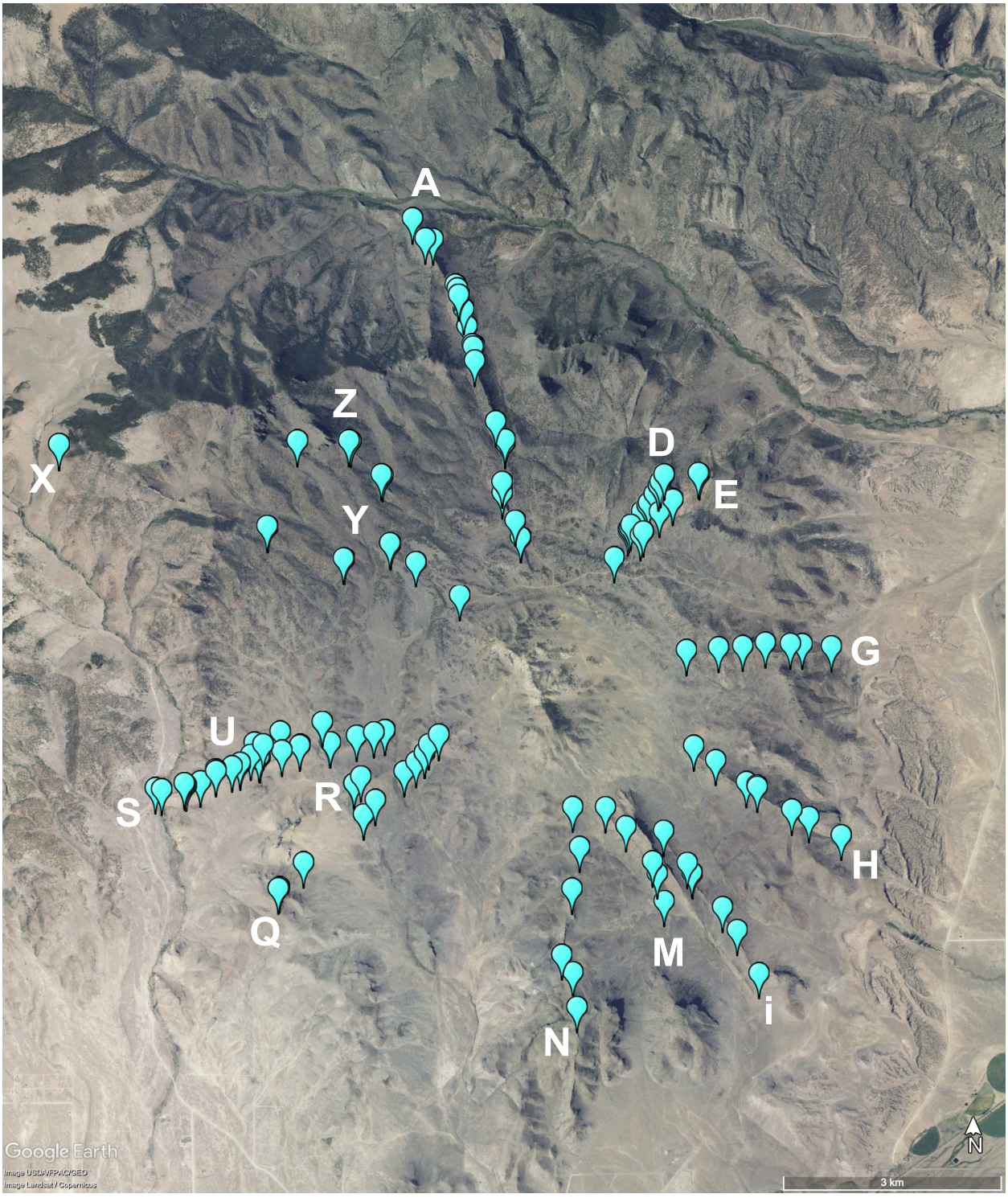

Figure B.1. Google Earth image of sampling locations for the porosity analysis presented in *Chapter 3* (Google, n.d.). Labels at the end of each dike correspond to the naming system used in this study.

Table B.1. Table of values for normalized bulk rock geochemistry for samples from each of the dikes presented in *Chapter 3*. Values are for normalized major elements in wt.%, on a volatile-free basis. Total iron is expressed as FeO.

	SiO_2	TiO_2	Al_2O_3	FeO	MnO	MgO	CaO	Na_2O	K_2O	P_2O_5
SCA.2-3	64.96	0.62	15.72	3.95	0.06	1.99	4.87	3.61	3.97	0.24
SCA.2-2	65.61	0.64	15.67	4.43	0.05	2.24	3.64	3.79	3.69	0.25
SCA.7-3	65.46	0.63	15.42	4.71	0.05	1.89	3.76	3.88	3.94	0.26
SCA.14-2	65.35	0.63	15.49	4.50	0.06	2.28	3.74	3.99	3.69	0.26
SCA.14-3	64.70	0.64	15.82	4.56	0.08	2.33	4.11	4.00	3.52	0.25
SCA.14-1	65.00	0.65	15.53	4.66	0.06	2.21	3.66	3.93	4.05	0.26
SCD.3-2	72.64	0.17	15.06	1.21	0.05	0.22	1.09	4.49	5.02	0.04
SCD.7-1	74.79	0.22	13.53	1.31	0.07	0.45	1.11	3.59	4.85	0.08
SCE.1-1	71.75	0.19	15.18	1.59	0.08	0.34	1.15	4.03	5.64	0.06
SCE.5-1	71.59	0.20	15.49	1.50	0.08	0.39	1.44	4.52	4.70	0.08
SCG.1-1	60.59	0.84	15.68	6.08	0.10	3.96	5.37	3.38	3.65	0.35
SCG.7-1	63.50	0.69	15.53	5.16	0.09	2.96	4.35	3.89	3.57	0.27
SCH.1-1	65.60	0.65	15.68	4.62	0.06	1.65	3.73	3.99	3.75	0.27
SCH.3-1	66.53	0.64	15.13	4.67	0.05	1.82	3.56	3.82	3.52	0.25
SCi.1-1	65.98	0.54	16.15	3.89	0.08	1.56	3.62	3.84	4.09	0.25
SCi.7-1	69.14	0.52	15.76	3.22	0.02	0.35	2.81	4.01	3.94	0.22
SCM.1-1	69.83	0.37	16.21	2.02	0.02	0.61	2.23	4.16	4.41	0.15
SCM.5-1	68.91	0.36	15.99	3.24	0.04	0.52	1.95	4.25	4.53	0.20
SCN.1-1	66.10	0.60	15.43	4.27	0.07	1.95	3.82	4.12	3.41	0.24
SCN.6-1	62.25	0.81	16.74	5.61	0.08	2.58	4.98	3.91	2.76	0.29
SCQ.1-1	67.03	0.52	15.91	3.49	0.06	1.42	3.28	3.62	4.46	0.20
SCQ.8-1	68.12	0.46	15.70	3.16	0.06	1.14	2.88	3.73	4.57	0.18
SCR.1-1	71.98	0.26	15.05	1.67	0.07	0.42	1.40	4.03	5.03	0.09
SC-01-11 (R)	72.66	0.19	15.11	1.13	0.04	0.24	1.25	4.41	4.91	0.06
SCS.2-1	69.66	0.36	15.86	2.42	0.04	0.57	2.25	4.21	4.48	0.16
SCS.3-4	68.29	0.36	16.46	2.72	0.06	0.73	2.54	4.48	4.19	0.17
SCU.4-3	69.49	0.36	15.59	2.79	0.05	0.68	2.42	4.31	4.14	0.17
SCS.8-1	69.49	0.39	15.43	3.17	0.03	0.65	2.27	4.23	4.18	0.15
SCS.8-3	70.34	0.33	15.32	2.69	0.03	0.56	2.17	4.30	4.13	0.13
SCU.3-3	67.16	0.55	15.18	4.25	0.06	1.69	3.40	4.06	3.40	0.23
SCU.5-1	59.97	1.15	15.29	8.69	0.11	4.14	4.95	3.05	2.21	0.46
SCX.1-2	67.40	0.70	15.69	3.49	0.04	1.07	3.77	3.88	3.70	0.27
SCX.2-2	64.35	0.71	15.57	5.04	0.06	2.63	3.50	3.76	4.11	0.27
SCY.2-1	54.81	1.34	16.26	8.54	0.13	5.84	6.71	2.96	2.78	0.62
SCZ.3-1	68.64	0.38	15.87	2.99	0.07	0.90	2.43	4.31	4.25	0.15

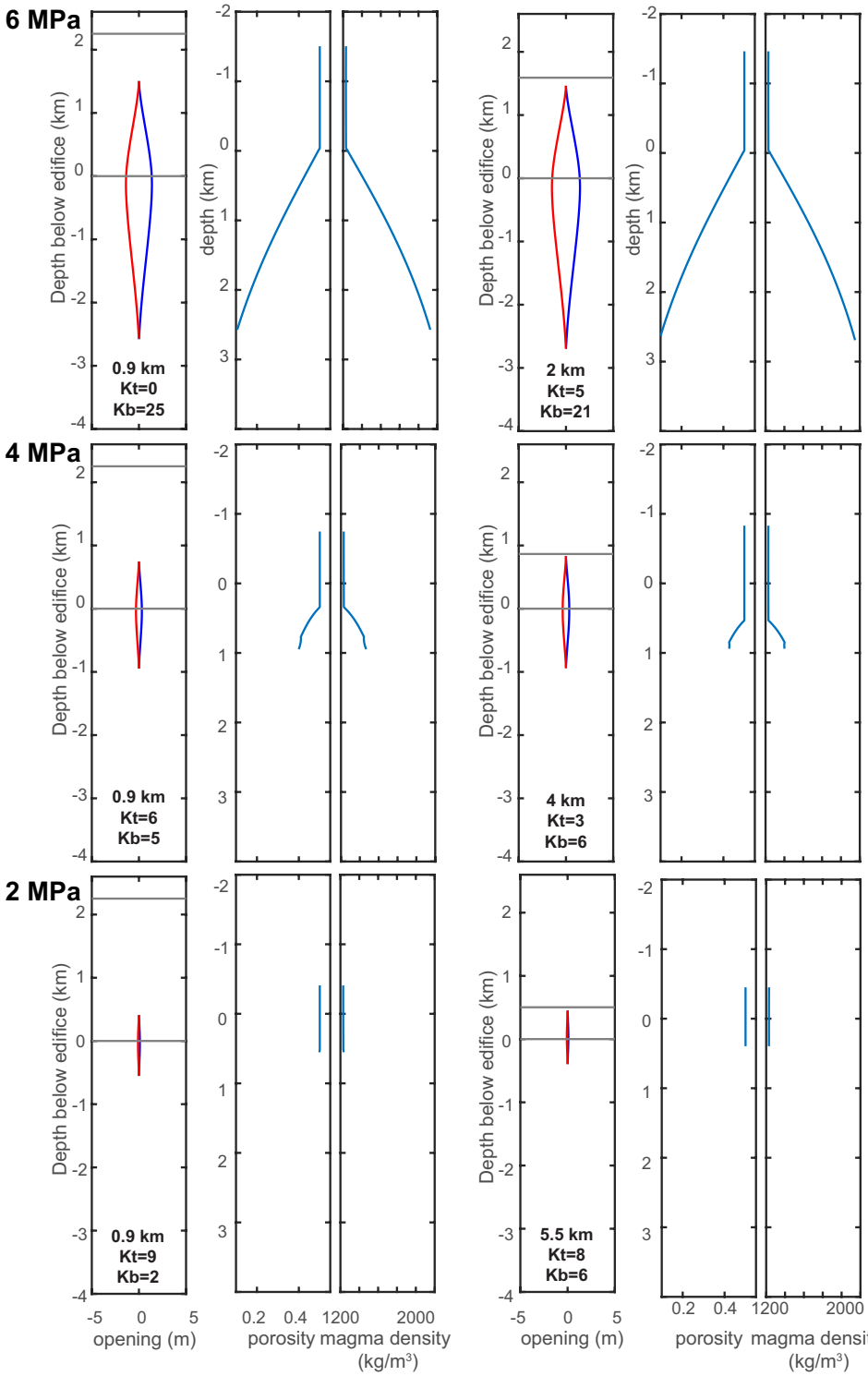

Figure B.2a. Dike opening profiles modeled for a trachytic composition magma with 4 wt.% H_2O and a 50% porosity threshold. Porosity and density variations are plotted as a function of dike height. Profiles are presented for 6 MPa, 4 MPa and 2 MPa overpressures, both proximally (left column) and distally (right column).

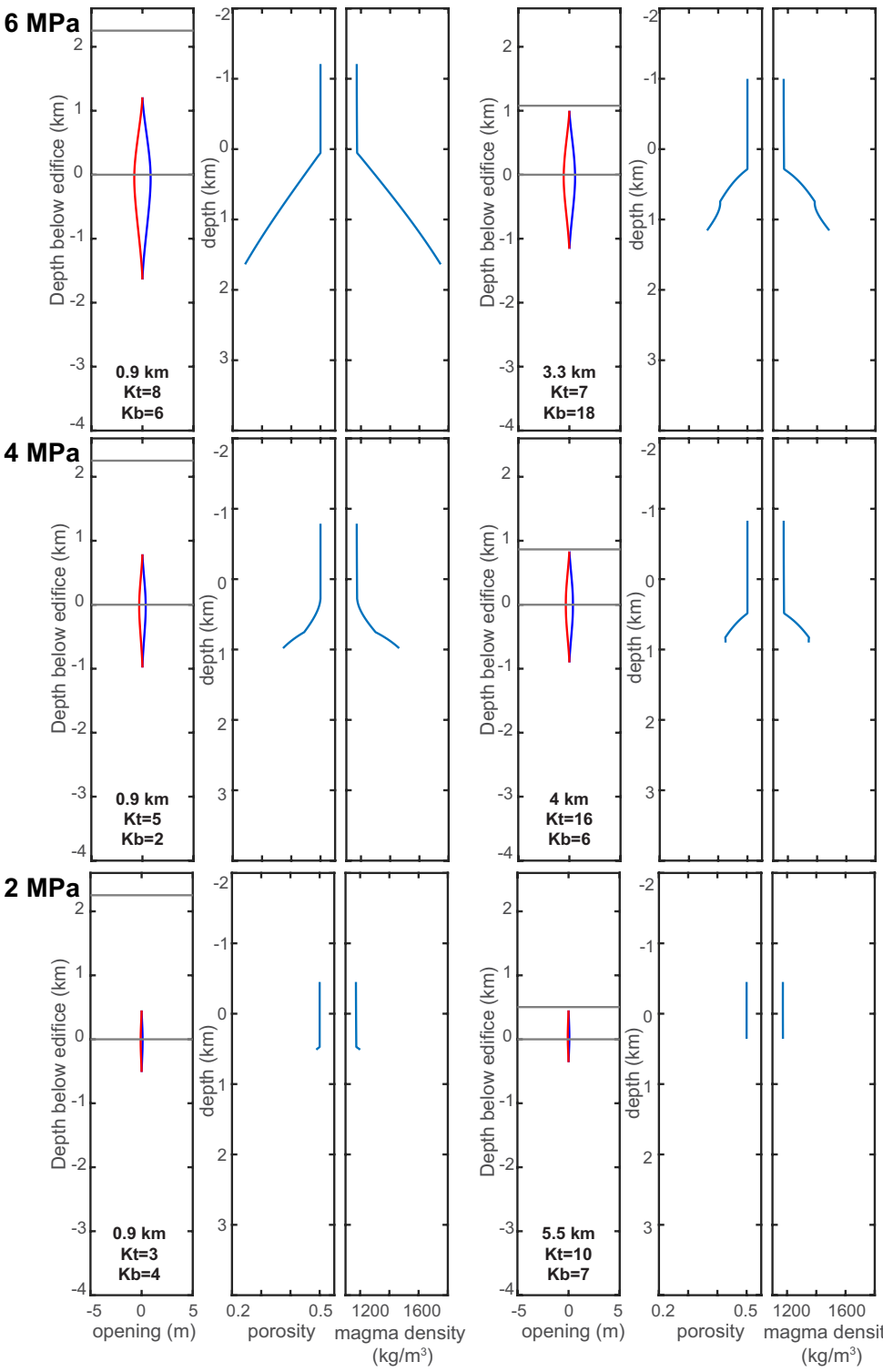

Figure B.2b. Dike opening profiles modeled for a rhyolitic composition magma with 4 wt.% H_2O and a 50% porosity threshold. Porosity and density variations are plotted as a function of dike height. Profiles are presented for 6 MPa, 4 MPa and 2 MPa overpressures, both proximally (left column) and distally (right column).

APPENDIX C

Supplementary Material for *Chapter 4: How to Emplace your Rhyolite*

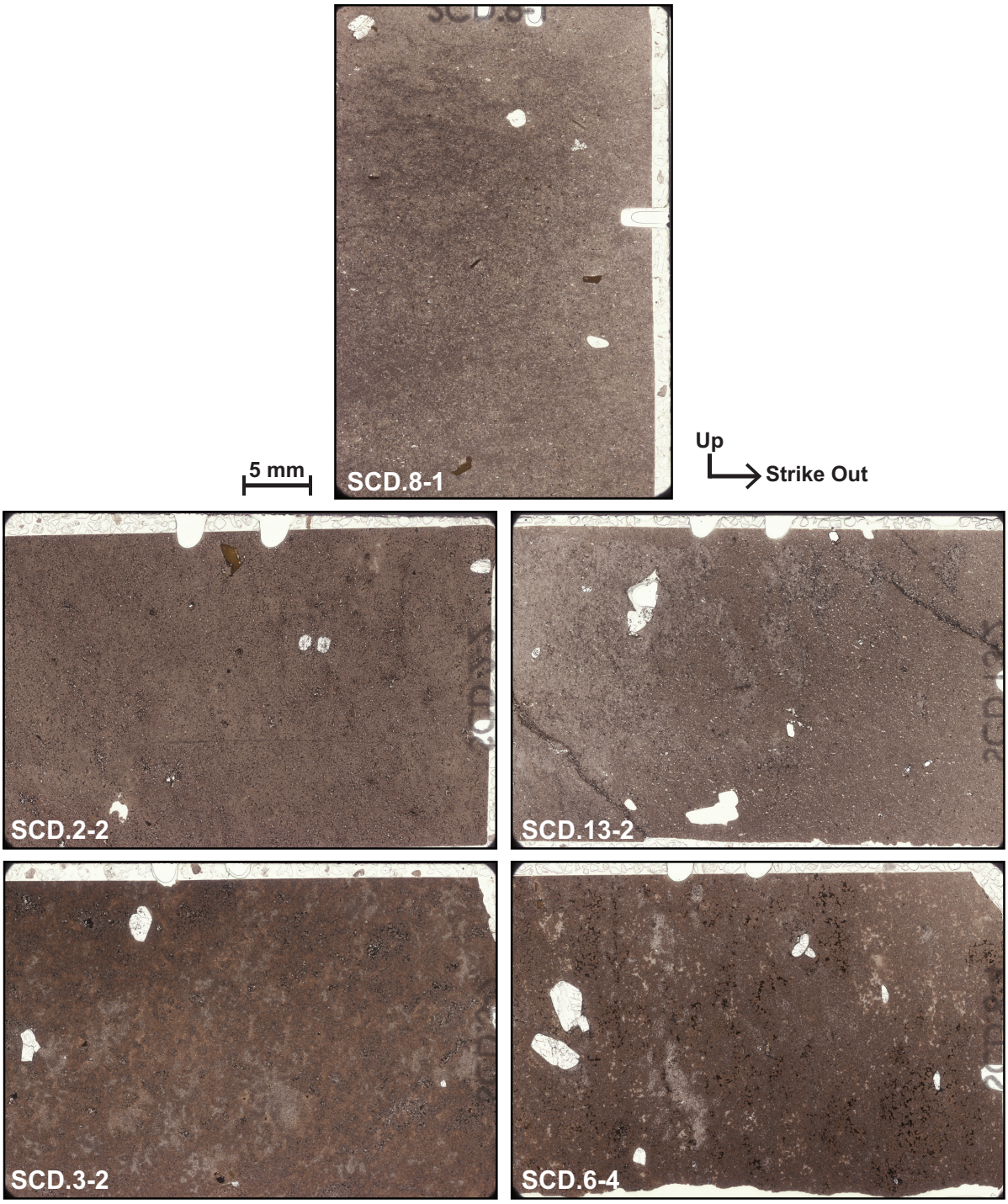

Figure C.1. Plain light thin section images from the platy interior. Thin sections are ordered from proximal at the top to distal at the bottom, corresponding to sampling sites in Figure 4.2. All thin sections are in the same scale and oriented per the notation, with the top of the page being vertical up, and the right side of the page being stike of the dike out from the central intrusive complex.

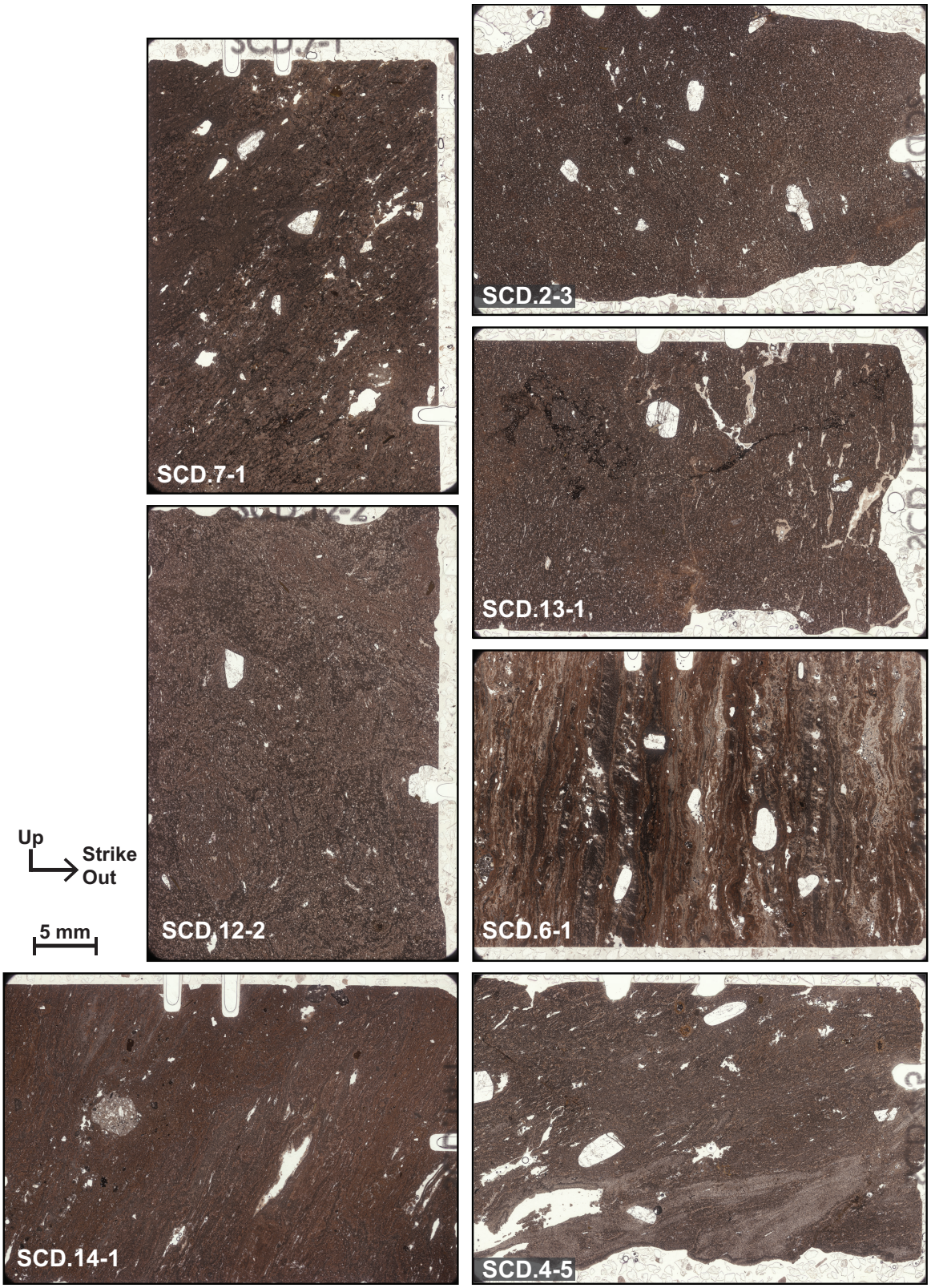

Figure C.2. Plain light thin section images from the glassy flow-banded interior. Thin sections are ordered from proximal at the top to distal at the bottom, corresponding to sampling sites in Figure 4.2. All thin sections are in the same scale and oriented per the notation.

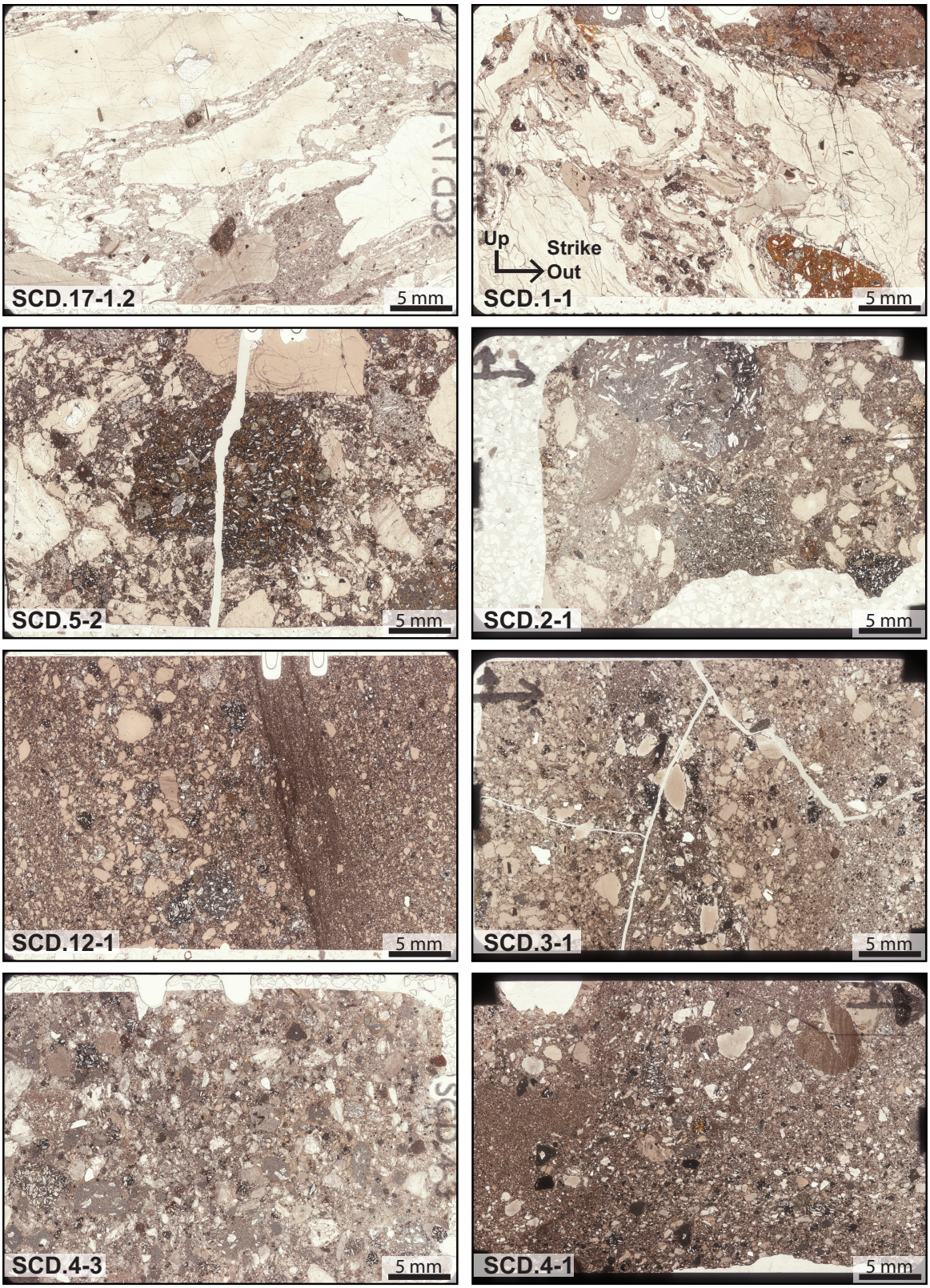

Figure C.3. Plain light thin section images from the brecciated margins. Thin sections are ordered from proximal at the top to distal at the bottom, corresponding to sampling sites in Figure 4.2. All thin sections but SCD.17-1.2 are oriented with vertical being up and the right of the page being strike of dike out from the CIC.



REFERENCES

CHAPTER ONE

Acocella, V., Behncke, B., Neri, M., & D'Amico, S. (2003). Link between major flank slip and 2002–2003 eruption at Mt. Etna (Italy). *Geophysical Research Letters*, 30(24). https://doi.org/10.1029/2003GL018642

Albino, F., Biggs, J., & Syahbana, D. K. (2019). Dyke intrusion between neighbouring arc volcanoes responsible for 2017 pre-eruptive seismic swarm at Agung. *Nature Communications*, 10(1), 748. https://doi.org/10.1038/s41467-019-08564-9

Castro, J. M., Cordonnier, B., Tuffen, H., Tobin, M. J., Puskar, L., Martin, M. C., & Bechtel, H. A. (2012). The role of melt-fracture degassing in defusing explosive rhyolite eruptions at volcán Chaitén. *Earth and Planetary Science Letters*, 333–334, 63–69. https://doi.org/10.1016/j.epsl.2012.04.024

Castro, J. M., Schipper, C. I., Mueller, S. P., Militzer, A. S., Amigo, A., Parejas, C. S., & Jacob, D. (2013). Storage and eruption of near-liquidus rhyolite magma at Cordón Caulle, Chile. *Bulletin of Volcanology*, 75(4), 702. https://doi.org/10.1007/s00445-013-0702-9

Donnelly-Nolan, J. M., Grove, T. L., Lanphere, M. A., Champion, D. E., & Ramsey, D. W. (2008). Eruptive history and tectonic setting of Medicine Lake Volcano, a large rear-arc volcano in the southern Cascades. *Journal of Volcanology and Geothermal Research*, 177(2), 313–328. https://doi.org/10.1016/j.jvolgeores.2008.04.023

Farquharson, J. I., Tuffen, H., Wadsworth, F. B., Castro, J. M., Unwin, H., & Schipper, C. I. (2022). In-conduit capture of sub-micron volcanic ash particles via turbophoresis and sintering. *Nature Communications*, 13(1), 4713. https://doi.org/10.1038/s41467-022-32522-7

Foster, A., Wadsworth, F. B., Tuffen, H., Unwin, H. E., & Humphreys, M. C. S. (2024). Evidence for the formation of silicic lava by pyroclast sintering. *Nature Communications*, 15(1), 5347. https://doi.org/10.1038/s41467-024-49601-6

Gardner, J. E., Llewellin, E. W., Watkins, J. M., & Befus, K. S. (2017). Formation of obsidian pyroclasts by sintering of ash particles in the volcanic conduit. *Earth and Planetary Science Letters*, 459, 252–263. https://doi.org/10.1016/j.epsl.2016.11.037

Gonnermann, H. M., & Manga, M. (2003). Explosive volcanism may not be an inevitable consequence of magma fragmentation. *Nature*, 426(6965), 432–435. https://doi.org/10.1038/nature02138

Hotta, K., Iguchi, M., & Tameguri, T. (2016). Rapid dike intrusion into Sakurajima volcano on August 15, 2015, as detected by multi-parameter ground deformation observations. *Earth, Planets and Space*, 68(1), 68. https://doi.org/10.1186/s40623-016-0450-0

Lara, L. E. (2009). The 2008 eruption of the Chaitén Volcano, Chile: A preliminary report. *Andean Geology*, 36(1). https://doi.org/10.4067/S0718-71062009000100009

Liu, Y., Zhang, Y., & Behrens, H. (2005). Solubility of H2O in rhyolitic melts at low pressures and a new empirical model for mixed H2O–CO2 solubility in rhyolitic melts. *Journal of Volcanology and Geothermal Research*, 143(1–3), 219–235. https://doi.org/10.1016/j.jvolgeores.2004.09.019

Poland, M. P., Fink, J. H., & Tauxe, L. (2004). Patterns of magma flow in segmented silicic dikes at Summer Coon volcano, Colorado: AMS and thin section analysis. *Earth and Planetary Science Letters*, 219(1–2), 155–169. https://doi.org/10.1016/S0012-821X(03)00706-4

Rust, A. C., Cashman, K. V., & Wallace, P. J. (2004). Magma degassing buffered by vapor flow through brecciated conduit margins. *Geology*, 32(4), 349. https://doi.org/10.1130/G20388.2

Schipper, C. I., Castro, J. M., Tuffen, H., James, M. R., & How, P. (2013). Shallow vent architecture during hybrid explosive–effusive activity at Cordón Caulle (Chile, 2011–12): Evidence from direct observations and pyroclast textures. *Journal of Volcanology and Geothermal Research*, 262, 25–37. https://doi.org/10.1016/j.jvolgeores.2013.06.005

Scholz, K. J. (2025). *Magmatic Processes Throughout the Crust: Deep Long-Period Earthquakes, Magma Chamber Evolution, and Topographic Influences on Shallow Dike Transport.* (Doctoral dissertation, University of Oregon).

Sieh, K., & Bursik, M. (1986). Most recent eruption of the Mono Craters, eastern central California. *Journal of Geophysical Research: Solid Earth*, 91(B12), 12539–12571. https://doi.org/10.1029/JB091iB12p12539

Tuffen, H., & Dingwell, D. (2005). Fault textures in volcanic conduits: Evidence for seismic trigger mechanisms during silicic eruptions. *Bulletin of Volcanology*, 67(4), 370–387. https://doi.org/10.1007/s00445-004-0383-5

Tuffen, H., Dingwell, D. B., & Pinkerton, H. (2003). Repeated fracture and healing of silicic magma generate flow banding and earthquakes? *Geology*, 31(12), 1089. https://doi.org/10.1130/G19777.1

Wadsworth, F. B., Llewellin, E. W., Vasseur, J., Gardner, J. E., & Tuffen, H. (2020). Explosive-effusive volcanic eruption transitions caused by sintering. *Science Advances*, 6(39), eaba7940. https://doi.org/10.1126/sciadv.aba7940

CHAPTER TWO

References are formatted for the Bulletin of Volcanology

Abdullin, R, Melnik, O, Rust, A, Blundy, J, Lgotina, E, Golovin, S (2024) Ascent of volatile-rich felsic magma in dykes: a numerical model applied to deep-sourced porphyry intrusions, Geophys J Int 236:1863–1876. https://doi.org/10.1093/gji/ggae027

Acocella, V, Neri, M (2009) Dike propagation in volcanic edifices: Overview and possible developments. Tectonophysics 471:67–77. https://doi.org/10.1016/j.tecto.2008.10.002

Ágústsdóttir, T, Woods, J, Greenfield, T, Green, R.G, White, R.S, Winder, T, Brandsdóttir, B,

Steinthórsson, S, Soosalu, H (2016) Strike-slip faulting during the 2014 Bárðarbunga-Holuhraun dike intrusion, central Iceland. Geophys Res Lett 43:1495–1503. https://doi.org/10.1002/2015GL067423

Albino, F, Biggs, J, Syahbana, DK (2019) Dyke intrusion between neighbouring arc volcanoes responsible for 2017 pre-eruptive seismic swarm at Agung. Nat Commun 10:748. https://doi.org/10.1038/s41467-019-08564-9

Barnett, ZA, Gudmundsson, A (2014) Numerical modelling of dykes deflected into sills to form a magma chamber. J Volcanol Geotherm Res 281:1–11. https://doi.org/10.1016/j.jvolgeores.2014.05.018

Bazargan, M, Gudmundsson, A (2019) Dike-induced stresses and displacements in layered volcanic zones. J Volcanol Geotherm Res 384:189–205. https://doi.org/10.1016/j.jvolgeores.2019.07.010

Caricchi, L, Pommier, A, Pistone, M, Castro, J, Burgisser, A, Perugini, D (2011) Strain-induced magma degassing: insights from simple-shear experiments on bubble bearing melts. Bull Volcanol 73:1245–1257. https://doi.org/10.1007/s00445-011-0471-2

Chadwick, WW, Dieterich, JH (1995) Mechanical modeling of circumferential and radial dike intrusion on Galapagos volcanoes. J Volcanol Geotherm Res 66:37–52. https://doi.org/10.1016/0377-0273(94)00060-t

Chen, Z, Jin, ZH, Johnson, SE (2011) Transient dike propagation and arrest near the level of neutral buoyancy. J Volcanol Geotherm Res 203:81–86. https://doi.org/10.1016/j.jvolgeores.2011.03.005

Clark, SP (1966) Handbook of Physical Constants. Geological Society of America. https://doi.org/10.1130/MEM97

Corbi, F, Rivalta, E, Pinel, V, Maccaferri, F, Bagnardi, M, Acocella, V (2015) How caldera collapse shapes the shallow emplacement and transfer of magma in active volcanoes. Earth Planet Sci Lett 431: 287–293. https://doi.org/10.1016/j.epsl.2015.09.028

Dahm T (2000) Numerical simulations of the propagation path and the arrest of fluid-filled fractures in the Earth. Geophys J Intl 141:623-638. https://doi.org/10.1046/j.1365-246x.2000.00102.x

Davis, T, Bagnardi, M, Lundgren, P, Rivalta, E (2021) Extreme curvature of shallow magma pathways controlled by competing stresses: Insights from the 2018 Sierra Negra eruption. Geophys Res Lett 48:e2021GL093038. https://doi.org/10.1029/2021gl093038

Donnelly-Nolan, JM, Grove, TL, Lanphere, MA, Champion, DE, Ramsey, DW (2008) Eruptive history and tectonic setting of Medicine Lake Volcano, a large rear-arc volcano in the southern \ Cascades. J Volcanol Geotherm Res 177:313–328. https://doi.org/10.1016/j.jvolgeores.2008.04.023

Feeley, TC, Cosca, MA (2003) Time vs. composition trends of magmatism at Sunlight volcano, Absaroka volcanic province, Wyoming. GSA Bull 115:714–728. https://doi.org/10.1130/0016-7606(2003)115<0714:TVCTOM>2.0.CO;2

Fierstein, J, Hildreth, W, Calvert, AT (2011) Eruptive history of South Sister, Oregon Cascades. J Volcanol Geotherm Res 207:145–179. https://doi.org/10.1016/j.jvolgeores.2011.06.003

Formenti, Y, Druitt, TH (2003) Vesicle connectivity in pyroclasts and implications for the fluidisation of fountain-collapse pyroclastic flows, Montserrat (West Indies). Earth Planet Sci Lett 214:561–574. https://doi.org/10.1016/S0012-821X(03)00386-8

Friese, N, Bense, FA, Tanner, DC, Gústafsson, LE, Siegesmund, S (2013) From feeder dykes to scoria cones: the tectonically controlled plumbing system of the Rauðhólar volcanic chain, Northern Volcanic Zone, Iceland. Bull Volcanol 75:717. https://doi.org/10.1007/s00445-013-0717-2

Geshi, N (2008) Vertical and lateral propagation of radial dikes inferred from the flow-direction analysis of the radial dike swarm in Komochi Volcano, Central Japan. J Volcanol Geotherm Res 173:122–134. https://doi.org/10.1016/j.jvolgeores.2008.01.001

Geshi, N, Browning, J, Kusumoto, S (2020) Magmatic overpressures, volatile exsolution and potential explosivity of fissure eruptions inferred via dike aspect ratios. Sci Rep 10:9406. https://doi.org/10.1038/s41598-020-66226-z

Geshi, N, Kusumoto, S, Gudmundsson, A (2012) Effects of mechanical layering of host rocks on dike growth and arrest. J Volcanol Geotherm Res 223:74–82. https://doi.org/10.1016/j.jvolgeores.2012.02.004

Geshi, N, Kusumoto, S, Gudmundsson, A (2010) Geometric difference between non-feeder and feeder dikes. Geology 38:195–198. https://doi.org/10.1130/G30350.1

Gonnermann, HM, Manga, M (2007) The Fluid Mechanics Inside a Volcano. Annu Rev Fluid Mech 39:321–356. https://doi.org/10.1146/annurev.fluid.39.050905.110207

Gries, RR (1985) San Juan Sag: Cretaceous Rocks in a Volcanic- Covered Basin, South Central Colorado. Mt Geol 22:167-179.

Gudmundsson, A (2011) Deflection of dykes into sills at discontinuities and magma-chamber formation. Tectonophysics 500:50–64. https://doi.org/10.1016/j.tecto.2009.10.015

Gudmundsson, A (2006) How local stresses control magma-chamber ruptures, dyke injections, and eruptions in composite volcanoes. Earth-Sci Rev 79:1–31. https://doi.org/10.1016/j.earscirev.2006.06.006

Gudmundsson, A (2002) Emplacement and arrest of sheets and dykes in central volcanoes. J Volcanol Geotherm Res 116:279–298.

Harp, AG (2021) Magma propagation and emplacement within the central intrusive complex of Summer Coon stratovolcano, Colorado. J Volcanol Geotherm Res 419:107372. https://doi.org/10.1016/j.jvolgeores.2021.107372

Harp, AG, Valentine, GA (2015). Shallow plumbing and eruptive processes of a scoria cone built on steep terrain. J Volcanol Geotherm Res 294:37–55. https://doi.org/10.1016/j.jvolgeores.2015.02.008

Harp, AG, Valentine, GA (2018) Emplacement controls for the basaltic-andesitic radial dikes of Summer Coon volcano and implications for flank vents at stratovolcanoes. Bull Volcanol 80:16. https://doi.org/10.1007/s00445-018-1194-4

Heimisson, ER, Hooper, A, Sigmundsson, F (2015) Forecasting the path of a laterally propagating dike. J Geophys Res Solid Earth 120:8774–8792. https://doi.org/10.1002/2015JB012402

Hotta, K, Iguchi, M, Tameguri, T (2016) Rapid dike intrusion into Sakurajima volcano on August 15, 2015, as detected by multi-parameter ground deformation observations. Earth Planet Space 68:68. https://doi.org/10.1186/s40623-016-0450-0

Huber, C, Bachmann, O, Manga, M (2010) Two Competing Effects of Volatiles on Heat Transfer in Crystal-rich Magmas: Thermal Insulation vs Defrosting. J Petrol 51:847–867. https://doi.org/10.1093/petrology/egq003

Huber, C, Townsend, M, Degruyter, W, Bachmann, O (2019) Optimal depth of subvolcanic magma chamber growth controlled by volatiles and crust rheology. Nat Geosci 12:762–768. https://doi.org/10.1038/s41561-019-0415-6

Iacovino, K, Till, CB (2019) DensityX: A program for calculating the densities of magmatic liquids up to 1,627 °C and 30 kbar. Volcanica 2:1–10. https://doi.org/10.30909/vol.02.01.0110

Jellinek, AM, DePaolo, DJ (2003) A model for the origin of large silicic magma chambers: precursors of caldera-forming eruptions. Bull Volcanol 65:363–381. https://doi.org/10.1007/s00445-003-0277-y

Johnson, RB (1968) Geology of the Igneous Rocks of the Spanish Peaks Region, Colorado. U.S. USGS Professional Paper 594-G. https://doi.org/10.3133/pp594G

Keating, GN, Valentine, GA, Krier, DJ, Perry, FV (2008) Shallow plumbing systems for small-volume basaltic volcanoes. Bull Volcanol 70:563–582. https://doi.org/10.1007/s00445-007-0154-1

Kervyn, M, Ernst, GGJ, Van Wyk De Vries, B, Mathieu, L, Jacobs, P (2009) Volcano load control on dyke propagation and vent distribution: Insights from analogue modeling. J Geophys Res Solid Earth 114:2008JB005653. https://doi.org/10.1029/2008JB005653

Klug, C, Cashman, KV (1994) Vesiculation of May 18, 1980, Mount St. Helens magma. Geology 22:468–472. https://doi.org/10.1130/0091-7613(1994)022<0468:VOMMSH>2.3.CO;2

Lipman, PW (1968) Geology of the Summer Coon volcanic center, eastern San Juan Mountains, Colorado. Colo Sch Mines Q 63:211–236.

Lipman, PW, Mehnert, HH (1975) Late Cenozoic Basaltic Volcanism and Development of the Rio Grande Depression in the Southern Rocky Mountains, in: Curtis, BF (ed.) Cenozoic History of the Southern Rocky Mountains. Geological Society of America, https://doi.org/10.1130/MEM144-p119

Lipman, PW, Steven, TA, Mehnert, HH (1970) Volcanic History of the San Juan Mountains, Colorado, as Indicated by Potassium–Argon Dating. GSA Bull 81:2329–2352. https://doi.org/10.1130/0016-7606(1970)81[2329:VHOTSJ]2.0.CO;2

Lipman, PW, Zimmerer, MJ, Gilmer, AK (2023) Precursors to a continental-arc ignimbrite flare-up: Early central volcanoes of the San Juan Mountains, Colorado, USA. Geosphere 20:23–73. https://doi.org/10.1130/GES02691.1

Lister, JR, Kerr, RC (1991) Fluid-mechanical models of crack propagation and their application to magma transport in dykes. J Geophys Res Solid Earth 96:10049–10077. https://doi.org/10.1029/91JB00600

Liu, Y, Zhang, Y, Behrens, H (2005) Solubility of H2O in rhyolitic melts at low pressures and a new empirical model for mixed H2O–CO2 solubility in rhyolitic melts. J Volcanol Geotherm Res

143:219–235. https://doi.org/10.1016/j.jvolgeores.2004.09.019

Maccaferri, F, Bonafede, M, Rivalta, E (2010) A numerical model of dyke propagation in layered elastic media. Geophys J Int 180:1107–1123. https://doi.org/10.1111/j.1365-246X.2009.04495.x

Maccaferri, F, Bonafede, M, Rivalta, E (2011) A quantitative study of the mechanisms governing dike propagation, dike arrest and sill formation. J Volcanol Geotherm Res 208:39–50. https://doi.org/10.1016/j.jvolgeores.2011.09.001

Mantiloni, L, Rivalta, E, Davis, T (2023) Mechanical Modeling of Pre-Eruptive Magma Propagation Scenarios at Calderas. J Geophys Res Solid Earth 128:e2022JB025956. https://doi.org/10.1029/2022JB025956

McTigue, DF, Mei, CC (1987) Gravity-induced stresses near axisymmetric topography of small slope. Intl J Num Anal Methods Geomech 11:257–268. https://doi.org/10.1002/nag.1610110304

Menand, T (2011) Physical controls and depth of emplacement of igneous bodies: A review. Tectonophysics 500:11–19. https://doi.org/10.1016/j.tecto.2009.10.016

Menand, T, Tait, SR (2002) The propagation of a buoyant liquid-filled fissure from a source under constant pressure: An experimental approach. J Geophys Res Solid Earth 107:2306. https://doi.org/10.1029/2001JB000589

Mertzman Jr, SA (1972) The geology and petrology of the Summer Coon Volcano, Colorado. Ph.D. Thesis. Case Western Reserve University.

Moats, WP (1990) Geometry and emplacement of silicic dikes at Summer Coon Volcano, Rio Grande and Saguache counties, Colorado. MS thesis. Arizona State University.

Moran, SC, Newhall, C, Roman, DC (2011) Failed magmatic eruptions: late-stage cessation of magma ascent. Bull Volcanol 73:115–122. https://doi.org/10.1007/s00445-010-0444-x

Perry FV, WoldeGabriel G, Valentine GA, Desmarais EK, Heiken G, Heizler M, Yamakawa M, Umeda K (1999) High-level radioactive waste disposal and volcanic hazard in Japan: A natural analog study of the Summer Coon volcano, Colorado. Geological Society of America Abstracts with Programs 31: A-478

Pinel, V, Jaupart, C (2004) Magma storage and horizontal dyke injection beneath a volcanic edifice. Earth Planet Sci Lett 221:245–262. https://doi.org/10.1016/S0012-821X(04)00076-7

Pinel, V, Jaupart, C (2000) The effect of edifice load on magma ascent beneath a volcano. Philos Trans R Soc Lond A 358:1515–1532. https://doi.org/10.1098/rsta.2000.0601

Poland, MP, Fink, JH, Tauxe, L (2004) Patterns of magma flow in segmented silicic dikes at Summer Coon volcano, Colorado: AMS and thin section analysis. Earth Planet Sci Lett 219:155–169. https://doi.org/10.1016/S0012-821X(03)00706-4

Poland, MP, Moats, WP, Fink, JH (2008) A model for radial dike emplacement in composite cones based on observations from Summer Coon volcano, Colorado, USA. Bull Volcanol 70:861–875. https://doi.org/10.1007/s00445-007-0175-9

Rasmussen, DJ, Plank, TA, Roman, DC, Zimmer, MM (2022) Magmatic water content controls the pre-eruptive depth of arc magmas. Science 375:1169–1172. https://doi.org/10.1126/science.abm5174

Rivalta, E, Böttinger, M, Dahm, T (2005) Buoyancy-driven fracture ascent: Experiments in layered gelatine. J Volcanol Geotherm Res 144:273–285. https://doi.org/10.1016/j.jvolgeores.2004.11.030

Rivalta, E, Dahm, T (2006) Acceleration of buoyancy-driven fractures and magmatic dikes beneath the free surface. Geophys J Int 166:1424–1439. https://doi.org/10.1111/j.1365-246X.2006.02962.x

Rivalta, E, Taisne, B, Bunger, AP, Katz, RF (2015) A review of mechanical models of dike propagation: Schools of thought, results and future directions. Tectonophysics 638:1–42. https://doi.org/10.1016/j.tecto.2014.10.003

Rubin, AM (1995a) Getting granite dikes out of the source region. J Geophys Res Solid Earth 100:5911–5929. https://doi.org/10.1029/94JB02942

Rubin, AM (1995b) Propagation of magma-filled cracks. Ann Rev Earth Planetary Sci 23:287-336. https://doi.org/10.1146/annurev.ea.23.050195.001443

Rubin, AM, Pollard, DD (1987) Origins of blade-like dikes in volcanic rift zones. USGS Professional Paper 1350:1449–1470.

Rust, AC, Manga, M, Cashman, KV (2003) Determining flow type, shear rate and shear stress in magmas from bubble shapes and orientations. J Volcanol Geotherm Res 122:111–132. https://doi.org/10.1016/S0377-0273(02)00487-0

Ryan, MP (1988) The mechanics and three-dimensional internal structure of active magmatic systems: Kilauea Volcano, Hawaii. J Geophys Res Solid Earth 93:4213–4248. https://doi.org/10.1029/JB093iB05p04213

Schneider CA, Rasband WS, Eliceiri KW (2012) NIH Image to ImageJ: 25 years of image analysis. Nat Meth 9:671–675.https://doi.org/ 10.1038/nmeth.2089

Shelley, D (1985) Determining paleo-flow directions from groundmass fabrics in the Lyttelton radial dykes, New Zealand. J Volcanol Geotherm Res 25:69–79. https://doi.org/10.1016/0377-0273(85)90005-8

Sieh, K, Bursik, M (1986) Most recent eruption of the Mono Craters, eastern central California. J Geophys Res Solid Earth 91:12539–12571. https://doi.org/10.1029/JB091iB12p12539

Sigmundsson, F, Hooper, A, Hreinsdóttir, S, Vogfjörd, KS, Ófeigsson, BG, Heimisson, ER, Dumont, S, Parks, M, Spaans, K, Gudmundsson, GB, Drouin, V, Árnadóttir, T, Jónsdóttir, K, Gudmundsson, MT, Högnadóttir, T, Fridriksdóttir, HM, Hensch, M, Einarsson, P, Magnússon, E, ... Eibl, EPS (2015) Segmented lateral dyke growth in a rifting event at Bárðarbunga volcanic system, Iceland. Nature, 517: 191–195. https://doi.org/10.1038/nature14111

Smith RP (1975) Structure and Petrology of Spanish Peaks Dikes. Ph.D. Thesis. University of Colorado Boulder.

Stasiuk, MV, Barclay, J, Carroll, MR, Jaupart, C, Ratté, JC, Sparks, RSJ, Tait, SR (1996) Degassing during magma ascent in the Mule Creek vent (USA). Bull Volcanol 58:117–130. https://doi.org/10.1007/s004450050130

Taisne, B, Jaupart, C (2009) Dike propagation through layered rocks. J Geophys Res Solid Earth 114. https://doi.org/10.1029/2008JB006228

Townsend, M, Pollard, DD, Johnson, K, Culha, C (2015) Jointing around magmatic dikes as a precursor to the development of volcanic plugs. Bull Volcanol 77:92. https://doi.org/10.1007/s00445-015-0978-z

Townsend, MR, Pollard, DD, Smith, RP (2017) Mechanical models for dikes: A third school of thought. Tectonophysics 703–704:98–118. https://doi.org/10.1016/j.tecto.2017.03.008

Urbani, S, Acocella, V, Rivalta, E, Corbi, F (2017) Propagation and arrest of dikes under topography: Models applied to the 2014 Bardarbunga (Iceland) rifting event. Geophys Res Let 44:6692–6701. https://doi.org/10.1002/2017GL073130

Urbani, S, Acocella, V, Rivalta, E (2018) What Drives the Lateral Versus Vertical Propagation of Dikes? Insights From Analogue Models. J Geophys Res Solid Earth 123:3680–3697. https://doi.org/10.1029/2017JB015376

Walker, GPL (1986) Koolau Dike Complex, Oahu: Intensity and origin of a sheeted-dike complex high in a Hawaiian volcanic edifice. Geology 14:310–313. https://doi.org/10.1130/0091-7613(1986)14<310:KDCOIA>2.0.CO;2

White, RA, McCausland, WA (2019) A process-based model of pre-eruption seismicity patterns and its use for eruption forecasting at dormant stratovolcanoes. J Volcanol Geotherm Res 382:267–297. https://doi.org/10.1016/j.jvolgeores.2019.03.004

White, SM, Crisp, JA, Spera, FJ (2006) Long-term volumetric eruption rates and magma budgets. Geochem Geophys Geosystems 7:1-20. https://doi.org/10.1029/2005GC001002

Zellmer, GF, Rubin, KH, Dulski, P, Iizuka, Y, Goldstein, SL, Perfit, MR (2011) Crystal growth during dike injection of MOR basaltic melts: evidence from preservation of local Sr disequilibria in plagioclase. Contrib Mineral Petrol 161:153–173. https://doi.org/10.1007/s00410-010-0518-y

Zhan, Y, Roman, DC, Le Mével, H, Power, JA (2022) Earthquakes Indicated Stress Field Change during the 2006 Unrest of Augustine Volcano, Alaska. Geophys Res Lett 49: e2022GL097958. https: doi.org/10.1029/2022GL097958

CHAPTER THREE

Abdullin, R., Melnik, O., Rust, A., Blundy, J., Lgotina, E., & Golovin, S. (2024). Ascent of volatile-rich felsic magma in dykes: A numerical model applied to deep-sourced porphyry intrusions. *Geophysical Journal International*, 236(3), 1863–1876. https://doi.org/10.1093/gji/ggae027

Acocella, V., Behncke, B., Neri, M., & D'Amico, S. (2003). Link between major flank slip and 2002–2003 eruption at Mt. Etna (Italy). *Geophysical Research Letters*, 30(24). https://doi.org/10.1029/2003GL018642

Acocella, V., & Neri, M. (2009). Dike propagation in volcanic edifices: Overview and possible developments. *Tectonophysics*, 471(1–2), 67–77. https://doi.org/10.1016/j.tecto.2008.10.002

Aksit, G. G., Townsend, M., & Harp, A. (2025). The influence of magma density and edifice stresses on silicic dike propagation trajectories at Summer Coon volcano, Colorado, USA. *Bulletin of Volcanology*, 87(10), 81. https://doi.org/10.1007/s00445-025-01870-9

Allgood, C., Llewellin, E. W., Brown, R. J., & Loisel, A. (2025). Magma flow localisation during dyke propagation produces complex magma transport pathways. *Nature Communications*, 16, 6358. https://doi.org/10.1038/s41467-025-61620-5

Bachmann, O., & Bergantz, G. W. (2008). Rhyolites and their Source Mushes across Tectonic Settings. *Journal of Petrology*, 49(12), 2277–2285. https://doi.org/10.1093/petrology/egn068

Burgisser, A., Collombet, M., Narbona-Reina, G., & Bresch, D. (2024). Two-phase magma flow with phase exchange: Part II. 1.5D numerical simulations of a volcanic conduit. *Studies in Applied Mathematics*, 153(3), e12747. https://doi.org/10.1111/sapm.12747

Caricchi, L., Pommier, A., Pistone, M., Castro, J., Burgisser, A., & Perugini, D. (2011). Strain-induced magma degassing: Insights from simple-shear experiments on bubble bearing melts. *Bulletin of Volcanology*, 73(9), 1245–1257. https://doi.org/10.1007/s00445-011-0471-2

Caricchi, L., Simpson, G., & Schaltegger, U. (2016). Estimates of Volume and Magma Input in Crustal Magmatic Systems from Zircon Geochronology: The Effect of Modeling Assumptions and System Variables. *Frontiers in Earth Science*, 4. https://doi.org/10.3389/feart.2016.00048

Chadwick, W. W., & Dieterich, J. H. (1995). Mechanical modeling of circumferential and radial dike intrusion on Galapagos volcanoes. *Journal of Volcanology and Geothermal Research*, 66(1–4), 37–52. https://doi.org/10.1016/0377-0273(94)00060-T

Colombier, M., Wadsworth, F. B., Scheu, B., Vasseur, J., Dobson, K. J., Cáceres, F., Allabar, A., Marone, F., Schlepütz, C. M., & Dingwell, D. B. (2020). In situ observation of the percolation threshold in multiphase magma analogues. *Bulletin of Volcanology*, 82(4), 32. https://doi.org/10.1007/\s00445-020-1370-1

Davis, T., Bagnardi, M., Lundgren, P., & Rivalta, E. (2021). Extreme Curvature of Shallow Magma Pathways Controlled by Competing Stresses: Insights From the 2018 Sierra Negra Eruption. *Geophysical Research Letters*, 48(13), e2021GL093038. https://doi.org/10.1029/2021GL093038

Davis, T., Rivalta, E., & Dahm, T. (2020). Critical Fluid Injection Volumes for Uncontrolled Fracture Ascent. *Geophysical Research Letters*, 47(14), e2020GL087774. https://doi.org/10.1029/2020GL087774

Feeley, T. C., & Cosca, M. A. (2003). Time vs. Composition trends of magmatism at Sunlight volcano, Absaroka volcanic province, Wyoming. *Geological Society of America Bulletin*, 115, 714–728. https://doi.org/10.1130/0016-7606(2003)115%253C0714:TVCTOM%253E2.0.CO;2

Formenti, Y., & Druitt, T. H. (2003). Vesicle connectivity in pyroclasts and implications for the fluidisation of fountain-collapse pyroclastic flows, Montserrat (West Indies). *Earth and Planetary Science Letters*, 214(3–4), 561–574. https://doi.org/10.1016/S0012-821X(03)00386-8

Fukushima, Y., Cayol, V., & Durand, P. (2005). Finding realistic dike models from interferometric s ynthetic aperture radar data: The February 2000 eruption at Piton de la Fournaise. *Journal of Geophysical Research: Solid Earth*, 110(B3). https://doi.org/10.1029/2004JB003268

Geshi, N., Browning, J., & Kusumoto, S. (2020). Magmatic overpressures, volatile exsolution and potential explosivity of fissure eruptions inferred via dike aspect ratios. *Scientific Reports*, 10(1), 9406. https://doi.org/10.1038/s41598-020-66226-z

Giachetti, T., Gonnermann, H. M., Gardner, J. E., Burgisser, A., Hajimirza, S., Earley, T. C., Truong, N., & Toledo, P. (2019). Bubble Coalescence and Percolation Threshold in Expanding Rhyolitic Magma. *Geochemistry, Geophysics, Geosystems*, 20(2), 1054–1074. https://doi.org/10.1029/2018GC008006

Goldman, R. T., Albright, J. A., Gravley, D. M., Grosfils, E. B., Gregg, P. M., & Hampton, S. J. (2022). Stress Control of Dike Deflection and Flank Eruption at Akaroa Volcano, New Zealand. *Journal of Geophysical Research: Solid Earth*, 127(8), e2022JB024305. https://doi.org/10.1029/2022JB024305

Gonnermann, H. M., & Manga, M. (2003). Explosive volcanism may not be an inevitable consequence of magma fragmentation. *Nature*, 426(6965), 432–435. https://doi.org/10.1038/nature02138

Gorbach, N. V., Portnyagin, M. V., & Philosofova, T. M. (2016). Dynamics of exrtrusive dome growth and variations in chemical and mineralogical composition of Young Shiveluch andesites in 2001–2013. *Journal of Volcanology and Seismology*, 10(6), 360–381. https://doi.org/10.1134/S0742046316060038

Harp, A. G. (2018). *The Impacts of Local Stress Fields and Host Rock Heterogeneity on Magma Transport and Extrusion at Stratovolcanoes* (Doctoral dissertation, State University of New York at Buffalo).

Harp, A. G. (2021). Magma propagation and emplacement within the central intrusive complex of Summer Coon stratovolcano, Colorado. *Journal of Volcanology and Geothermal Research*, 419, 107372. https://doi.org/10.1016/j.jvolgeores.2021.107372

Harp, A. G., & Valentine, G. A. (2018). Emplacement controls for the basaltic-andesitic radial dikes of Summer Coon volcano and implications for flank vents at stratovolcanoes. *Bulletin of Volcanology*, 80(2), 16. https://doi.org/10.1007/s00445-018-1194-4

Heap, M. J., Villeneuve, M., Albino, F., Farquharson, J. I., Brothelande, E., Amelung, F., Got, J.-L., & Baud, P. (2020). Towards more realistic values of elastic moduli for volcano modelling. *Journal of Volcanology and Geothermal Research*, 390, 106684. https://doi.org/10.1016/j.jvolgeores.2019.106684

Heimisson, E. R., Hooper, A., & Sigmundsson, F. (2015). Forecasting the path of a laterally propagating dike. *Journal of Geophysical Research: Solid Earth*, 120(12), 8774–8792. https://doi.org/10.1002/2015JB012402

Holohan, E. P., Schöpfer, M. P. J., & Walsh, J. J. (2011). Mechanical and geometric controls on the structural evolution of pit crater and caldera subsidence. *Journal of Geophysical Research*, 116(B7), B07202. https://doi.org/10.1029/2010JB008032

Karakas, O., Degruyter, W., Bachmann, O., & Dufek, J. (2017). Lifetime and size of shallow magma bodies controlled by crustal-scale magmatism. *Nature Geoscience*, 10(6), 446–450. https://doi.org/10.1038/ngeo2959

Klug, C., & Cashman, K. V. (1994). Vesiculation of May 18, 1980, Mount St. Helens magma. *Geology*, 22(5), 468. https://doi.org/10.1130/0091-7613(1994)022%253C0468:VOMMSH%253E2.3.CO;2

Lindoo, A., Larsen, J. F., Cashman, K. V., Dunn, A. L., & Neill, O. K. (2016). An experimental study of permeability development as a function of crystal-free melt viscosity. *Earth and Planetary Science Letters*, 435, 45–54. https://doi.org/10.1016/j.epsl.2015.11.035

Lipman, P. W. (1968). Geology of the Summer Coon volcanic center, eastern San Juan Mountains, Colorado. *Colorado School of Mines Quarterly*, 63:211-236.

Lipman, P. W. (1976). Geologic map of the Del Norte area, eastern San Juan Mountains, Colorado. *U.S. Geological Survey Miscellaneous Investigations* I-952.

Lipman, P. W., Steven, T. A., & Mehnert, H. H. (1970). Volcanic History of the San Juan Mountains, Colorado, as Indicated by Po3sium–Argon Dating. *Geological Society of America Bulletin*, 81(8), 2329. https://doi.org/10.1130/0016-7606(1970)81%255B2329:VHOTSJ%255D2.0.CO;2

Lipman, P. W., Zimmerer, M. J., & Gilmer, A. K. (2024). Precursors to a continental-arc ignimbrite flare-up: Early central volcanoes of the San Juan Mountains, Colorado, USA. *Geosphere*, 20(1), 23–73. https://doi.org/10.1130/GES02691.1

Lister, J. R. (1990). Buoyancy-driven fluid fracture: The effects of material toughness and of low-viscosity precursors. *Journal of Fluid Mechanics*, 210, 263–280. https://doi.org/10.1017/S0022112090001288

Lister, J. R., & Kerr, R. C. (1991). Fluid-mechanical models of crack propagation and their application to magma transport in dykes. *Journal of Geophysical Research: Solid Earth*, 96(B6), 10049–10077. https://doi.org/10.1029/91JB00600

Liu, Y., Zhang, Y., & Behrens, H. (2005). Solubility of H2O in rhyolitic melts at low pressures and a new empirical model for mixed H2O–CO2 solubility in rhyolitic melts. *Journal of Volcanology and Geothermal Research*, 143(1–3), 219–235. https://doi.org/10.1016/j.jvolgeores.2004.09.019

Maimon, O., Lyakhovsky, V., Melnik, O., & Navon, O. (2012). The propagation of a dyke driven by gas-saturated magma. *Geophysical Journal International*, 189(2), 956–966. https://doi.org/10.1111/j.1365-246X.2012.05342.x

Martel, S. J., & Muller, J. R. (2000). A Two-dimensional Boundary Element Method for Calculating Elastic Gravitational Stresses in Slopes. *Pure and Applied Geophysics*, 157(6–8), 989–1007. https://doi.org/10.1007/s000240050014

Mastin, L. G., & Ghiorso, M. S. (2000). A numerical program for steady-state flow of magma-gas mixtures through vertical eruptive conduits (No. 2000-209). *US Geological Survey*

Melnik, O., & Sparks, R. S. J. (2005). Controls on conduit magma flow dynamics during lava dome building eruptions. *Journal of Geophysical Research: Solid Earth*, 110(B2). https://doi.org/10.1029/2004JB003183

Mertzman, S. (1972). *The geology and petrology of the Summer Coon Volcano, Colorado.* (Doctoral dissertation, Case Western University)

Moats, W. P. (1990). *Geometry and emplacement of silicic dikes at Summer Coon volcano, Rio Grande and Saguache Counties, Colorado.* (M.S. Thesis, Arizona State University)

Okumura, S., Nakamura, M., Nakano, T., Uesugi, K., & Tsuchiyama, A. (2010). Shear deformation experiments on vesicular rhyolite: Implications for brittle fracturing, degassing, and compaction of magmas in volcanic conduits. *Journal of Geophysical Research: Solid Earth*, 115(B6). https://doi.org/10.1029/2009JB006904

Okumura, S., Nakamura, M., Uesugi, K., Nakano, T., & Fujioka, T. (2013). Coupled effect of magma degassing and rheology on silicic volcanism. *Earth and Planetary Science Letters*, 362, 163–170. https://doi.org/10.1016/j.epsl.2012.11.056

Papale, P., Neri, A., & Macedonio, G. (1998). The role of magma composition and water content in explosive eruptions: 1. Conduit ascent dynamics. *Journal of Volcanology and Geothermal Research*, 87(1-4), 75-93.

Parmigiani, A., Degruyter, W., Leclaire, S., Huber, C., & Bachmann, O. (2017). The mechanics of shallow magma reservoir outgassing. *Geochemistry, Geophysics, Geosystems*, 18(8), 2887–2905. https://doi.org/10.1002/2017GC006912

Pinel, V., & Jaupart, C. (2000). The effect of edifice load on magma ascent beneath a volcano. *Philosophical Transactions of the Royal Society of London. Series A: Mathematical, Physical and Engineering Sciences*, 358(1770), 1515–1532. https://doi.org/10.1098/rsta.2000.0601

Pinel, V., & Jaupart, C. (2004). Magma storage and horizontal dyke injection beneath a volcanic edifice. *Earth and Planetary Science Letters*, 221(1–4), 245–262. https://doi.org/10.1016/S0012-821X(04)00076-7

Pinel, V., & Mériaux, C. A. (2025). Subsurface lateral magma propagation from Nyiragongo volcano in the Western Rift Zone of the East African Rift. *Journal of African Earth Sciences*, 226, 105569. https://doi.org/10.1016/j.jafrearsci.2025.105569

Plank, T., Kelley, K. A., Zimmer, M. M., Hauri, E. H., & Wallace, P. J. (2013). Why do mafic arc magmas contain ~4wt% water on average? *Earth and Planetary Science Letters*, 364, 168–179. https://doi.org/10.1016/j.epsl.2012.11.044

Poland, M. P., Fink, J. H., & Tauxe, L. (2004). Patterns of magma flow in segmented silicic dikes at Summer Coon volcano, Colorado: AMS and thin section analysis. *Earth and Planetary Science Letters*, 219(1–2), 155–169. https://doi.org/10.1016/S0012-821X(03)00706-4

Poland, M. P., Moats, W. P., & Fink, J. H. (2008). A model for radial dike emplacement in composite cones based on observations from Summer Coon volcano, Colorado, USA. *Bulletin of Volcanology*, 70(7), 861–875. https://doi.org/10.1007/s00445-007-0175-9

Pollard, D. D., & Townsend, M. R. (2018). Fluid-filled fractures in Earth's lithosphere: Gravitational loading, interpenetration, and stable height of dikes and veins. *Journal of Structural Geology*, 109, 38–54. https://doi.org/10.1016/j.jsg.2017.11.007

Rasmussen, D. J., Plank, T. A., Roman, D. C., & Zimmer, M. M. (2022). Magmatic water content controls the pre-eruptive depth of arc magmas. *Science*, 375(6585), 1169–1172. https://doi.org/10.1126/science.abm5174

Rivalta, E., & Dahm, T. (2006). Acceleration of buoyancy-driven fractures and magmatic dikes beneath the free surface. *Geophysical Journal International,* 166(3), 1424–1439. https://doi.org/10.1111/j.1365-246X.2006.02962.x

Rivalta, E., Taisne, B., Bunger, A. P., & Katz, R. F. (2015). A review of mechanical models of dike propagation: Schools of thought, results and future directions. *Tectonophysics*, 638, 1–42. https://doi.org/10.1016/j.tecto.2014.10.003

Roman, A., & Jaupart, C. (2014). The impact of a volcanic edifice on intrusive and eruptive activity. *Earth and Planetary Science Letters*, 408, 1–8. https://doi.org/10.1016/j.epsl.2014.09.016

Rubin, A. M. (1993). Tensile fracture of rock at high confining pressure: Implications for dike propagation. *Journal of Geophysical Research: Solid Earth*, 98(B9), 15919–15935. https://doi.org/10.1029/93JB01391

Rubin, A. M. (1995). Getting granite dikes out of the source region. *Journal of Geophysical Research: Solid Earth*, 100(B4), 5911–5929. https://doi.org/10.1029/94JB02942

Rubin, A. M., & Pollard, D. D. (1987). Origins of blade-like dikes in volcanic rift zones. *US Geological Survey Professional Paper*, 1350(2), 1449-1470.

Ryan, M. P. (1988). The mechanics and three-dimensional internal structure of active magmatic systems: Kilauea Volcano, Hawaii. *Journal of Geophysical Research: Solid Earth*, 93(B5), 4213–4248. https://doi.org/10.1029/JB093iB05p04213

Scholz, K. J. (2025). *Magmatic Processes Throughout the Crust: Deep Long-Period Earthquakes, Magma Chamber Evolution, and Topographic Influences on Shallow Dike Transport.* (Doctoral dissertation, University of Oregon).

Secor, D. T., & Pollard, D. D. (1975). On the stability of open hydraulic fractures in the Earth's crust. *Geophysical Research Letters*, 2(11), 510–513. https://doi.org/10.1029/GL002i011p00510

Segall, P., Cervelli, P., Owen, S., Lisowski, M., & Miklius, A. (2001). Constraints on dike propagation from continuous GPS measurements. *Journal of Geophysical Research: Solid Earth*, 106(B9), 19301–19317. https://doi.org/10.1029/2001JB000229

Shea, T., Houghton, B. F., Gurioli, L., Cashman, K. V., Hammer, J. E., & Hobden, B. J. (2010). Textural studies of vesicles in volcanic rocks: An integrated methodology. *Journal of Volcanology and Geothermal Research*, 190(3–4), 271–289. https://doi.org/10.1016/j.jvolgeores.2009.12.003

Sigmundsson, F., Parks, M., Geirsson, H., Hooper, A., Drouin, V., Vogfjörd, K. S., Ófeigsson, B. G., Greiner, S. H. M., Yang, Y., Lanzi, C., De Pascale, G. P., Jónsdóttir, K., Hreinsdóttir, S., Tolpekin, V., Friðriksdóttir, H. M., Einarsson, P., & Barsotti, S. (2024). Fracturing and tectonic stress drive ultrarapid magma flow into dikes. *Science*, 383(6688), 1228–1235. https://doi.org/10.1126/science.adn2838

Smittarello, D., Smets, B., Barrière, J., Michellier, C., Oth, A., Shreve, T., Grandin, R., Theys, N., Brenot, H., Cayol, V., Allard, P., Caudron, C., Chevrel, O., Darchambeau, F., De Buyl, P., Delhaye, L., Derauw, D., Ganci, G., Geirsson, H., ... Syavulisembo Muhindo, A. (2022). Precursor-free eruption triggered by edifice rupture at Nyiragongo volcano. *Nature*, 609(7925), 83–88. https://doi.org/10.1038/s41586-022-05047-8

Taisne, B., & Jaupart, C. (2011). Magma expansion and fragmentation in a propagating dyke. *Earth and Planetary Science Letters*, 301(1–2), 146–152. https://doi.org/10.1016/j.epsl.2010.10.038

Taisne, B., & Tait, S. (2009). Eruption versus intrusion? Arrest of propagation of constant volume, buoyant, liquid-filled cracks in an elastic, brittle host. *Journal of Geophysical Research: Solid Earth*, 114(B6). https://doi.org/10.1029/2009JB006297

Townsend, M. R., Pollard, D. D., & Smith, R. P. (2017). Mechanical models for dikes: A third school of thought. *Tectonophysics*, 703–704, 98–118. https://doi.org/10.1016/j.tecto.2017.03.008

Ueda, H., Fujita, E., Ukawa, M., Yamamoto, E., Irwan, M., & Kimata, F. (2005). Magma intrusion and discharge process at the initial stage of the 2000 activity of Miyakejima, Central Japan, inferred

from tilt and GPS data. *Geophysical Journal International*, 161(3), 891–906. https://doi.org/10.1111/j.1365-246X.2005.02602.x

Walker, G. P. L. (1989). Gravitational (density) controls on volcanism, magma chambers and intrusions. *Australian Journal of Earth Sciences*, 36(2), 149–165. https://doi.org/10.1080/08120098908729479

Wong, Y., & Segall, P. (2019). Numerical Analysis of Time-Dependent Conduit Magma Flow in Dome-Forming Eruptions With Application to Mount St. Helens 2004–2008. *Journal of Geophysical Research: Solid Earth*, 124(11), 11251–11273. https://doi.org/10.1029/2019JB017585

Woods, J., Winder, T., White, R. S., & Brandsdóttir, B. (2019). Evolution of a lateral dike intrusion revealed by relatively-relocated dike-induced earthquakes: The 2014–15 Bárðarbunga–Holuhraun rifting event, Iceland. *Earth and Planetary Science Letters*, 506, 53–63. https://doi.org/10.1016/j.epsl.2018.10.032

CHAPTER FOUR

Aksit, G. G., Townsend, M., & Harp, A. (2025). The influence of magma density and edifice stresses on silicic dike propagation trajectories at Summer Coon volcano, Colorado, USA. *Bulletin of Volcanology*, 87(10), 81. https://doi.org/10.1007/s00445-025-01870-9

Aravena, Á., Cioni, R., de'Michieli Vitturi, M., & Neri, A. (2018). Conduit stability effects on intensity and steadiness of explosive eruptions. *Scientific Reports*, 8(1), 4125. https://doi.org/10.1038/s41598-018-22539-8

Carslaw, H., & Jaeger, J. (1959). *Conduction of Heat in Solids (2nd ed)*. Clarendon Press, New York. 510 pages.

Cashman, K. V., Thornber, C. R., & Pallister, J. S. (2008). From Dome to Dust: Shallow Crystallization and Fragmentation of Conduit Magma During the 2004–2006 Dome Extrusion of Mount St. Helens, Washington. In *A Volcano Rekindled: The Renewed Eruption of Mount St. Helens, 2004-2006*. US Geologic Survey Professional paper 1750-19, pp. 387–413.

Cassidy, M., Manga, M., Cashman, K., & Bachmann, O. (2018). Controls on explosive-effusive volcanic eruption styles. *Nature Communications*, 9(1), 2839. https://doi.org/10.1038/s41467-018-05293-3

Castro, J. M., Cordonnier, B., Tuffen, H., Tobin, M. J., Puskar, L., Martin, M. C., & Bechtel, H. A. (2012). The role of melt-fracture degassing in defusing explosive rhyolite eruptions at volcán Chaitén. *Earth and Planetary Science Letters*, 333–334, 63–69. https://doi.org/10.1016/j.epsl.2012.04.024

Castro, J. M., Schipper, C. I., Mueller, S. P., Militzer, A. S., Amigo, A., Parejas, C. S., & Jacob, D. (2013). Storage and eruption of near-liquidus rhyolite magma at Cordón Caulle, Chile. *Bulletin of Volcanology*, 75(4), 702. https://doi.org/10.1007/s00445-013-0702-9

Degruyter, W., Huber, C., Bachmann, O., Cooper, K. M., & Kent, A. J. R. (2017). Influence of Exsolved Volatiles on Reheating Silicic Magmas by Recharge and Consequences for Eruptive Style at Volcán Quizapu (Chile). *Geochemistry, Geophysics, Geosystems*, 18(11), 4123–4135. https://doi.org/10.1002/2017GC007219

Donnelly-Nolan, J. M., Grove, T. L., Lanphere, M. A., Champion, D. E., & Ramsey, D. W. (2008). Eruptive history and tectonic setting of Medicine Lake Volcano, a large rear-arc volcano in the southern Cascades. *Journal of Volcanology and Geothermal Research*, 177(2), 313–328. https://doi.org/10.1016/j.jvolgeores.2008.04.023

Eichelberger, J. C. (1995). Silicic Volcanism: Ascent of Viscous Magmas from Crustal Reservoirs. *Annual Review of Earth and Planetary Sciences*, 23(1), 41–63. https://doi.org/10.1146/annurev.ea.23.050195.000353

Fierstein, J., Hildreth, W., & Calvert, A. T. (2011). Eruptive history of South Sister, Oregon Cascades. *Journal of Volcanology and Geothermal Research*, 207(3–4), 145–179. https://doi.org/10.1016/j.jvolgeores.2011.06.003

Fink, J. H., & Pollard, D. D. (1983). Structural evidence for dikes beneath silicic domes, Medicine Lake Highland Volcano, California. *Geology*, 11(8), 458. https://doi.org/10.1130/0091-7613(1983)11%253C458:SEFDBS%253E2.0.CO;2

Gardner, J. E., Llewellin, E. W., Watkins, J. M., & Befus, K. S. (2017). Formation of obsidian pyroclasts by sintering of ash particles in the volcanic conduit. *Earth and Planetary Science Letters*, 459, 252–263. https://doi.org/10.1016/j.epsl.2016.11.037

Gardner, J. E., Wadsworth, F. B., Llewellin, E. W., Watkins, J. M., & Coumans, J. P. (2018). Experimental sintering of ash at conduit conditions and implications for the longevity of tuffisites. *Bulletin of Volcanology*, 80(3), 23. https://doi.org/10.1007/s00445-018-1202-8

Giachetti, T., Gonnermann, H. M., Gardner, J. E., Shea, T., & Gouldstone, A. (2015). Discriminating secondary from magmatic water in rhyolitic matrix-glass of volcanic pyroclasts using thermogravimetric analysis. *Geochimica et Cosmochimica Acta*, 148, 457–476. https://doi.org/10.1016/j.gca.2014.10.017

Giachetti, T., Hudak, M. R., Shea, T., Bindeman, I. N., & Hoxsie, E. C. (2020). D/H ratios and H2O contents record degassing and rehydration history of rhyolitic magma and pyroclasts. *Earth and Planetary Science Letters*, 530, 115909. https://doi.org/10.1016/j.epsl.2019.115909

Gonnermann, H. M., & Manga, M. (2003). Explosive volcanism may not be an inevitable consequence of magma fragmentation. *Nature*, 426(6965), 432–435. https://doi.org/10.1038/nature02138

Google Earth Pro. (n.d.). Satellite imagery of Latitude 37.801099° Longitude -106.355107°. Retrieved October 1, 2025.

Hammer, J. E., & Rutherford, M. J. (2002). An experimental study of the kinetics of decompression-induced crystallization in silicic melt. *Journal of Geophysical Research: Solid Earth*, 107(B1). https://doi.org/10.1029/2001JB000281

Harp, A. G. (2018). *The Impacts of Local Stress Fields and Host Rock Heterogeneity on Magma Transport and Extrusion at Stratovolcanoes* (Doctoral dissertation, State University of New York at Buffalo)

Harp, A. G. (2021). Magma propagation and emplacement within the central intrusive complex of Summer Coon stratovolcano, Colorado. *Journal of Volcanology and Geothermal Research*, 419, 107372. https://doi.org/10.1016/j.jvolgeores.2021.107372

Harp, A. G., & Valentine, G. A. (2018). Emplacement controls for the basaltic-andesitic radial dikes of Summer Coon volcano and implications for flank vents at stratovolcanoes. *Bulletin of Volcanology*, 80(2), 16. https://doi.org/10.1007/s00445-018-1194-4

Houghton, B. F., Wilson, C. J. N., Del Carlo, P., Coltelli, M., Sable, J. E., & Carey, R. (2004). The influence of conduit processes on changes in style of basaltic Plinian eruptions: Tarawera 1886 and Etna 122 BC. *Journal of Volcanology and Geothermal Research*, 137(1–3), 1–14. https://doi.org/10.1016/j.jvolgeores.2004.05.009

Kaminski, E., & Jaupart, C. (1998). The size distribution of pyroclasts and the fragmentation sequence in explosive volcanic eruptions. *Journal of Geophysical Research: Solid Earth*, 103(B12), 29759–29779. https://doi.org/10.1029/98JB02795

Kennedy, B. M., Jellinek, A. M., Russell, J. K., Nichols, A. R. L., & Vigouroux, N. (2010). Time-and temperature-dependent conduit wall porosity: A key control on degassing and explosivity at Tarawera volcano, New Zealand. *Earth and Planetary Science Letters*, 299(1–2), 126–137. https://doi.org/10.1016/j.epsl.2010.08.028

Klug, C., & Cashman, K. V. (1994). Vesiculation of May 18, 1980, Mount St. Helens magma. *Geology*, 22(5), 468. https://doi.org/10.1130/0091-7613(1994)022%253C0468:VOMMSH%253E2.3.CO;2

Kolzenburg, S., Ryan, A. G., & Russell, J. K. (2019). Permeability evolution during non-isothermal compaction in volcanic conduits and tuffisite veins: Implications for pressure monitoring of volcanic edifices. *Earth and Planetary Science Letters*, 527, 115783. https://doi.org/10.1016/j.epsl.2019.115783

Lara, L. E. (2009). The 2008 eruption of the Chaitén Volcano, Chile: A preliminary report. *Andean Geology*, 36(1). https://doi.org/10.4067/S0718-71062009000100009

Lipman, P. W. (1968). Geology of the Summer Coon volcanic center, eastern San Juan Mountains, Colorado. *Colorado School of Mines Quarterly*, 63:211-236.

Lipman, P. W. (1976). Geologic map of the Del Norte area, eastern San Juan Mountains, Colorado. *U.*

S. Geological Survey Miscellaneous Investigations I-952.

Lipman, P. W., Zimmerer, M. J., & Gilmer, A. K. (2024). Precursors to a continental-arc ignimbrite flare-up: Early central volcanoes of the San Juan Mountains, Colorado, USA. *Geosphere*, 20(1), 23–73. https://doi.org/10.1130/GES02691.1

Mertzman, S. (1972). *The geology and petrology of the Summer Coon Volcano, Colorado*. (Doctoral dissertation, Case Western University)

Mitchell, K. L. (2005). Coupled conduit flow and shape in explosive volcanic eruptions. *Journal of Volcanology and Geothermal Research*, 143(1–3), 187–203. https://doi.org/10.1016/j.jvolgeores.2004.09.017

Moats, W. P. (1990). *Geometry and emplacement of silicic dikes at Summer Coon volcano, Rio Grande and Saguache Counties, Colorado*. (Unpublished Master's Thesis, Arizona State University)

Mullet, B. G., & Segall, P. (2021). Stress-Driven Failure of Cylindrical Volcanic Conduits. *Journal of Geophysical Research: Solid Earth*, 126(8). https://doi.org/10.1029/2021JB022278

Pinel, V., & Jaupart, C. (2000). The effect of edifice load on magma ascent beneath a volcano. *Philosophical Transactions of the Royal Society of London. Series A: Mathematical, Physical and Engineering Sciences*, 358(1770), 1515–1532. https://doi.org/10.1098/rsta.2000.0601

Poland, M. P., Fink, J. H., & Tauxe, L. (2004). Patterns of magma flow in segmented silicic dikes at Summer Coon volcano, Colorado: AMS and thin section analysis. *Earth and Planetary Science Letters*, 219(1–2), 155–169. https://doi.org/10.1016/S0012-821X(03)00706-4

Romine, W. L., Whittington, A. G., Nabelek, P. I., & Hofmeister, A. M. (2012). Thermal diffusivity of rhyolitic glasses and melts: Effects of temperature, crystals and dissolved water. *Bulletin of Volcanology*, 74(10), 2273–2287. https://doi.org/10.1007/s00445-012-0661-6

Rust, A. C., Cashman, K. V., & Wallace, P. J. (2004). Magma degassing buffered by vapor flow through brecciated conduit margins. *Geology*, 32(4), 349. https://doi.org/10.1130/G20388.2

Schindelin, J., Arganda-Carreras, I., Frise, E., Kaynig, V., Longair, M., Pietzsch, T., Preibisch, S., Rueden, C., Saalfeld, S., Schmid, B., Tinevez, J.-Y., White, D. J., Hartenstein, V., Eliceiri, K., Tomancak, P., & Cardona, A. (2012). Fiji: An open-source platform for biological-image analysis. *Nature Methods*, 9(7), 676–682. https://doi.org/10.1038/nmeth.2019

Schipper, C. I., Castro, J. M., Tuffen, H., James, M. R., & How, P. (2013). Shallow vent architecture during hybrid explosive–effusive activity at Cordón Caulle (Chile, 2011–12): Evidence from direct observations and pyroclast textures. *Journal of Volcanology and Geothermal Research*, 262, 25–37. https://doi.org/10.1016/j.jvolgeores.2013.06.005

Schneider, A., Rempel, A. W., & Cashman, K. V. (2012). Conduit degassing and thermal controls on

eruption styles at Mount St. Helens. *Earth and Planetary Science Letters*, 357–358, 347–354. https://doi.org/10.1016/j.epsl.2012.09.045

Shields, J. K., Mader, H. M., Caricchi, L., Tuffen, H., Mueller, S., Pistone, M., & Baumgartner, L. (2016). Unravelling textural heterogeneity in obsidian: Shear-induced outgassing in the Rocche Rosse flow. *Journal of Volcanology and Geothermal Research*, 310, 137–158. https://doi.org/10.1016/j.jvolgeores.2015.12.003

Sieh, K., & Bursik, M. (1986). Most recent eruption of the Mono Craters, eastern central California. *Journal of Geophysical Research: Solid Earth*, 91(B12), 12539–12571. https://doi.org/10.1029/JB091iB12p12539

Smith, R. P. (1975). *Structure and Petrology of Spanish Peaks Dikes.* (Doctoral Dissertation, University of Colorado, Boulder)

Stasiuk, M. V., Barclay, J., Carroll, M. R., Jaupart, C., Ratté, J. C., Sparks, R. S. J., & Tait, S. R. (1996). Degassing during magma ascent in the Mule Creek vent (USA). *Bulletin of Volcanology*, 58(2–3), 117–130. https://doi.org/10.1007/s004450050130

Tuffen, H., & Dingwell, D. (2005). Fault textures in volcanic conduits: Evidence for seismic trigger mechanisms during silicic eruptions. *Bulletin of Volcanology*, 67(4), 370–387. https://doi.org/10.1007/s00445-004-0383-5

Tuffen, H., Dingwell, D. B., & Pinkerton, H. (2003). Repeated fracture and healing of silicic magma generate flow banding and earthquakes? *Geology*, 31(12), 1089. https://doi.org/10.1130/G19777.1

Unwin, H. E., Tuffen, H., Wadsworth, F. B., Phillips, E. R., James, M. R., Foster, A., Kolzenburg, S., Castro, J. M., & Porritt, L. A. (2023). The exposed Mule Creek vent deposits record the structure of a volcanic conduit during a hybrid explosive–effusive eruption. *Bulletin of Volcanology*, 85(5), 28. https://doi.org/10.1007/s00445-023-01638-z

Wadsworth, F. B., Llewellin, E. W., Castro, J. M., Tuffen, H., Schipper, C. I., Gardner, J. E., Vasseur, J., Foster, A., Damby, D. E., McIntosh, I. M., Boettcher, S., Unwin, H. E., Heap, M. J., Farquharson, J. I., Dingwell, D. B., Iacovino, K., Paisley, R., Jones, C., & Whattam, J. (2022). A reappraisal of explosive–effusive silicic eruption dynamics: Syn-eruptive assembly of lava from the products of cryptic fragmentation. *Journal of Volcanology and Geothermal Research*, 432, 107672. https://doi.org/10.1016/j.jvolgeores.2022.107672

Wadsworth, F. B., Llewellin, E. W., Vasseur, J., Gardner, J. E., & Tuffen, H. (2020). Explosive-effusive volcanic eruption transitions caused by sintering. *Science Advances*, 6(39), eaba7940. https://doi.org/10.1126/sciadv.aba7940

Walker, R. J., Branney, M. J., & Norry, M. J. (2017). Dike propagation and magma flow in a glassy rhyolite dike: A structural and kinematic analysis. *GSA Bulletin*, 129(5–6), 594–606. https://

doi.org/10.1130/B31378.1

Wicks, C., de la Llera, J. C., Lara, L. E., & Lowenstern, J. (2011). The role of dyking and fault control in the rapid onset of eruption at Chaitén volcano, Chile. *Nature*, 478(7369), 374–377. https://doi.org/10.1038/nature10541

Wolff, J. A. (1986). Welded-tuff dykes, conduit closure, and lava dome growth at the end of explosive eruptions. *Journal of Volcanology and Geothermal Research*, 28(3–4), 379–384. https://doi.org/10.1016/0377-0273(86)90032-6

CHAPTER FIVE

Aksit, G.G., Townsend, M.R., Harp, A.G. (2023, January 30 -February 3). Silicic dike propagation at stratovolcanoes: A petrofabric analysis to determine magma transport directions at Summer Coon volcano, CO, USA. [*Conference Presentation*]. IAVCEI 2023 Scientific Assembly, Rotorua, New Zealand.

Pinel, V., & Jaupart, C. (2000). The effect of edifice load on magma ascent beneath a volcano. *Philosophical Transactions of the Royal Society of London. Series A: Mathematical, Physical and Engineering Sciences*, 358(1770), 1515–1532. https://doi.org/10.1098/rsta.2000.0601

Pinel, V., & Jaupart, C. (2004). Magma storage and horizontal dyke injection beneath a volcanic edifice. *Earth and Planetary Science Letters*, 221(1–4), 245–262. https://doi.org/10.1016/S0012-821X(04)00076-7

Harp, A. G., & Valentine, G. A. (2018). Emplacement controls for the basaltic-andesitic radial dikes of Summer Coon volcano and implications for flank vents at stratovolcanoes. *Bulletin of Volcanology*, 80(2), 16. https://doi.org/10.1007/s00445-018-1194-4